Understanding the Role of Latent Heating in the Heat and Mass Transport of the Global Atmospheric Circulation

by

Robert Fajber

A thesis submitted in conformity with the requirements
for the degree of Doctor of Philosophy
Graduate Department of Physics
University of Toronto

Abstract

Understanding the Role of Latent Heating in the Heat and Mass Transport of the Global Atmospheric Circulation

Robert Fajber

Doctor of Philosophy

Graduate Department of Physics

University of Toronto

2020

Almost one quarter of the insolation from the sun evaporates water vapor at the surface, which adds thermal energy to the atmosphere through latent heating. The main goals of this thesis are to diagnose and quantify the role that this latent heating plays in atmospheric transport and the global general circulation. Using the equivalent potential temperature (θ_e) as a variable to study the circulation implicitly accounts for the effects of latent heating on the dynamics, suggesting that tropospheric transport should follow these surfaces. In chapter 2 this idea is heuristically tested using an idealized moist general circulation model with perturbed midlatitude surface temperatures; the atmosphere responds by transporting warm air along climatological θ_e surfaces.

In chapter 3 we study the mass transport of the general circulation projected onto θ_e surfaces using the Statistical Transformed Eulerian Mean (STEM), which parameterizes this circulation using zonal mean statistics. The functional dependence of the STEM is exploited to understand the response of the circulation on θ_e surfaces to climate perturbations, by calculating the functional derivatives. One key finding is that the sensitivity of the circulation is inversely proportional to the zonal mean standard deviation of θ_e.

The preceding analysis using θ_e is complemented in chapter 4 by a novel heat tagging method developed in this thesis which allows us to attribute the potential temperature (θ) content of the atmosphere to specific diabatic processes. The heat tags includes both locally produced and remotely advected tagged tracer content, providing insight into regions which may be sensitive to remote diabatic processes. This method is applied to an idealized moist general circulation model. The majority of θ in the troposphere is from latent heating, even in the poles here where there is no latent heating. The variability of the heat tags, their use in decomposing heat transport, and the response to a CO_2 doubling experiment are also studied.

Acknowledgements

If it takes a village to raise a child, this thesis would still be in its infancy without the support and advice that I have received over the years.

My supervisor, Paul Kushner, has been instrumental in my development as a scientist during my time at the University of Toronto. His advice and input has been essential in helping me transition from being an undergraduate curious about general circulation modelling into an active researcher in the topic. I am especially grateful for his support during the last leg of my graduate student career.

I am also indebted to my committee members, Dylan Jones and Nicolas Grisouard, who have always taken an active interest in my research far beyond their obligations as members of a thesis committee. Their insights have broadened my research horizons and challenged me to view my ideas from multiple perspectives.

I was quite fortunate to work in an engaging research group, and I thank all of the graduate students and postdocs that I met over the years. In particular, I have to thank Frédéric Laliberté for inducting me into the dark art of moist thermodynamic analysis, and Alexandre Audette, who gave me the opportunity to pass on this knowledge to the next generation. Zoe Fajber, Maura Dewey, and Alexandre Audette all helped with copy editing this document; the remaining typos are mine and mine alon.

Last, but certainly not least, I have to thank my partner, Emi Hunter, who has put up with me longer and more than anyone else mentioned here, and without her support over the years I would never have finished.

Contents

Chapter 1

Introduction

The global atmospheric circulation exists to balance the differential absorption of solar heating between the atmosphere and the poles. Since more energy is absorbed in the tropics than is emitted, and more energy is emitted than absorbed in the tropics, there must exist a transport of energy between the tropics and the poles. By considering the net atmospheric energy balance, it can be anticipated that the heat transport connected with water vapor plays a large role in creating this transport. However, quantifying this role is complicated by the coupling between atmospheric dynamics and latent heating. This thesis discusses two different ways of accounting for this coupling, to find the role of water vapor in the global heat transport, and discusses them in the context of idealized models experiments designed to demonstrate their utility as well as climate change scenarios.

The first technique involves regridding the circulation into a phase space with a variable that is conserved under condensation (the equivalent potential temperature). While this has been done before, this thesis uses the technique in the context of novel short term perturbations in Chapter 2, and a mathematical framework that demonstrates how the response of the circulation can be related to the unperturbed circulation is developed in Chapter 3.

The second technique involves using passive tracers, called "heat tags", which record the contributions of various diabatic processes the potential temperature in the atmosphere. The heat tags related to latent heating encapsulate information connecting the dynamics of water vapor with the atmospheric heat content and transport, and link information from remote regions together. While previous analysis techniques have been used to study the total heat transport, the heat tags allow us to isolate the heat transport directly attributable to latent heating.

This Chapter introduces both the necessary background for these studies as well as the more specific

scientific questions that the thesis addresses. Section 1.1 briefly discusses the atmospheric energy balance and what constraints it provides on atmospheric heat transport. Section 1.2 begins by introducing the potential temperature and equivalent potential temperature, then describes the thermodynamic phase analysis used in Chapters 2 and 3, and concludes by connecting this thermodynamic phase space analysis to heat transport. Section 1.3 briefly summarizes the main results of the previous Sections, and then discusses the idealized moist model that is used in Chapters 2 and 4, before placing the remaining Chapters in their scientific context.

Coming out of this thesis, the reader will have a better understanding of the role that latent heating and moisture play in the transport of mass and heat in the global circulation. This understanding aids in our interpretation of how tropospheric transport moves heat from the tropics to the poles in the modern circulation and how this heat transport will respond to changes in temperature and moisture as a result of climate change.

1.1 Atmospheric Energy Balance

Most of the energy that is added to the atmosphere does not happen through direct solar absorption, but through interactions with the surface, which has important consequences for the global heat transport. Of the 341 W/m^2 of incoming solar radiation, only 78 W/m^2 is absorbed by the atmosphere, while 102 W/m^2 is reflected back into space, and 161 W/m^2 is absorbed by the surface (Trenberth et al., 2009). Most of the energy absorbed by the surface is transferred to the atmosphere; 40W/m^2 is transferred directly to space through the atmospheric window, 1 W/m^2 is absorbed by the surface, while a net 120 W/m^2 is transferred to the atmosphere. Of the energy transferred to the atmosphere 23 W/m^2 is transferred through longwave radiation, 20 W/m^2 is transferred through turbulent sensible heat flux, and 85 W/m^2 is transferred back to the atmosphere through evaporation of water vapor at the surface (Trenberth et al., 2009). The evaporation of water vapor into the atmosphere represents the majority of the energy transfer from the surface to the atmosphere, and the largest source of energy in the atmosphere overall. Balancing these transfers of energy to the atmosphere is a net transfer of the atmosphere to space of 239 W/m^2.

The different mechanisms for adding heat to the atmosphere also relate to the dynamics of the atmosphere differently. On the thousands of kilometer length scales relevant to the dynamics of the global circulation, radiative processes are approximately vertical (Ling and Zhang, 2013), so that the full three dimensional radiative transfer equations can be replaced by one dimensional radiative transfer equations (an approximation made in many general circulation models, including the ones used in this

thesis). Under this approximation the radiative transfer can be determined by the temperature profile and the radiative properties within a single atmospheric column, and is coupled to the dynamics by modifications to these properties. The turbulent transfer of sensible heat to the atmosphere occurs only in the lowermost layer of the troposphere, and so is coupled to the dynamics by the windspeed and the temperature difference locally at the surface. By contrast while the evaporative flux is controlled by the wind speed and moisture difference between the atmosphere and the surface, the moisture added to the atmosphere does not have a significant effect on the atmosphere until condensation or sublimation occurs and latent heat release decreases the density. This means that latent heating can couple to atmospheric dynamics in more complicated ways, because it depends both on the dynamics at the surface controlling evaporation as well as the large scale circulation which concentrates the moisture and saturates the atmosphere. Additionally, because so much of the energy added to the atmosphere is through evaporation of water vapor, most of the convection on Earth couples the dry dynamics with moisture and latent heating (see the introduction of Emanuel, 1994). Considering only the energetics of dry air will lead to a very different view on what controls large-scale stability (or stratification) than if the dry and moist air are considered together.

The global heat transport involves both sensible and latent components, whose proportions are determined by a combination of the mean surface temperature and the surface temperature gradient (Caballero, 2005). Whether the total heat transport involving water vapor is studied or whether only the dry heat transport is studied without water vapor will significantly change our perspective on atmospheric transport of mass and heat. For instance, while evaporation more or less monotonically decreases from the tropics to the poles, latent heating is greatest in the deep tropics and the midlatitude stormtracks (Trenberth and Stepaniak, 2003a,b; Ling and Zhang, 2013). The dry heat transport and the total heat transport thus look different because of the conversion of latent to thermal energy by condensation. Choosing between an analysis based on the energetics of dry air or on the energetics of moist air will thus lead to different conclusions about the role of water vapor in the atmosphere.

Even the dry moist and total heat transport is known, there remain many unanswered questions regarding the linkage of heat transport to the dynamics of the atmosphere. For instance, does the atmo sphere transport heat through laminar or turbulent flow? How does the heat added through evaporation change the dynamics and heat transport in the atmosphere? How do the thermodynamic changes from climate change impact the heat transport of the atmosphere? Investigating the relationship between atmospheric heat transport and atmospheric dynamics, and the role that moisture plays in this, is the subject of this thesis.

1.2 Thermodynamic Analysis of Atmospheric Flows

1.2.1 Moist Thermodynamics

Throughout this thesis I assume that an air parcel consists of a homogeneous mixture of a well-mixed ideal gas component called "dry air" and a moist component consisting of vapor, liquid, and solid water. The entropy of the dry air can be written as a function of the temperature and pressure of the dry air

$$S_d = C_p \ln\left(\frac{T}{T}^0\right) + R_d \ln\left(\frac{p_d}{p^0}\right). \tag{1.1}$$

It is related to a potential temperature by

$$\begin{aligned} \theta = &\quad T^0 \exp(\tfrac{S_d - S_d^0}{C_d}) \\ = &\quad T\left(\tfrac{p_d}{p_0}\right)^{\frac{R_d}{C_p}} \end{aligned} \tag{1.2}$$

where C_p is the heat capacity at constant pressure, R_d is the ideal gas constant, p_d is the pressure, all of the dry air, and T^0 and p^0 are the reference temperature and reference pressure. Traditionally the reference temperature is chosen to be the triple point of water and p_0 is chosen to be the average surface pressure, in order to reflect reasonable atmospheric conditions. Implicit in this definition is the choice $S_d^0 = 0 J\,K^{-1}$, another choice would lead to a different factor appearing in the definition of θ. The potential temperature has a physical interpretation: it is the temperature that a parcel would have if it was adiabatically raised or lowered through the atmosphere to the reference pressure p^0. For this process, the dry static energy DSE $= C_p T + \Phi$ (where Φ is the geopotential height) must also be conserved following an air parcel. Since at the reference pressure, DSE $= C_p T = C_p \theta$, then DSE $= C_p \theta$ everywhere for an adiabatic process. For a diabatic atmosphere this relationship is no longer exact, but is still a good approximation. Our goal is to find an analogous expression for the total system of air and water.

How many thermodynamic variables are needed to describe the mixture of dry air and moist components? To constrain a system where the substances are in thermal equilibrium, the temperature and density of all four substances would have to be known, for a total of 5 variables. Then the total, or moist, entropy of the air parcel would be

$$S_m = f(T, p_d, \rho_v, \rho_l, \rho_s) \tag{1.3}$$

where ρ_v, ρ_i and ρ_s are the densities of the water vapor, liquid, and ice phases (e.g. Hauf and Höller, 1987).

Since this thesis is concerned with the impacts of latent heating on the dynamics of the atmosphere, it is useful to make some further simplifications.

1. The solid phase of water is not present in the atmosphere.
2. The water vapor is in thermodynamic equilibrium with the water condensate, so that the Gibbs functions are equal. This precludes non equilibrium phases (such as super cooled liquid) from being considered.
3. The entropy of mixing can be ignored (e.g. see Hauf and Höller, 1987), which is small compared with other sources of entropy (Pauluis et al., 2010).
4. The reference state of the moist component is assumed to have $S_{v0} = \frac{L_{v0}}{T_0}$ and $S_{l0} = 0 J\,K^{-1}$, where S_{v0} and S_{l0} are the reference entropies of the vapor component and the liquid component separately.
5. No water is removed from the air parcel.

Under these assumptions the moist entropy per dry air mass can be written as

$$S_m = (C_p + r_t C_l) ln\left(\frac{T}{T_0}\right) - R_d ln\left(\frac{p_d}{p_{d0}}\right) - r_v R_v ln\left(\frac{p_v}{p_v^*}\right) + r_v \frac{L_v}{T}, \tag{1.4}$$

where p_v^* is the saturation vapor pressure and $r_t = \frac{\rho_v + \rho_l}{\rho_d}$. For small amounts of water θ_e approaches θ.

If assumption 1 were not made there would be an additional term involving the latent heating of fusion in equation (1.4). If a different value for S_{v0} was chosen there would be an extra term involving the reference latent heat of vaporization. These extra terms will occur because at the reference state we must have $S_{v0} - S_{l0} = \frac{L_{v0}}{T0}$ for the two water phases to be in equilibrium; since if both S_{v0} and S_{l0} are simultaneously set to 0 we will require an extra term to adjust L_{v0}. Including the effects of freezing gives values of θ_e that are one to two degrees warmer for saturated, surface air at 300 K (Bryan and Fritsch, 2004), and lower for colder or less saturated air. We will neglect the effects of freezing in order to match further simplifications made later.

The choice of $S_{l0} = 0$ is what actually defines this version of the moist entropy; by choosing the moist component to be referenced to liquid water we minimized the effects of moving liquid water into or out of an air parcel. With the choice of $S_{v0} = 0$ we could have referenced the moist component of the system to water vapor, which would minimize the effects of moving water vapor into or out of an air parcel (Emanuel, 1994, Section 4.5). Since the main focus of this thesis is on precipitating air parcels, the choice of $S_{l0} = 0$ is advantageous and we will not consider any other choice.

The saturation vapor pressure $p_v^* = f(T, p_d)$, so that $p_v = f(T, p_d, r_t)$. Therefore $S_m = f(T, p_d, r_T)$, so these assumptions have reduced the number of variables needed to define the thermodynamic state of an airmass from five to three. This is essentially a restatement of Gibb's phase rule for the system of dry air and water, since I have introduced chemical equilibrium between the different water phases.

Defining the equivalent moist potential temperature analagously to the dry potential temperature case,

$$\begin{aligned} \theta_e &= T^0 exp\left[\frac{s_m}{C_d + r_t C_l}\right] \\ &= T\left(\frac{P_d^0}{P_d}\right)^{\frac{R_d}{C_d + r_t C_l}} \mathcal{H}^{\left(\frac{-r_v R_v}{C_d + r_t C_l}\right)} exp\left[\frac{r_v L_v}{(C_d + r_t C_l)T}\right] \end{aligned} \tag{1.5}$$

where θ_e is known as the equivalent potential temperature and $\mathcal{H} = \frac{p_v}{p_v^*}$ is the relative humidity.

The moist entropy is conserved for a reversible adiabatic process. In particular S_m will be conserved during phases transformations as long as they happen at thermodynamic equilibrium (so that $ln\mathcal{H} = 0$). One example for which this will be violated is for evaporation into unsaturated air. This happens primarily under two circumstances, either through turbulent mixing in the planetary boundary layer; which adds water vapor to unsaturated parcels, or through the evaporation of falling precipitation. The condition of reversibility is also not met for precipitating air parcels, since the removal of liquid water means that they are unable to return to their initial state, even if the atmospheric processes that bought the parcel to that point were reversed. Our choice of reference entropies minimizes this entropy loss to the removal of liquid water, but it does not eliminate it entirely.

To come up with a quantity which is conserved for precipitating air parcels I make one further simplification by assuming that all of the precipitation is immediately removed from the atmosphere. This assumption is referred to as the pseudo-adiabatic assumption, and it replaces assumption 5 in the previous list. The entropy of this process, referred to as the pseudo-adiabatic moist entropy, can be written as

$$S_p = f(T, P, r_v) \tag{1.6}$$

so that the entropy can determined using only water vapor. This restriction forces us to choose a single condensed phase of water vapor to use, since it cannot be known apriori whether the water vapor was removed above or below the freezing point. The use of only using liquid water in S_m allows the formulation of S_m and S_p to be closer.

Unfortunately this entropy does not have an analytic solution, because the entropy is no longer a perfect differential for an open system (Emanuel, 1994, Section 4.7). The corresponding equivalent

potential temperature can be approximated by

$$\theta_e \approx \theta \left(\frac{p_v}{p_v^*} \right)^{-r_v \frac{R_v}{C_p}} \exp\left(\frac{L_v r_v}{C_p T} \right) \tag{1.7}$$

or by several empirical formulas that vary from the exact solution by only a few tenths of a degree (Bolton, 1980).

Despite the lack of an analytic solution, the pseudo-adiabatic equivalent potential temperature has several advantages over the reversible θ_e. First, it can be calculated using only the specific humidity, without requiring any information about cloud water or cloud ice. In fact, by assuming that all of water is removed as liquid, the use of a pseudoadiabatic variable precludes introducing freezing. Secondly, it corresponds to a physical process: it is the temperature of a moist air parcel, raised up to a great height in the atmosphere so that all of the water vapor is condensed (and immediately precipitated), and then adiabatically returned to the reference pressure p_0 (Emanuel, 1994, Section 4.5). The θ_e of a reversible adiabatic process, i.e. with entropy defined by equation (1.4), cannot be defined in the same way; if an air parcel were raised to a high altitude so that the water was condensed (and held inside the parcel so that total water is conserved), then returned to the surface its temperature would be the same as the initial temperature since all of the water would evaporate during the descent. The irreversibility of pseudo-adiabatic processes from precipitation is what enables the starting and ending temperatures to be different.

Reversible adiabatic and the pseudo-adiabatic processes represent two distinctive possibilities in which either ascending air parcels retain all liquid water or lose all liquid immediately. The real atmosphere lies between these two possibilities, since both clouds and precipitation exist in the atmosphere simultaneously. Throughout the rest of this thesis I will use the psuedo-adbatic θ_e, because it matches the assumptions made by the idealized general circulation numerical model, used in Chapters 2 and 4, and it can be computed without having to know the liquid water content (which is not available for all of the datasets considered in Chapter 3).

Similar to the relationship between DSE and $C_p\theta$, the moist static energy, MSE $= C_pT + \Phi + L_vq$ is well approximated by $C_p\theta_e$ for a moist adiabatic process. The difference MSE $- C_p\theta_e$ is the work converted into kinetic energy during moist adiabatic ascent; if MSE is conserved all of the work is converted and if $C_p\theta_e$ is conserved none of the work is converted (Betts, 1974). θ_e and MSE have very similar distributions in the atmosphere, and very similar integrated transports (Emanuel, 1994). This is what justifies referring to the transport of $C_p\theta_e$ as the atmospheric heat transport.

I briefly illustrate the difference between the dry potential temperature θ and the moist potential

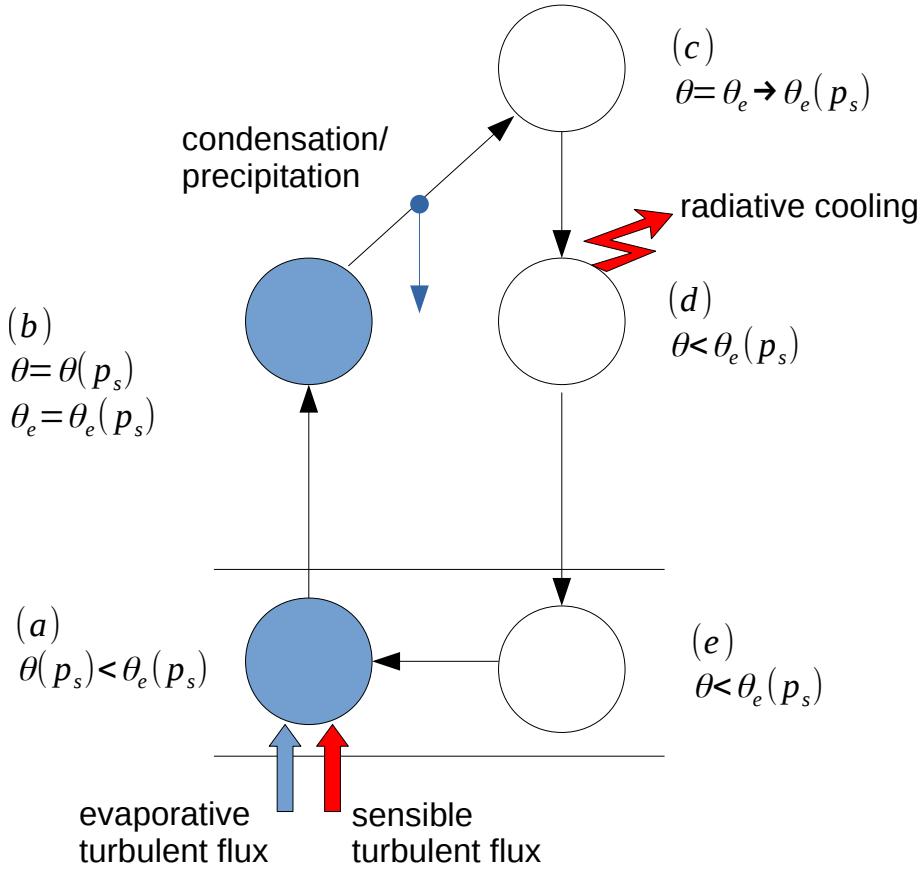

Figure 1.1: Idealized cycle of an air parcel from and to the PBL, showing the diabatic processes and the relationship between θ and θ_e as it occurs. $\theta|_s$ and $\theta_e|_s$ are the θ and θ_e values in equilibrium with the surface.

temperature θ_e by considering an idealized thermodynamic cycle. Ignoring irreversible processes (e.g. the entropy lost to falling rain water), the budgets for the dry and moist potential temperatures are

$$\begin{aligned} \dot{\theta} &\approx \frac{\Pi}{C_p}\left(L_v\dot{q}_{cond} + Q_{sens} + Q_{radi}\right) \\ \dot{\theta}_e &\approx \frac{\Pi}{C_p}\left(L_v\dot{q}_{evap} + Q_{sens} + Q_{radi}\right) \end{aligned} \tag{1.8}$$

where $\dot{q}_{cond}$ is the water vapor tendency from condensation, $\dot{q}_{evap}$ is the water vapor from evaporation, Q_{sens} is the heating from turbulent sensible heat fluxes, and Q_{radi} is the radiative heating. Note that the evaporation term is only valid for the pseudoadiabatic form of θ_e. For the reversible form of θ_e the evaporation would only appear as a tendency if it happened in unsaturated air. The main source of evaporation in the atmosphere is in turbulent surface fluxes near the surface. The approximations in equation (1.8) are due to ignoring the changes in density and heat capacity due to the presence of water vapor. These variables are both conserved under unsaturated adiabatic ascent, but account for the impacts of water vapor differently.

Consider an air parcel which undergoes an idealized cycle of an air parcel moving through the atmosphere (figure 1.1): initially the air parcel is in the boundary layer where it experiences large turbulent fluxes(a), then it ascends to the lifted condensation level where it saturates(b), then continues ascending to a high altitude, during which the water vapor condenses and precipitates out(c), followed by radiative cooling in the free troposphere(d) followed by a return to the boundary layer(e). In general the turbulent fluxes of moisture and sensible heat are large in the boundary layer and negligible outside. While the parcel is in the boundary layer the turbulent fluxes will force the parcel to match the boundary layer properties(a), having $\theta = \theta(p_s)$ and $\theta_e = \theta_e(p_s) > \theta(p_s)$, because the boundary layer is moist. Once an air parcel leaves the boundary layer it experiences adiabatic ascent, with its θ and θ_e values unchanged, until it reaches its lifted condensation level (b) where the air saturates. After this point condensation will act to increase θ but not θ_e as the parcel ascends. Eventually, once the parcel has ascended to a great height and all of the moisture has been removed(c) then $\theta \to \theta_e = \theta_e(p_s)$. At this point, θ_e is related to the buoyancy of the air parcel because all of the latent energy has been converted to thermal energy. Stability calculations which compare θ_e at the surface to a layer above are valid if that layer is high enough in the atmosphere that saturation occurs, otherwise they may falsely include the latent energy on the buoyancy of the air parcel (equivalent to ignoring the convective inhibition energy, see Chapter 6 of Emanuel, 1994). As the air parcel moves through the free troposphere it will be subject to longwave cooling(d), which operates on longer time scales than the turbulent boundary layer fluxes or the initial ascent phase (which is why it was ignored in these stages). Eventually the air parcel will be

recycled into the boundary layer(e), and the cycle can begin again.

This idealized cycle highlights the different information that can be gained by studying θ or θ_e. To study the connection between the near surface atmosphere and free troposphere (as I do in Chapter 2), θ_e is a good choice of variable; since it is conserved during the initial fast ascent. To study the warm air created by latent heating in the troposphere (as I do in Chapter 4), then θ is a good variable to use.

I close this Subsection with a comment on the potential vorticity of a moist atmosphere. For a dry atmosphere the potential vorticity is normally defined as

$$PV = \rho^{-1} \left(2\Omega + \nabla \underline{u}\right) \cdot \nabla\theta \tag{1.9}$$

where Ω is the planetary rotation rate, and $\underline{u}$ is the velocity vector. Given a distribution of θ the PV can be inverted to find the velocities (see Holton, 2004, Sections 4.3 and 6.3). By replacing θ by θ_e in this formula, can a potential vorticity be found that is also invertible given a distribution of θ_e? The answer is no; crucially, which regions of the atmosphere that are saturated or unsaturated will not be known, and so require additional knowledge of the water vapor field (Schubert et al., 2001). This is a restatement of the earlier observation that θ_e was a function of T, p_d, and r_t. There are similar problems with defining a moist quasi-geostrophic theory; some assumption about the dynamics of water vapor has to be made in order to define an invertibility principle (Cohen and Boos, 2016). Recently Yamada and Pauluis (2016) found a formulation for a moist Elissian-Palm flux, but only in θ_e space (defined in the next Section), so it is not invertible into pressure space, or connected to a particular potential vorticity the way it would be in a dry atmosphere. This thesis, however, focuses primarily on the mass transport in the atmosphere, and so these considerations about potential vorticity are not pursued further.

1.2.2 Distribution of θ and θ_e in the Atmosphere

The distributions of some zonal mean statistics, related to mean state and variability of θ and θ_e in the troposphere, are shown in figure 1.2. The data here (and in the other figures) is annual mean data averaged over the years 1980-2019 from the ERA5 reanalysis dataset (Copernicus Climate Change Service Climate Data Store, 2017). The 300 K $\overline{\theta}$ (where $\bar{\cdot}$ is a zonal mean) surfaces almost extend from the tropical surface to the Arctic midtroposphere. Colder θ iso-surfaces connect points in the subtropics and extratropics to points in the arctic midtroposphere, and warmer θ iso-surfaces do not make contact with the surface. This is in contrast with the $\overline{\theta_e}$ adiabats, which all make contact with the surface. In the tropics $\overline{\theta_e}$ values are highest near the surface and upper troposphere with a minimum in the midtroposphere.

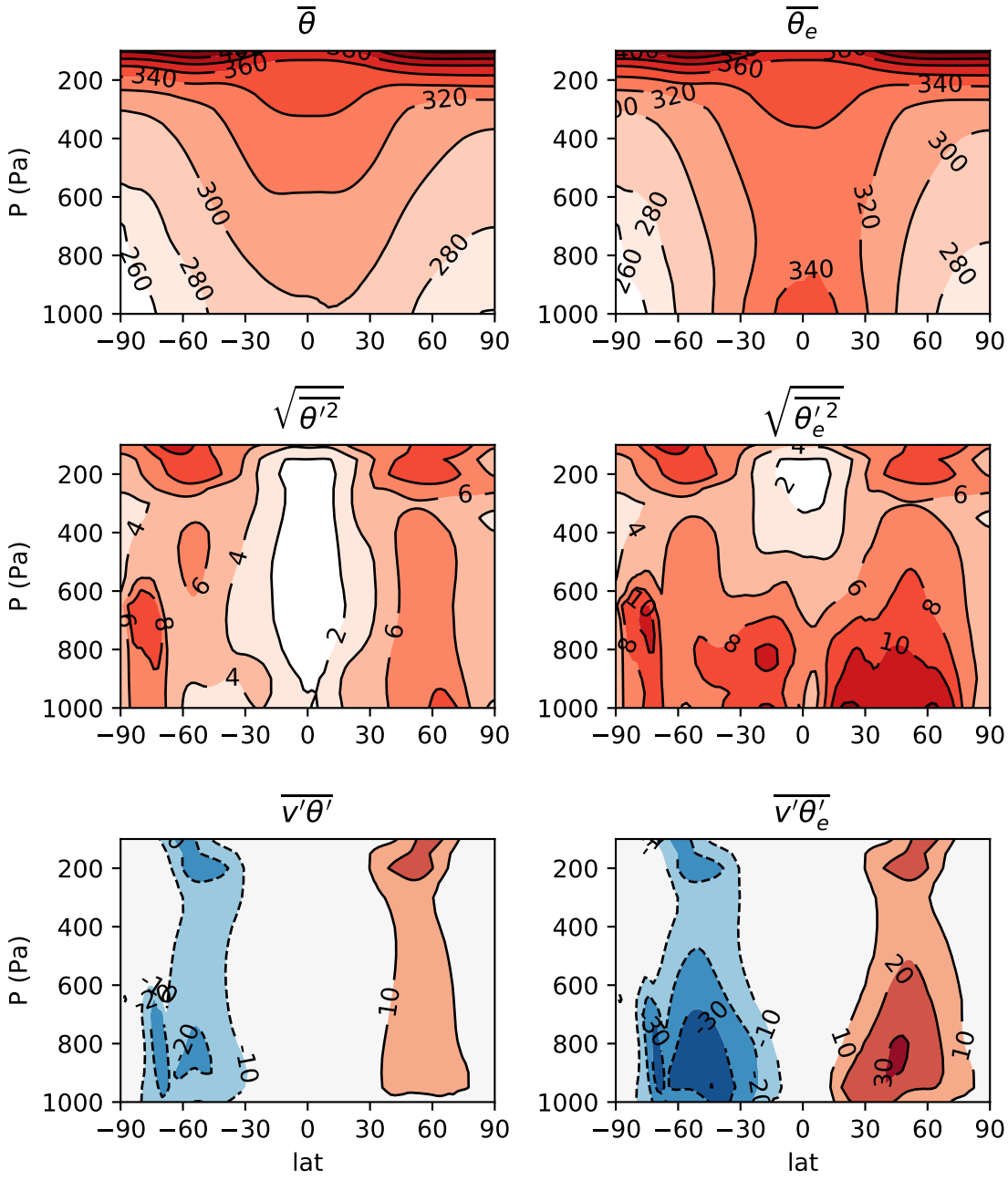

Figure 1.2: Zonal mean climatologies of the mean and variability of θ (left) and θ_e (right) for the ERA5 reanalysis. Top row: zonal mean distribution of θ and θ_e, middle row: zonal standard deviation of θ and θ_e, bottom row, eddy covariances of θ and θ_e with v.

The vertical stratification of θ and θ_e are used as indicators of vertical stability (Iribarne and Godson, 1981, Chapter 9). In the case of θ, this is an absolute instability; since $\rho = f(\theta, p)$, so if $-\frac{1}{g}\partial_p\theta < 0$ then the profile will be unstable to infinitesimal perturbations. From figure 1.2 it can be seen that $-\frac{1}{g}\partial_p\overline{\theta} > 0$ everywhere in the atmosphere, or, equivalently, on average the atmosphere is stable with respect to dry convection. The increases of $\overline{\theta}$ in the tropics is related to the latent heating as air parcels rise along moist adiabats. Convection in modern day climates is thus inherently a moist process, and $\overline{\theta}$ should not be used as an indicator of convective stability, except maybe at the poles.

The vertical stability calculated using $\overline{\theta_e}$ includes the effects of moisture, but it is only a conditional instability, since θ_e and ρ cannot be directly related (the relationship will depend on whether the air is saturated or not, and this cannot be determined solely from θ_e). A region of $-\frac{1}{g}\partial_p\overline{\theta_e} < 0$ will only be unstable if the air is mechanically lifted to its level of free convection (see Emanuel, 1994, Section 6.7). Synoptic scale eddies contain regions of updrafts and downdrafts; in the midlatitudes these updraft regions provide sufficient mechanical forcing to lift moist air from the boundary layer to its lifted condensation level, and so $\partial_p\overline{\theta_e}$ can be used in most circumstances as an indicator of stability (Iribarne and Godson, 1981, Chapter 9).

When the temperature decreases p_v^* becomes small, and so the maximum moisture content inside of a parcel also becomes very small. This is the case in the upper troposphere and stratosphere. In these regions, $\theta_e \approx \theta$. This is why above approximately 300 hPa surfaces of $\overline{\theta}$ and $\overline{\theta_e}$ almost coincide.

The standard deviations of θ and θ_e, $\sqrt{\overline{\theta'^2}}$ and $\sqrt{\overline{\theta_e'^2}}$ respectively, are shown in the middle row of figure 1.2. The standard deviation of θ is only significant in the midlatitudes, and has similar values near the surface and the upper troposphere. In contrast, $\sqrt{\overline{\theta_e'^2}}$ has larger values near the surface, and has large values extending into the subtropics and tropics. The difference between the two reflects the variability of water vapor in the atmosphere, and not the mean moisture content. This is why the largest difference occurs in the midlatitude near-surface and not in the tropical near-surface, where $\overline{\theta_e} - \overline{\theta}$ is maximized.

The covariance of θ and θ_e with meridional wind v, $\overline{v'\theta'}$ and $\overline{v'\theta_e'}$ respectively, are shown in the bottom row of figure 1.2. These covariances are also referred to as the eddy transports, since they quantify the transport of θ and θ_e associated with deviations from the zonal mean. This will be discussed more in subsequent Sections. The eddy covariance of θ_e with v is largest in the midlatitudes, with the largest values in the upper troposphere. The eddy covariance $\overline{v'\theta_e'}$ is also large in the midlatitudes, but it is significantly larger at the surface than it is in the upper troposphere. This is again related to the variability of moisture, which is much stronger near the surface. In the upper troposphere there is very limited water vapor, so $\theta_e \approx \theta$, both $\overline{\theta} \approx \overline{\theta_e}$ and the variances and covariances are also very similar.

In the next two Subsections I will show how the distributions of θ and θ_e described here can be used to transform the circulation from pressure space to thermodynamic space.

1.2.3 Streamfunctions in Moist Thermodynamic Variables

The zonal mean streamfunction can be calculated in pressure space as

$$\psi(\phi, p) = L_x \int\int \overline{v} \frac{dp}{-g} \frac{d\lambda}{2\pi}, \tag{1.10}$$

where $L_x = 2\pi a \cos\phi$. The climatological mass flux averaged in pressure space, $M_\phi(\phi, p) = L_x \overline{v}$ and the climatological streamfunction averaged in pressure space $\psi(\phi, p)$, are shown in the top row of figure 1.3. In the tropics the poleward mass flux is coincident with relatively high values of $\overline{\theta}$ and the equatorwards branch is coincident with relatively low values of $\overline{\theta}$ (figure 1.2), resulting in a net transport of θ polewards. However, in the midlatitudes the Ferrel cell rotates the other way, which leads to a net transport of θ equatorwards. This is referred to as a thermally indirect circulation, because the cell cannot be driven solely by diabatic heating, or it would be in violation of the second law of thermodynamics. The streamfunction in pressure space can be driven by mechanical forcing from the surface, and eddy fluxes of momentum and heat, in addition to the diabatic forcing (Holton, 2004, Chapter 10).

The distribution of diabatic heating in the atmosphere is such that the net transport of heat should be polewards everywhere (Trenberth and Stepaniak, 2003a,b; Ling and Zhang, 2013; Zhang et al., 2017). However, the gradient of energy inputs into the atmosphere does not reverse anywhere, implying that there should be a global, thermally direct circulation extending from the equator to the pole. From figure 1.3 it can be inferred that this circulation is not captured by the mean circulation calculated in pressure space. One of the goals of using streamfunctions in thermodynamic space is to find a mean thermally direct circulation that extends over the entire atmosphere.

Below I briefly review the equations for massfluxes on a θ_e surface (analogous equations hold for massfluxes on a θ surface). The meridional mass flux zonally averaged on a θ_e surface is defined by

$$M_\phi(\phi, \theta_e) = \int\int v(\lambda, \phi, p)\, \delta(\theta_e - \theta_e^o(\lambda, \phi, p)) \frac{dp}{-g} \frac{d\lambda}{2\pi} \tag{1.11}$$

where θ_e^o is the observed distribution of θ_e. The delta function projects a point in pressure space into a point into a new space where θ_e is the vertical coordinate. In this new space a vertical mass flux, M_{θ_e}, can be calculated analogously by replacing v with $\dot{\theta_e}$ in (1.11). In steady state these mass fluxes satisfy a mass-conservation equation (Yamada and Pauluis, 2016),

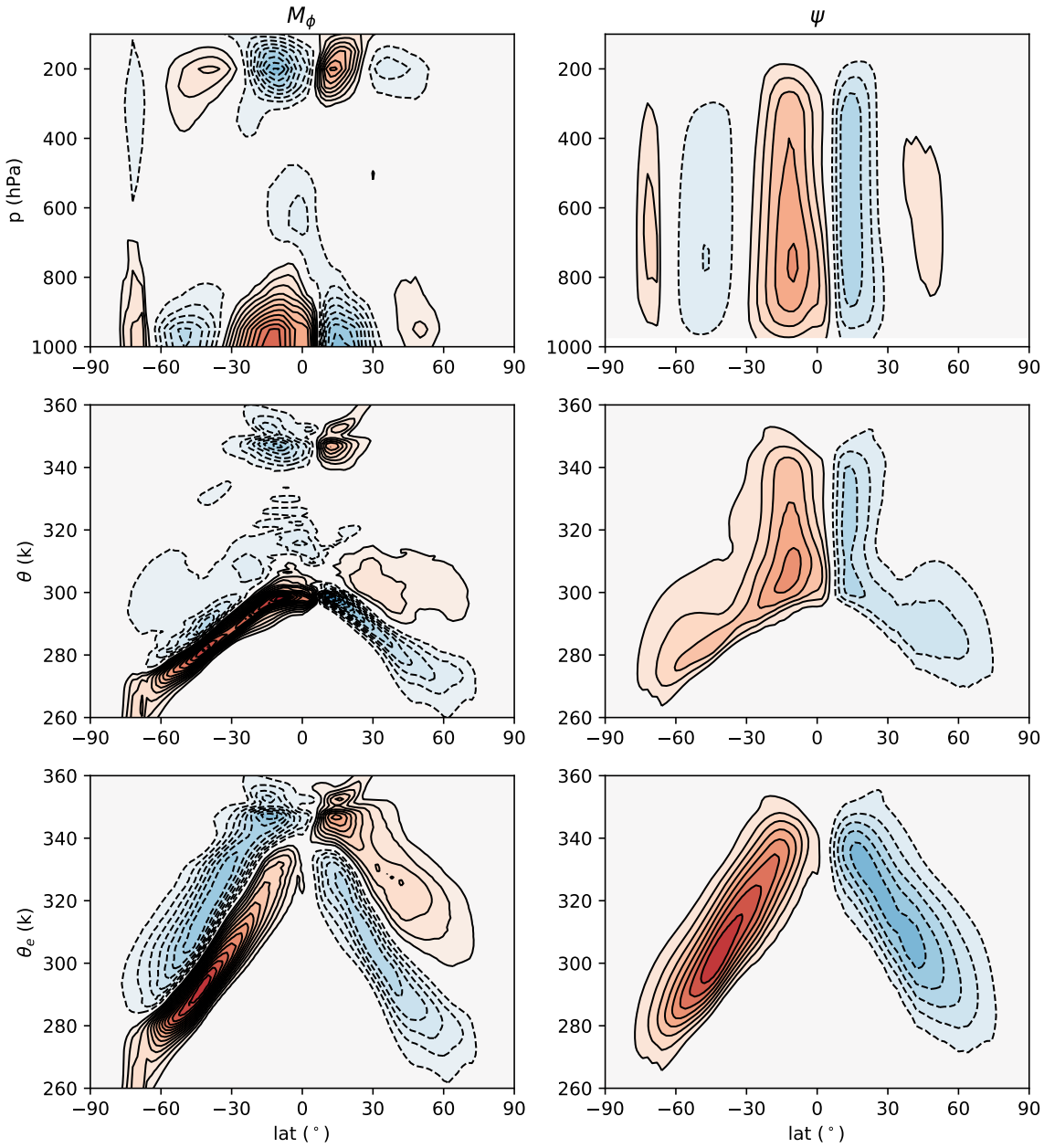

Figure 1.3: Zonal and annual mean climatological meridional mass fluxes (left) and streamfunctions (right) in pressure space (top row), θ space (middle row), and θ_e space (bottom row) for the ERA5 reanalysis. The contour interval is 10^9 ms^{-1} for the mass flux in pressure space, 10^9 kgs^{-1}K^{-1} for the mass fluxes in θ and θ_e space, and 2×10^{10}kgs^{-1} for the streamfunctions.

$$0 = \frac{1}{a\cos\phi}\frac{\partial M_\phi \cos\phi}{\partial\phi}(\phi,\theta_e) + \frac{\partial M_{\theta_e}}{\partial\theta_e}(\phi,\theta_e) \tag{1.12}$$

and

$$M_{\theta_e}(\phi,\theta_e) = \int\int \dot{\theta}_e(\lambda,\phi,p)\,\delta\left(\theta_e - \theta_e^o(\lambda,\phi,p)\right)\frac{dp}{-g}\frac{d\lambda}{2\pi} \tag{1.13}$$

is the diabatic tendency remapped onto θ_e space. In this case the flow is non-divergent and a streamfunction can be calculated as

$$\psi(\phi,\theta_e) = L_x\int_0^{\theta_e} -M_\phi(\phi,\theta_e')d\theta_e' \tag{1.14}$$

where the isolines of the streamfunction will be tangent to vectors of (M_ϕ, M_{θ_e}). Equivalently, positive vertical differences of the streamlines, $\psi(\phi_1,\theta_e) - \psi(\phi_0,\theta_e)$, indicate an equatorward isentropic mass flux ($M_\phi < 0$), and positive horizontal differences of the streamlines, $\psi(\phi,\theta_{e1})$-$\psi(\phi,\theta_{e0})$, indicate a positive diabatic tendency ($M_{\theta_e} > 0$). Equation (1.11) can be substituted into equation (1.14), and by switching the order of integration the streamfunction can be expressed as

$$\psi(\phi,\theta_e) = L_x\int\int vI\left(\theta_e - \theta^o{}_e\right)\frac{d\lambda}{2\pi}\frac{dp}{-g}, \tag{1.15}$$

where $I(x) = 1$ if $x > 0$ and 0 otherwise. This is the expression used in, for example, Pauluis et al. (2008, 2010); Döös and Nilsson (2011). Calculating ψ with M_ϕ is useful for deriving the statistical transformed Eulerian mean (STEM) parametrization considered in the next Section.

For the steady state circulation in θ_e space to conserve mass, the streamfunction must be equal at the upper and lower boundary. This is because the streamfunction difference between an upper bound θ_e^U and a lower bound θ_e^L is $\Delta\psi = \int_{\theta_e^L}^{\theta_e^U} M_\phi d\theta_e$. If θ_e^U and θ_e^L are chosen to encompass the entire atmosphere, then if $\Delta\psi \neq 0$ there must a net mass flux in the atmosphere either towards the equator or towards the pole. In steady state this cannot be allowed, so ψ must be equal on θ_e^U and θ_e^L. For the explicit definition of the streamfunction traditionally $\theta_e^L = 0$ and $\theta_e^U = \infty$, and the streamfunction at these boundaries is chosen to be 0 to facilitate the interpretation of $\psi(\phi,\theta_e)$ as the mass flux on adiabats below θ_e.

Frequently, the circulation in thermodynamic space is referred to as the mass transport needed to balance Earth's radiative imbalance (e.g. Pauluis et al., 2010). To elucidate this phrase I consider a simplified distribution of heating and cooling in the atmosphere comprised of δ-functions:

$$M_{\theta_e}(\phi,\theta) = S\left[\frac{\delta(\phi-\phi_1)}{a\cos\phi_1} - \frac{\delta(\phi-\phi_2)}{a\cos\phi_2}\right]\left[I(\theta_e-\theta_{e1}) - I(\theta_e-\theta_{e2})\right] \tag{1.16}$$

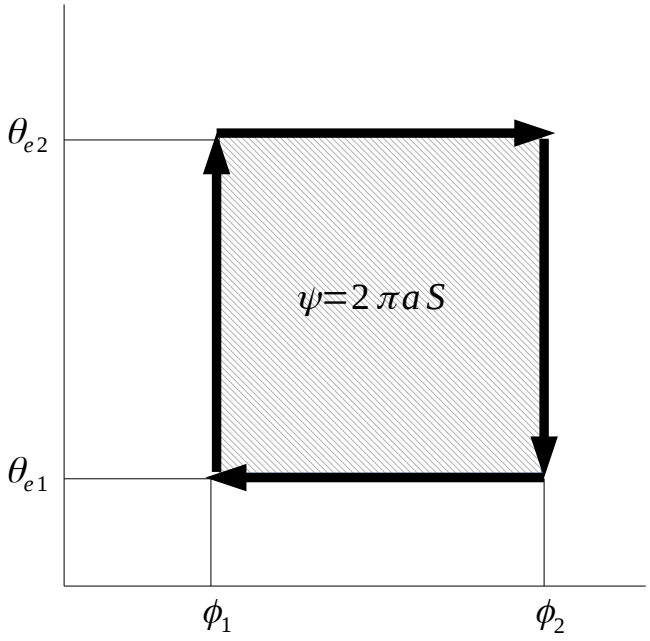

Figure 1.4: Schematic of the idealized circulation created by a delta function of heating at ϕ_1 and a delta function of cooling at ϕ_2.

so that the atmosphere is being heated at a rate $\frac{S}{a\cos\phi_1}$ at latitude ϕ_1 between a lower θ_e, θ_{e1}; and a higher θ_e, θ_{e2} and is also cooled at a rate of $\frac{S}{a\cos\phi_2}$ at latitude ϕ_2 between θ_{e1} and θ_{e2}. For this example, using equation (1.12) gives the meridional mass fluxes

$$M_\phi\left(\phi_1 \le \phi \le \phi_2, \theta_e\right) = \left(\cos\phi\right)^{-1} S\left[\delta\left(\theta_e - \theta_{e2}\right) - \delta\left(\theta_e - \theta_{e1}\right)\right], \tag{1.17}$$

and using equation (1.14) gives

$$\psi\left(\phi, \theta_e\right) = \begin{cases} 2\pi a S & \text{for } \phi_1 \le \phi \le \phi_2, \theta_{e1} \le \theta_e \le \theta_{e2} \\ 0 & \text{elsewhere} \end{cases}. \tag{1.18}$$

This circulation is schematically shown in figure 1.4. The circulation is a square cell bounded by four streamlines: a vertical transport at ϕ_1, a polewards transport at θ_{e2}, another vertical transport at ϕ_2, and an equatorwads transport at θ_{e1}. The streamfunction is a constant value in the region bounded by these four surfaces, and is proportional to the strength of the diabatic forcing. By construction, the mass fluxes transport the amount of heat needed to balance the difference between the heating and cooling, and so they are "in balance" with the diabatic forcing. Additionally, the distribution of the diabatic heating and cooling determines the difference of θ_e between the polewards and equatorwards branch. In the atmosphere, the diabatic forcing is, of course, not confined to two distinct latitudes, but rather is spread throughout the atmosphere. This causes the circulation cells to not be on flat θ_e surfaces but rather to change θ_e with latitude, since the transport is not conservative and the θ_e of air parcels is constantly being changed.

The climatological isentropic mass fluxes, M_ϕ, and streamfunction, ψ, calculated in θ space are shown in the middle row of figure 1.3, and calculated in θ_e space in the bottom row of figure 1.3. Both streamfunctions show a single cell in each hemisphere, transporting both θ and θ_e are transported from the tropics to the poles. The upper branch of the cells is moving relatively high θ and θ_e air polewards and relatively low θ and θ_e air equatorwards.

The streamfunction in θ space $\psi(\phi, \theta)$ fills a large range of θ of about 30-50 K. In contrast, $\psi\left(\phi, \theta_e\right)$ has a more or less constant range of θ_e of 20-30 K throughout the entire atmosphere. The difference in the thickness of the cell in the tropics is analogous to the distribution of the $\overline{\theta}$ and $\overline{\theta_e}$ in the tropics. The mass fluxes in the lower tropical troposphere and upper tropical troposphere are well separated in θ space, but not well separated in θ_e space. The upper bound of the circulation in θ and θ_e is similar, because $\theta_e \approx \theta$ in the upper troposphere.

The difference in the tropical cells can also be viewed in terms of the different tendencies for θ and θ_e

from equation (1.8). Since condensation is so concentrated in the deep tropics, it creates large values of $M_\theta(\phi,\theta)$, which is the vertical component of motion in the (ϕ,θ) space. This has to be partially balanced by an excess of longwave cooling in the subtropics in order to reach θ values observed in the midlatitude troposphere (Trenberth and Stepaniak, 2003b). By contrast, θ_e is conserved during condensation, and so tropical condensation does not appear as vertical motion, explaining the relatively small range of θ_e values that the tropical circulation extends over.

For both $\psi(\phi,\theta)$ and $\psi(\phi,\theta_e)$, the poleward branch slopes downwards in the midlatitudes. This is mainly due to the effects of longwave cooling, which reduces θ and θ_e. To a first approximation the circulation in θ space is capturing the component of the circulation which is in balance with condensation and longwave cooling and the circulation in θ_e space is capturing the component of the circulation which is in balance with evaporation and longwave cooling.

The maximum of $\psi(\phi,\theta_e)$ is about twice the maximum of $\psi(\phi,\theta)$. This implies that the poleward and equatorwards moving airmasses are better separated on θ_e surfaces than they are on θ surfaces (Pauluis et al., 2008, 2010). This difference can be thought about as resulting from the transport of moisture on a dry isentrope or the "moist recirculation" (Laliberté et al., 2012). Consider two air parcels in the boundary layer with the same θ but different moisture contents. On average the moist parcel will undergo convection (either buoyantly driven or mechanically forced by a storm), escape the boundary layer and move polewards, while the dry air parcel will remain inside the boundary layer and move equatorwards. The parcels have the same θ, these motions will cancel out when the circulation is calculated on θ surfaces, but not when calculated on θ_e surfaces. Since the dry and moist air parcels in the boundary layer will have the same θ but different θ_e, which is why the equatorward branch of $\psi(\phi,\theta)$ extends over a narrow range of θ surfaces, but the equatorward branch of $\psi(\phi,\theta_e)$ extends over a relatively wider range of θ_e values. The factor of two difference between the circulations calculated in θ and θ_e space demonstrates the large role that moisture plays in the global circulation.

1.2.4 Statistical Transformed Eulerian Mean (STEM) Circulation

To calculate the streamfunction in thermodynamic space defined in the previous Section requires large amounts of data as the transformation should be done on instantaneous data, with a minimum sampling time of 6 hours to 1 day (e.g. Pauluis et al., 2010; Wu and Pauluis, 2013). A common way to circumvent this requirement is to consider approximations to the circulation based on zonal mean statistics. Perhaps the most used is the Transformed Eulerian Mean (TEM) circulation, initially designed to study wave mean flow interactions in the atmosphere (Andrews and Mcintyre, 1976). In spherical pressure

coordinates the zonal mean TEM can be written as

$$\psi_{TEM} = \psi(\phi, p) + \frac{a\cos\phi}{-g}\frac{\overline{v'\theta'}}{\partial_p\overline{\theta}}, \tag{1.19}$$

which is the first order approximation to the isentropic circulation remapped into pressure space, using the zonal mean thermodynamic surfaces (Juckes, 2001), e.g. the circulation at the point (ϕ, θ) is mapped to $\left(\phi, p\left[\overline{\theta} = \theta\right]\right)$. The second term is the eddy correction needed to bring the circulation in pressure space into agreement with the circulation in θ space. One advantage of the TEM circulation over the explicitly calculated isentropic circulation is that it allows the flow to be separated into a zonal mean and a zonally anomalous, or eddy, component. Since these components have different driving mechanisms it is useful to treat them separately. Both the TEM circulation and the remapping of the isentropic circulation require a monotonic coordinate, i.e. $\partial_p\overline{\theta} > 0$ throughout the atmosphere. Outside of a narrow layer near the surface, this condition is met for $\overline{\theta}$ (addressing the circulation in the surface layer requires additional care, see Held and Schneider, 1999). However, for θ_e this condition is not met except for in the high latitudes, and so the TEM approximation is not useful, e.g. in regions where $\partial_p\overline{\theta_e} = 0$ then ψ_{TEM} is undefined.

The STEM streamfunction avoids this problem by parametrizing the probability density of the flow in thermodynamic space without using the stratification calculated in pressure space. To do this I first write the streamfunction in terms of $m = \partial_p M_\phi(\phi, \theta_e)$. If I consider m to be zonally homogeneous and averaged over many realizations (i.e. a time average) then the mass flux between the surfaces p, $p + dp$ and θ_e, $\theta_e + d\theta_e$, $mdpd\theta_e$, can be written as the expectation value of v given the probability distribution of v and θ_e,

$$mdpd\theta_e = \left[\int vP(v, \theta_e)dv\right] dpd\theta_e. \tag{1.20}$$

To see that this is consistent with the usual definition of the streamfunction, if $P(v, \theta_e) = \delta\left(\theta_e - \theta_e^o\right)$, then the probability distribution collapses to a realization of the observed state, and equation (1.14) is recovered.

The approach of the STEM is to parametrize P as a joint normal probability distribution, i.e.

$$\begin{aligned} P\left(v, \theta_e\right) &= \tfrac{1}{\sqrt{2\pi}}\det\left[\mathrm{cov}\left(v, \theta_e\right)\right]^{-\frac{1}{2}} \exp\left[-\tfrac{1}{2}\begin{pmatrix} v - \overline{v}, & \theta_e - \overline{\theta_e} \end{pmatrix}^T \Sigma^{-1} \begin{pmatrix} v - \overline{v}, & \theta_e - \overline{\theta_e} \end{pmatrix}\right], \\ &\equiv \mathcal{N}\left(v, \theta_e\,;\, (\overline{v}, \overline{\theta_e}), \Sigma\right) \end{aligned} \tag{1.21}$$

where

$$\Sigma = \begin{pmatrix} \overline{v'^2} & \overline{v'\theta'_e} \\ \overline{v'\theta'_e} & \overline{\theta'^2_e} \end{pmatrix}. \tag{1.22}$$

The joint normal pdf can be expressed, after some algebra (e.g. appendix A of Pauluis et al., 2011):

$$\mathcal{N}\left(v, \theta_e\,;\, (\overline{v}, \overline{\theta_e}), \Sigma\right) = \mathcal{N}\left(v, \theta_e\,;\, \overline{v} + \left(\theta_e - \overline{\theta_e}\right) \frac{\overline{v'\theta'_e}}{\overline{\theta'^2_e}}, \frac{|\Sigma|}{\overline{\theta'^2_e}}\right) \mathcal{N}\left(\theta_e\,;\, \overline{\theta_e}, \overline{\theta'^2_e}\right), \tag{1.23}$$

and since the mass flux is the definition of the expectation value, the mass flux on a θ_e surface can be expressed as

$$M_\phi = \int \left(\overline{v} + \left(\theta_e - \overline{\theta_e}\right) \frac{\overline{v'\theta'_e}}{\overline{\theta'^2_e}}\right) \mathcal{N}\left(\overline{\theta_e}\,,\, \overline{\theta'^2_e}\right) \frac{dp}{-g}. \tag{1.24}$$

Unlike the original expression equation (1.11), this can be computed only using the second order statistics. It can also be broken down into two terms, the mean joint massflux m_M which depends on $\overline{v}$, and the eddy joint mass flux, m_E, which depends on $\overline{v'\theta'_e}$. This decomposition is analogous to the TEM circulation, except that m_E does not depend on the mean stratification, $\partial_p \overline{\theta_e}$; instead it depends on $\overline{\theta'^2_e}$.

Putting these expressions into equation (1.14) and completing the integration gives the final expressions for the STEM mean and eddy streamfunctions, similar to (Wu and Pauluis, 2013; Wolfe, 2014),

$$\psi_M = L_x \int_\infty^0 \overline{v} \frac{1}{2} \mathrm{erf}\left(\frac{\theta_e - \overline{\theta_e}}{\sqrt{2\overline{\theta'^2_e}}}\right) \frac{dp}{-g} \tag{1.25}$$

$$\psi_E = L_x \int_\infty^0 \frac{\overline{v'\theta'_e}}{\sqrt{\overline{\theta'^2_e}}} \frac{1}{\sqrt{2\pi}} \exp\left[-\frac{1}{2}\left(\frac{\theta_e - \overline{\theta_e}}{\sqrt{\overline{\theta'^2_e}}}\right)^2\right] \frac{dp}{-g} \tag{1.26}$$

where erf is the usual error function.

I note that the $\psi_E \to 0$ as $\theta_e \to -\infty$ and $\theta_e \to \infty$ but not $\theta_e \to 0$. While the range $\theta_e \in (-\infty, 0)$ is unphysical (since $\theta_e > 0$), it is necessary to include because of the use of the joint normal distribution in parametrizing the STEM, which means that the STEM streamfunction has flow outside of the boundaries where the flow is defined using the exact calculation (Wolfe, 2014). To estimate the amount of flow in the unphysical region, if $\overline{\theta_e}$ is 250K in the lowest layer with $\sqrt{\theta'^2_e}$ of 10K (an underestimate of $\overline{\theta_e}$ and an overestimate of $\sqrt{\theta'^2_e}$ to make a conservative estimate), then $\theta_e = 0$ would correspond to 25 standard deviations, so the total amount of mass flux existing on the unphysical $\theta_e < 0$ s surfaces is very small. Still, this range has to be included in analytic calculations involving the STEM to eliminate boundary

terms that would otherwise occur at $\theta_e = 0$.

Unlike ψ_E it is not apparent that ψ_M conserves mass, since erf does not decay to zero at $-\infty$ or ∞. However,

$$\psi_M(\theta_e \to \pm\infty) = L_x \left(\pm\frac{1}{2}\right) \int_\infty^0 \overline{v} \frac{dp}{-g}, \tag{1.27}$$

so if

$$\int_\infty^0 \overline{v} \frac{dp}{-g} = 0 \tag{1.28}$$

then $\psi_M(\theta_e \to \pm\infty) = 0$. In other words, a distribution of $\overline{v}$ that conserves mass in pressure space will also conserve mass in θ_e space.

The STEM streamfunction reduces to the TEM streamfunction in the limit of low zonal variability (Pauluis et al., 2011). For θ the STEM streamfunction and the TEM streamfunction produce similar streamfunctions. In idealized circulations using Eady waves or a numerical simulation of a Boussinesq fluid in a channel, the STEM is more accurate than the TEM in reconstructing the buoyancy averaged flow (analogous to the flow averaged in thermodynamic space in the atmosphere), but has a small amount of flow in regions outside of the boundaries (Wolfe, 2014). This is because the probability distribution of the flow is Gaussian, and so is nonzero over all possible buoyancy values, not only the ones present in the solution. These small overshoots are generally small and do not contribute much to the total streamfunction (Wolfe, 2014).

Figure 1.5 shows the division of $\psi(\phi, \theta)$ and $\psi(\phi, \theta_e)$ into mean and eddy components. The mean circulation in both θ and θ_e show the expected Hadley, Ferrel, and polar cells. This must be the case, since the isentropic mass flux is proportional to $\overline{v}$, and so the cells must be located at the same latitudes and have the same direction as the mean circulation averaged in pressure space (ψ in figure 1.3 top row). The strength of the mean circulation in θ space is much larger than the strength of the circulation in θ_e space. This could have been anticipated from the distribution of $\overline{\theta}$ and $\overline{\theta_e}$. Zonal mean θ has a strong stratification in the tropics, so that the equatorward and poleward branches of the circulation are well separated on θ surfaces. Zonal mean θ_e has similar values at the bottom and top of the troposphere, so the poleward and equatorward branches of the Hadley cell are not well separated and are mixed together on θ_e surfaces. A similar differentiation can be made between the vertical motion in the two thermodynamic spaces; condensation contributes to $\dot{\theta}$ and so will appear as vertical motion in θ space, but will not appear in vertical motion in θ_e space. The relative difference of the mean circulation between θ and θ_e spaces is also related to the difference between the sensible and latent heat transports

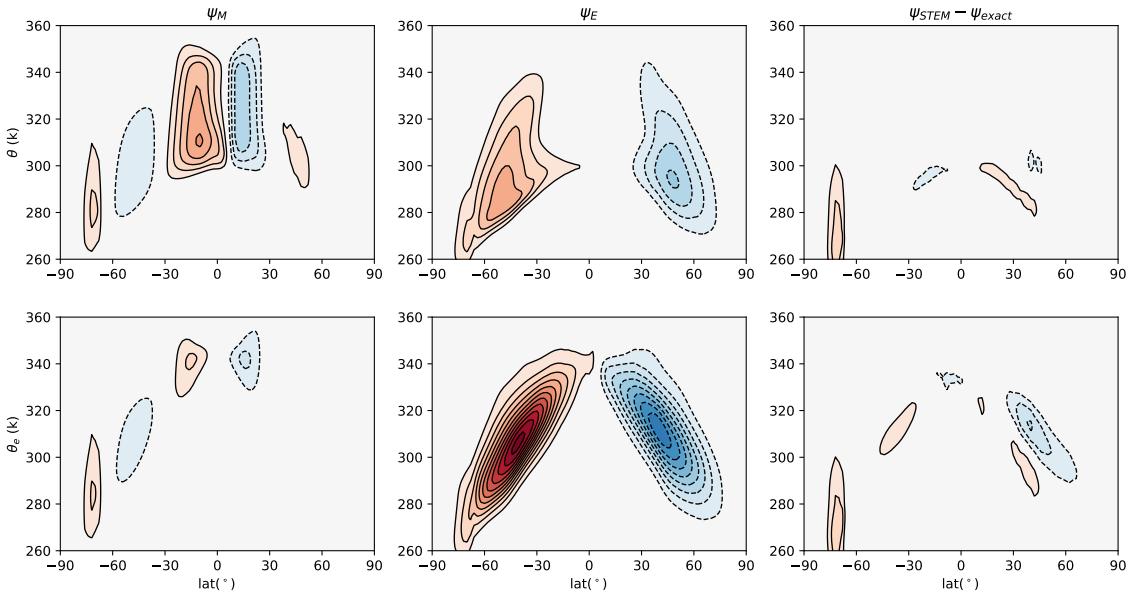

Figure 1.5: Zonal and annual mean climatologies of the STEM mean (left) and eddy (center), streamfunctions in θ (top) and θ_e (bottom) space for ERA5 reanalysis. The right column shows the differences between the streamfunctions calculated using the exact expression (equation 1.15) and the STEM parametrization (equation 1.26). The contour interval is the same as in figure 1.3.

in the Hadley cell. The lower branch of the Hadley cell transports latent heat into the tropics, where condensation and subsequent sensible heat transport by the upper branch of the Hadely cell happens afterwards. These transports partially cancel, similar to the circulation in θ_e space. It should be noted that the weakness of the Hadley cells in figure 1.5 is because they are calculated over an annual mean; the Hadley cell appears more prominently in both θ and θ_e spaces in seasonal averages (Pauluis et al., 2011).

The eddy circulation shows a clear division between the tropics and the midlatitudes in θ space, whereas in the θ_e space the eddy streamfunction extends all the way into the tropics. In fact, for the streamfunction in θ_e space the eddy streamfunction dominates the entire circulation. The eddy transport of water vapor, particularly through stationary waves, plays a large role in maintaining the eddy streamfunction in the tropics (Shaw and Pauluis, 2012).

The difference between the total STEM streamfunction, e.g. the sum of (1.26) and (1.26), and the exact streamfunction calculated using (1.14), is shown in the right column of figure 1.5. The largest differences are in the northern hemisphere, where the streamfunction calculated with the STEM is about 5%-10% stronger than the streamfunction using the exact formula. The other notable difference is in the southern hemisphere, over Antartica, where the exact streamfuncton is not closed. This is likely due to an error with the vertical interpolation near topography not conserving mass.

In summary, the STEM streamfunction allows us to estimate the streamfunction in any thermodynamic quantity from first and second order zonal mean statistics. This provides a huge computational advantage, since the streamfunction can be calculated using only zonal mean data, which can also be averaged over longer time periods. In addition, the STEM formulation allows the circulation to be divided into mean and eddy components, and the STEM relates the circulation in thermodynamic space to functions calculated in pressure space. This functional dependence can be exploited to gain additional diagnostic information about the sensitivity of the circulation, which we will investigate in Chapter 3.

1.2.5 Total Heat and Mass Transports

Using the approximation that MSE $= C_P\theta_e$, the total atmospheric heat transport can be determined from pressure space by vertically integrating the mean and eddy meridional fluxes:

$$\begin{aligned} H^T_{\theta_e} &= C_p L_x \int \left(\overline{v}\,\overline{\theta_e} + \overline{v'\theta'_e}\right) \frac{dp}{-g} \\ &= H^M_{\theta_e} + H^E_{\theta_e}, \end{aligned} \tag{1.29}$$

where H^T is the total transport, H^M is the mean transport, and H^E is the eddy transport.

This can also be determined from the mass fluxes in the thermodynamic space (Döös and Nilsson, 2011) by using the relationship $M = -\partial_{\theta_e}\psi$ and

$$H^T_{\theta_e} = C_p L_x \int_0^\infty M\theta_e d\theta_e, \tag{1.30}$$

and assuming that the streamfunction is closed so that $\lim_{\theta_e\to\infty}\psi = 0$ and $\psi(\theta_e = 0) = 0$ and integrating by parts it can be demonstrated that

$$H^T_{\theta_e} = C_p \int_0^\infty \psi d\theta_e. \tag{1.31}$$

This is shown in figure 1.6 for both θ and θ_e. In the tropics, the dominant transport of θ happens through H^M, while H^M plays a smaller role in the transport of θ_e. This is due to the compensation of moist and dry energy transport in the Hadley cell. The lower branch of the Hadley cell transports moist air towards the equator, where it is condensed and removed from the atmosphere. The condensational heating increases θ in the upper branch, which exports it from tropics and into the midlatitudes, where it is transported further polewards by the atmospheric eddies (Trenberth and Stepaniak, 2003b). The total transport of θ_e is dominated by the eddy transport globally.

The partitioning of the flow between mean and eddy components mirrors the partioning of the STEM mean and eddy streamfunctions. This is because the total integrated STEM streamfunctions match the mean and eddy transports calculated in pressure space. This can be shown by integrating equations (1.26) between $-\infty$ and ∞. Including the range $\theta_e \in (-\infty, 0)$ in the integral is necessary to remove the boundary term that would otherwise be present from $\psi(\theta_e = 0)$.

Noting that

$$\begin{aligned}\int_{-T}^{T} \operatorname{erf}\left(\frac{\theta_e-\overline{\theta_e}}{\sqrt{\overline{\theta_e'^2}}}\right) d\theta_e = \;& \frac{\overline{\theta_e}}{2}\left[\operatorname{erf}\left(\frac{T+\overline{\theta_e}}{\sqrt{\overline{\theta_e'^2}}}\right) - \operatorname{erf}\left(\frac{T-\overline{\theta_e}}{\sqrt{\overline{\theta_e'^2}}}\right)\right] \\ & + \frac{\sqrt{\overline{\theta_e'^2}}}{\sqrt{\pi}}\left[\exp\left(-\left[\frac{T-\overline{\theta_e}}{\sqrt{\overline{\theta_e'^2}}}\right]^2\right) - \exp\left(-\left[\frac{T+\overline{\theta_e}}{\sqrt{\overline{\theta_e'^2}}}\right]^2\right)\right]\end{aligned} \tag{1.32}$$

then

$$\begin{aligned} H^M &= C_p \textstyle\int_{-\infty}^{\infty} \psi_M d\theta_e \\ &= C_p L_x \textstyle\int_{\infty}^{0} \frac{\overline{v}}{2} \int_{-\infty}^{\infty} \operatorname{erf}\left(\frac{\theta_e-\overline{\theta_e}}{\sqrt{2\overline{\theta_e'^2}}}\right) d\theta_e \frac{dp}{-g} \\ &= C_p L_x \textstyle\int_{\infty}^{0} \overline{v}\,\overline{\theta_e} \frac{dp}{-g}, \end{aligned} \tag{1.33}$$

so the heatflux from the STEM mean streamfunction agrees with the mean heatflux computed in pressure space. Similarly

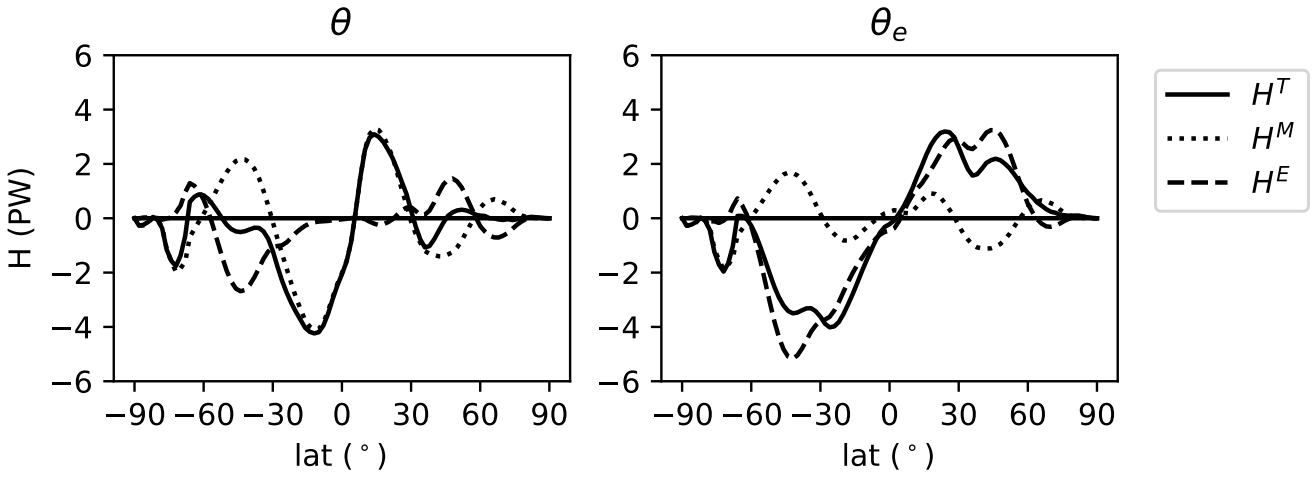

Figure 1.6: Vertically integrated annual mean heat transport calculated using θ (left), and θ_e (right) from the ERA5 reanalysis.

$$\begin{aligned} H^E &= C_p \int_{-\infty}^{\infty} \psi_E d\theta_e \\ &= C_p L_x \int_{\infty}^{0} \frac{\overline{v'\theta'_e}}{\sqrt{\overline{\theta'^2_e}}} \int_{-\infty}^{\infty} \frac{1}{\sqrt{2\pi}} \exp\left[-\frac{1}{2}\left(\frac{\theta_e - \overline{\theta_e}}{\sqrt{\overline{\theta'^2_e}}}\right)^2\right] d\theta_e \frac{dp}{-g} \\ &= C_p L_x \int_{\infty}^{0} \overline{v'\theta'_e} \frac{dp}{-g}, \end{aligned} \tag{1.34}$$

where the last line is accomplished using a Gaussian identity. This proves that the STEM eddy streamfunction agrees with the eddy heatflux computed in pressure space.

1.3 Summary and Remaining Science Questions

The main themes of the preceding discussion can be summarized into a few key points:

1. The size of energy transfers into and from the atmosphere point to latent heating as a key mechanism for adding heat to the atmosphere and linking surface heating to atmospheric heating.

2. The difference between θ and θ_e is related to storage and transport of water vapor in the atmosphere, θ treats latent heating as an external heat source, while θ_e implicitly accounts for when water vapor is added to the atmosphere.

3. Analyzing the global circulation in thermodynamic phase spaces finds the component of the mass transport that is needed to balance the thermodynamic transformations in the atmosphere, regardless of whether the transport is occurring through the zonal mean circulation or eddies. The circulation in thermodynamic space is a single global cell with poleward and equatorward branches; the circulation in θ_e space is stronger than the circulation in θ space because the poleward and equatorward branches are better separated.

4. The STEM circulations parameterizes the circulation in a thermodynamic space using second order zonally averaged statistics calculated in pressure space, and it separates the circulation into a zonal mean and eddy component with heatfluxes corresponding to the vertically integrated heat fluxes computed in pressure space.

A major theme of this discussion is quantifying the effects of latent heating on the transport of the troposphere. The reason this is challenging is because latent heating only happens after water vapor becomes saturated; usually requiring the water vapor to be transported vertically first. This results in latent heating being coupled to the dynamics of the troposphere, which significantly complicates how its role in the global circulation is understood. In this thesis I explore some different means of quantifying

the effect of the coupling between the hydrological cycle and the transport of mass and heat by the global circulation and use them to improve the understanding of the global climate system.

In Chapters 2 and 4 I make use of two different versions of an idealized moist model (IMM) to study the effects of latent heating in the global circulation in a simplified setting. The motivation for using IMMs is to study the effects of latent heating on transport in a statistically steady setting without any zonal asymmetries in order to gain insight into the zonal mean transport in a simpler settings. The IMMs (used in this thesis) are based originally on the moist model of Frierson et al. (2006), and later expanded by Frierson (2007); O'Gorman and Schneider (2008) and Vallis et al. (2018). These IMMs are best understood as a spectral dynamical core which solves the dynamical equations, with some minimalistic parametrizations and boundary conditions included. This approach can be contrasted with simplified models created by modifying the boundary conditions of more comprehensive models (e.g. Neale and Hoskins, 2000; Lee et al., 2008; Medeiros et al., 2016). The model is best summarized as a cloudless, greybody, aquaplanet. In more detail, the model has:

1. Water vapor, which is modelled by a passive tracer which modifies the density of the atmosphere (e.g. virtual temperature is used to calculate hydrostatic pressure), and which adds latent heat to the atmosphere when saturation is achieved. Additionally, a convection scheme is included which simulates convection by relaxing the atmosphere to a moist adiabatic profile when the liquid and solid water are not included in the model, and it is assumed that water vapor is instantly removed from the atmosphere (a modification made by O'Gorman and Schneider, 2008). This also precludes using these models from studying cloud processes.

2. A two stream, greybody radiative transfer model, which assumes that the optical depth is parametrized as a function of latitude, pressure and additionally in Chapter 4, of water vapor and a nominal CO_2 value (Vallis et al., 2018). The radiative transfer includes both thermal radiation as well as absorption of shortwave radiation; the shortwave function at the top of the atmosphere is chosen to be only a function of latitude, so there is no diurnal or seasonal cycle in the model.

3. A thermodynamic ocean layer, which assumes a uniform temperature profile, prognostically calculated through the energy balance at the surface, and which does not freeze. Turbulent fluxes from the surface create an evaporative flux of water vapor as well as a sensible heat flux, the temperature of the ocean layer is used as a boundary condition for the long wave scheme in the radiative transfer, and a nominal albedo is included to reflect shortwave radiation. On long time scales, since the temperature of the ocean layer is used for the upwards longwave flux, the ocean temperature adjusts until the outgoing longwave radiation balances the net energy input from insolation and

atmospheric fluxes.

The main difference between the IMMs in Chapter 2 and Chapter 4 is in the radiation scheme. In Chapter 2 water vapor does not affect the opitcal depth, and therefore the radiative heating and cooling inside the atmosphere, while in Chapter 4 it does. This choice was made to try to have a more realistic distribution of radiative cooling in the tropics, which is important for modelling the distribution of tracers of diabatic heating, as explained in Chapter 4.

One aspect of the model that is not particularly realistic of the model is the stratosphere. The shortwave absorption in the stratosphere is only a function of pressure in the original grey body model (O'Gorman and Schneider, 2008), and does not model the distribution of ozone leading to an inaccurate distribution of shortwave heating and unrealistically long radiative damping timescales (Jucker and Gerber, 2017). Additionally, since the model lacks any representation of the seasonal cycle, the model does not form a strong polar vortex in the winter hemisphere. Since the main focus of the thesis is on the effects of latent heating, which almost exclusively takes place inside of the tropspohere, these simplifications are acceptable for our purposes.

In Chapter 2 I investigate how the distribution of zonal mean θ_e can be used to understand the linkage between the midlatitude surface and the polar midtroposphere. This linkage has been studied in observations by Laliberté and Kushner (2014), who found correlations between θ_e in the midlatitude near surface and the Arctic midtroposphere during August in reanalysis products. I force the an idealized aquaplanet model (described above) with midlatitude surface heating to create θ_e surface anomalies in the midlatitude troposphere. Our goal is to track these anomalies through the atmosphere, and compare their transport between θ and θ_e surfaces through the troposphere to identify the role of latent heating in creating this linkage. The size and location of the SST anomalies is varied in order to test the response of different regions of the atmosphere. This work has been published in the Journal of the Atmospheric Sciences (Fajber et al., 2018).

In Chapter 3 I develop and explore a theory to explain the sensitivity of the STEM circulation in θ_e space to perturbations in climate change simulations. Since the STEM streamfunction in θ_e space relates the circulation in θ_e space to statistics related to the mean and eddy heat transport, it is an ideal tool for studying the link between the circulation in θ_e space, the global heat transport, and the eddy statistics. Calculating the sensitivity kernels of the STEM streamfunction finds the sensitivity of the circulation in θ_e space to perturbations in the mean thermodynamic state ($\overline{\theta_e}$) and dynamical perturbations $\left(\overline{v}, \overline{v'\theta'_e}, \overline{\theta'^2_e}\right)$. Additionally, this framework clarifies the linearization technique first developed by Wu and Pauluis (2013) and used by Fajber et al. (2018), and explains the similarities between different

experiments. Our results point to the zonal variability of θ_e, $\overline{\theta_e'^2}$, as key to controlling the sensitivity of the circulation to perturbations, and that this is not well constrained between two modern reanalysis products. This work is in preparation to be submitted to the peer-reviewed literature.

In Chapter 4 I introduce a passive tracer method, called heat tagging, for partitioning the θ content of the atmosphere by source, and apply it to an idealized aquaplanet model (similar to the model used in Chapter 2, but adapted by Vallis et al., 2018). Budgets that balance local diabatic sources with local heat divergence and storage do not retain information about the influence of remote regions, which requires air-mass tracking. Heat tagging locally decomposes the potential temperature into contributions from the distinctive diabatic processes that generate them, wherever they occur. The distribution, variability, transport, and sensitivity to climate perturbations of the atmospheric heat tag distribution is studied in the relatively simple setting of an idealized aquaplanet model. The heat tags are also used to isolate the component of heat transport related to the hydrological cycle; this creates a new decomposition of the poleward heat transport which naturally removes the apparent competition between water vapor convergence and dry heat divergence in the tropics. This work is also in preparation to be submitted to the peer-reviewed literature.

In Chapter 5 I argue that these techniques could be implemented in modern general circulation models. Throughout this thesis care is taken to work within common modelling frameworks with the intention that these studies be used as proof of concept studies for implementing them in more comprehensive climate models. I also include some future research directions for follow up studies on the ideas of this study.

Chapter 2

Influence of Midlatitude Surface Thermal Anomalies on the Polar Midtroposphere in an Idealized Moist Model

A version of this work has been previously published; see Fajber et al. (2018).

2.1 Introduction

Recent warming trends in the Arctic show a surface maximum, but also extend broadly into the vertical in all seasons (Screen and Simmonds, 2010). However, the warming that occurs at the Arctic surface and the Arctic mid troposphere (AMT) may not be causally connected. Studies using atmospheric general circulation models with forced with Sea Surface Temperature (SST) anomalies due to Arctic sea ice loss show thermal responses that are confined to near the Arctic surface (Screen et al., 2012; Perlwitz et al., 2015). The inability of the Arctic surface heating to warm the AMT suggests that an alternative pathway is needed to explain trends in the AMT. Tracer transport modeling has shown that much of the air residing in the AMT last made contact with the surface in the midlatitudes, with a large fraction of air produced at the Arctic surface unable to penetrate above the Arctic planetary boundary layer (Orbe et al., 2015a). This suggests that warm, moist air originating in the at or near the surface in

the midlatitudes, a region we will refer to as the midlatitude near surface (MNS), can be carried to the AMT, potentially having an influence on its heat content.

The possibility of MNS air influencing AMT temperatures on global warming time scales was studied by Laliberté and Kushner (2013), who found that projected AMT heating under a forced climate change could be constrained by MNS heating through a simple model of isentropic homogenization. Notably, this simple isentropic homogenization needed to include both surface warming and moistening to constrain the AMT response. This suggests that latent heating in the midlatitudes helps determine the connection between the MNS and the AMT. This idea was further explored by Laliberté and Kushner (2014), who used reanalysis data to study the connection on intraseasonal time scales. Their study found a connection between the MNS and the AMT in boreal summer that provides the main source of instraseasonal, interannual and decadal AMT variability during these months, and that the MNS anomaly leads the AMT anomaly by approximately a month. It is important to note that this transport pathway and potential warming mechanism are best explained by considering the impacts of sensible and latent heat transport jointly. If only sensible heat anomalies are considered; the MNS variability is too small, by approximately a factor of two, to explain the heat anomalies seen in the AMT.

Moisture plays a role in establishing this connection by warming the atmosphere through latent heating in the midlatitude atmosphere. Condensation of water vapor typically happens in the warm cores of extratropical cyclones, where warm moist air from the surface is raised to the condensation level (Schemm et al., 2013). The release of latent heat further increases the buoyancy of the air, and results in increased uplift. Latent heat transport by eddies also accounts for a significant fraction of the atmospheric heat transport in the midlatitudes (Döös and Nilsson, 2011; Shaw and Pauluis, 2012).

Since dry potential temperature (θ) does not implicitly include the impacts of latent heating, condensation will appear as a source of θ, and so it will not be conserved wherever the air becomes saturated. In order to account for the effects of latent heating on the atmospheric circulation in the midlatitudes it is convenient to use the equivalent potential temperature (θ_e) that will be conserved under condensation. These conservation properties make θ_e a useful variable to study the transport of air between the MNS and the AMT in a way that implicitly accounts for the static stability felt by air parcels as they move upwards through extratropical cyclones (Juckes, 2000; Frierson and Davis, 2011; Wu and Pauluis, 2014).

Our study is aimed at understanding the dynamics associated with the connection between the MNS and the AMT on intraseasonal time scales. To do this, we use an idealized moist model (IMM; originally described in Frierson et al., 2006), to isolate the transport pathway. The IMM simulates the primitive equations with simplified physical parameterizations of moisture and radiation that allow us to analyze the pathway between the MNS and the AMT in a relatively simple setting. The choice of this idealized

model is to provide a minimal model capable of producing the observed connection between the AMT and the MNS. Our goal is not to characterize the IMM; rather we are attempting to provide a test of moist isentropic propagation mechanism hypothesized in Laliberté and Kushner (2014) to operate on intraseasonal time scales.

In section 2.2, we describe a new experimental setup for the IMM that creates an extratropical atmosphere with qualitatively realistic extratropical stratification while avoiding large surface energy imbalances. The transient adjustment of the atmosphere to switch-on zonally symmetric midlatiutde heating perturbations is then studied. By perturbing the model in this way and studying only transient effects, we have more direct control over the perturbation and responses than if we allow for a long term adjustment of the atmosphere.

In section 2.3, we analyze both the response of the polar midtroposphere (PMT; since the model is hemispherically symmetric we do not distinguish between the two hemispheres) in the IMM as well as the extratropical troposphere as a whole. We look at anomalies between the transient ensemble averaged over days 10-20 and the control simulation to characterize the transient response to the surface perturbation. Calculating the distribution of these anomalies allows us to test the statistical significance of the results. We also investigate the impacts of the surface perturbation on the eddy covariance $\overline{v'\theta'_e}$ and the bulk stability of the atmosphere. Throughout, we compare dry and moist perspectives on the circulation response.

In section 2.4, we follow Pauluis et al. (2011) to calculate the eddy driven circulation in θ_e coordinates. Using θ_e as a coordinate to compute the poleward eddy mass transport separates the warm and moist air parcels from the comparatively warm but dry parcels. Similar results are obtained using moist static energy instead of θ_e (Döös and Nilsson, 2011), however in this study we will use θ_e to facilitate previous studies with reanalysis (Laliberté and Kushner, 2014). We then decompose the response of the streamfunction by utilizing the functional dependence established by the statistical transformed Eulerian mean (STEM) circulation. This analysis allows us to separate the impacts of the mean thermodynamic anomalies and the eddy anomalies on both the isentropic mass flux and the total heat transport.

In section 2.5, the main conclusions of this Chapter will be summarized. We will also raise some limitations of the study and propose possible future research directions.

2.2 Methods

2.2.1 Idealized Moist Model (IMM)

The IMM used here has a spectral atmospheric dynamical core with a two stream radiation transfer scheme and a surface energy balance boundary condition (initially described in Frierson et al., 2006). The surface is a zonally symmetric ocean mixed layer of 40m depth. The IMM water-like tracer is passive until it reaches saturation, as computed from the Clausius Clapeyron relation. Upon saturation, the tracer releases latent heat; the condensate is then removed immediately from the model. Freeze and melt processes are not included in the model, even below the freezing point. Due to these simplifications we use the pseudoadiabatic θ_e in our diagnoses (see subsection 1.2.1 for more details). A simplified Betts-Miller convection scheme is used to model subgrid scale convection [for the original description of the scheme see Betts (1986); here we used the "shallower "option described in Frierson (2007)]. Because the condensate is removed instantaneously, no clouds are formed. The radiative transfer scheme assumes that the vertical optical depth is fixed, which makes water vapor radiatively inactive. The current version of the model can be downloaded from climate-dynamics.org/software. It should be noted that these experiments were done with a previous version, although it is not expected that current updates would have a significant impact on our results; the only update relevant to our runs is a small change in the tracer damping scheme. The model is run with T85 horizontal resolution, 30 vertical levels, and 8^{th} order resolution-dependent hyperdiffusion, with a base damping coeffecient of $2.32 \times 10^{-5}\text{s}^{-1}$.

2.2.2 Surface Boundary Condition

Typically the IMM is run with a energy balance surface condition in which the SST at the lower boundary evolves according to:

$$C\frac{\partial}{\partial t}T_s = -I_\uparrow + I_\downarrow + (1-\alpha)S_\downarrow - H + Q, \tag{2.1}$$

where C is the heat capacity of the mixed ocean layer (of depth 40m), T_s is the SST, $I_\uparrow$ and $I_\downarrow$ are the upward and downward longwave fluxes respectively, $S_\downarrow$ is the shortwave downward flux, H is the surface turbulent energy flux to the atmosphere, and Q is an imposed heat flux (Frierson et al., 2006; O'Gorman and Schneider, 2008).

To constrain the climate and surface perturbations that we impose, we use an imposed meridional SST profile $T_s(\phi)$ which sets the left hand side of equation (2.1) to zero. However since $I_\uparrow$ is determined by T_s, the terms on the right hand side of (2.1) will not in general be balanced unless the imposed Q flux

is not zero. Imposing an SST profile is thus equivalent to imposing a heat source or sink in the model. On the other hand, if the SST profile is chosen to be one in surface energy balance, for which the non-Q terms on the right hand side of (2.1) sum to zero, then the time mean of (2.1) can be self-consistently zero with Q itself set to zero.

These considerations suggest a method for determining the SST profile we use to generate the control state for our perturbation experiments. First we run the IMM using the energy balance surface condition using equation (2.1), then we take the zonal and time averaged SSTs from this run as our imposed control SST profile. In this study, the IMM is run with a constant, equinoctial, hemispherically symmetric distribution of solar radiation, without seasonal or diurnal cycle (O'Gorman and Schneider, 2008). The model is run for 1800 days, with the last 1080 days used for averaging. We choose $T_s(\phi)$ to be hemispherically symmetric so we can average over both hemispheres and increase our sample size. The model is then run with SSTs fixed to this profile for 4320 days, with the last 3600 days used for generating initial conditions for the perturbation ensemble described in the next section.

The final control SST profile that is obtained using this method disagrees in some respects with the observed SSTs (top row of figure 2.1). We note that the since the ocean mixed layer is a homogeneous layer, so the SST is the temperature that the surface radiates with. This is an important difference with the real world, where water below freezing will form ice, and the temperature of the ice will become the temperature that the surface radiates with, while the SST will remain at the freezing temperature. Since the ocean layer in this model does not freeze and the temperature within the mixed layer is constant, and $I_\uparrow$ is lower than what can be obtained at the freezing temperature, the SSTs are much lower than what is observed. In particular, the SST gradient is stronger than observed in the extratropics, and the SST goes below freezing at the pole (consistent with the model not including sea ice). The SST profile does, however resemble the SSTs seen in aquaplanet GCMs with more realistic atmospheric radiative transfer and physical parametrizations using a similar energy balance boundary condition (see figure 1a in Lee et al., 2008). With the imposed SST profile the atmosphere spins up relatively quickly; after approximately 180 days the imposed SST simulation is in a similar state to the energy balance surface condition simulation after 720 days. This is due to the use of fixed SST boundary conditions and the lack of diurnal or seasonal cycle in the atmosphere. The initial time to spin up is therefore solely determined by the atmosphere experiencing constant forcing, which is much faster than if the boundary layer had to equilibriate or had to undergo multiple seasonal cycles.

The simulated distribution of the zonal mean θ_e, $\overline{\theta_e}$ (here and throughout the text we use $\overline{A}$ to denote the zonal average of A and $A' = A - \overline{A}$) in the mid and high latitudes is qualitatively similar to observations in the energy balance surface condition (bottom row of figure 2.1). In particular, the

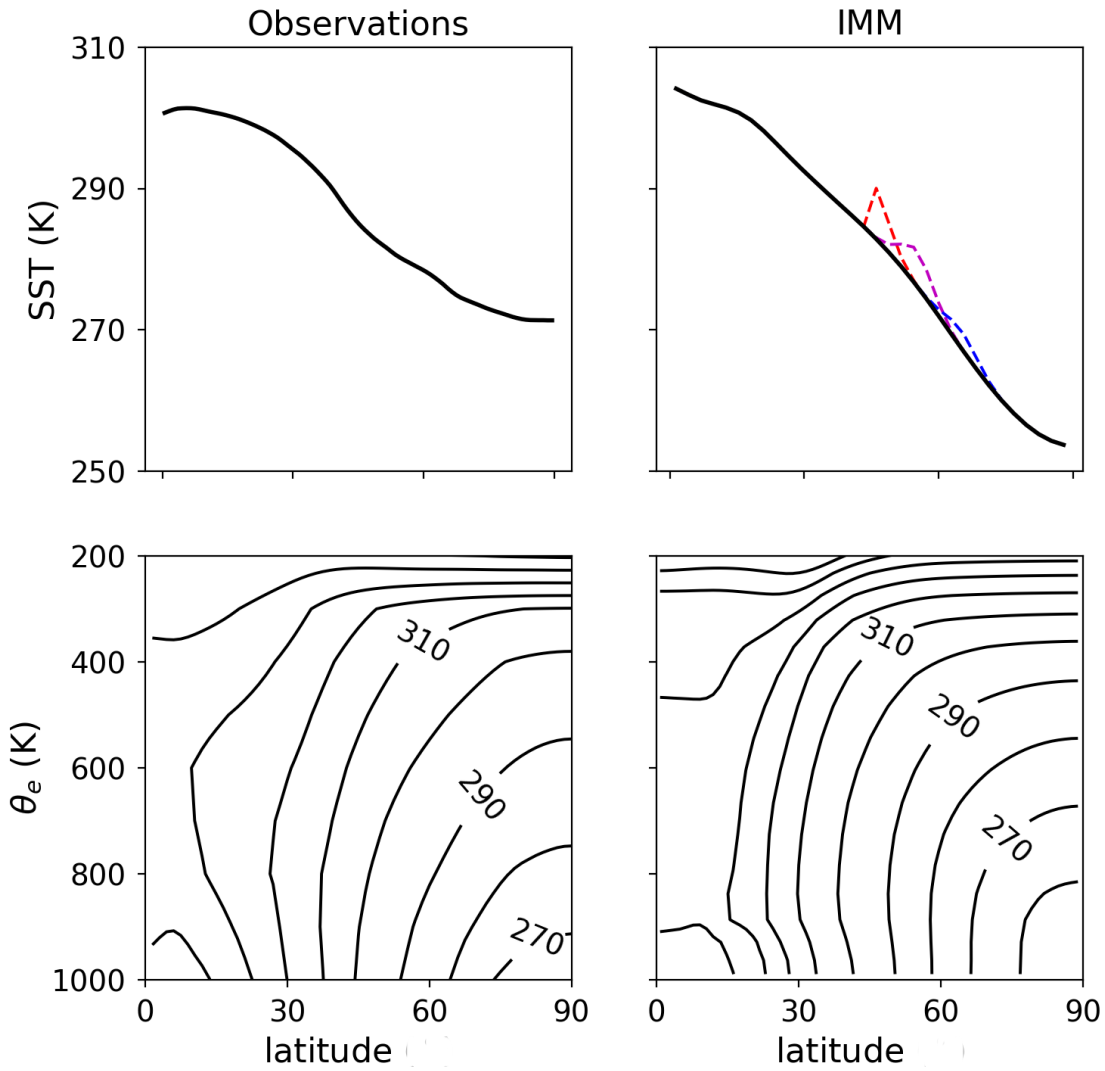

Figure 2.1: Top row: annual and zonal mean SSTs from the NOAA Optimum Interpolation Sea Surface Temperatures V2 (Reynolds et al., 2002) left, and time and zonally averaged SSTs from the IMM energy balance surface condition, right. This latter SST profile is used for all experiments shown in this study. The right panel also shows a sample of the perturbations used to generate the initial condition ensemble: $\delta T = 7.5$K, $\phi_0 = 45°$ (red dashed); $\delta T = 5.0$K, $\phi_0 = 55°$ (purple dashed); $\delta T = 2.5$K, $\phi_0 = 65°$(blue dashed). Bottom row: the annual mean zonal mean distribution of $\overline{\theta_e}$ from the ERA Interim reanalysis product (Dee et al., 2011) left, and from the IMM run with the imposed control SST profile used in this study, right. The contour interval is 10K.

tropics are unstably stratified, the midlatitudes have a near-neutral stability, and the poles are stably stratified. We note an approximate 10K cold bias at the polar surface. Although these control SSTs driving these simulations are qualitatively different from observations, they give rise to a qualitatively realistic distribution of $\overline{\theta_e}$ that we will explore in our analysis.

When the imposed SST model is instead driven by annual mean observed SSTs (shown in the top left panel of figure 2.1), the polar atmosphere becomes unstably stratified, and a polar thermally direct cell (similar to the Tropics) forms. This difference arises because the polar ocean surface is near freezing, which is warmer than the sub-freezing SSTs required by energy balance. Imposing this SST profile in the IMM is thus equivalent to creating a large Q in equation (2.1) in the polar regions. The energy imbalance is then transferred into the atmosphere through sensible and latent heat fluxes which destabilize the atmosphere and drive a thermally direct circulation. We will therefore use the energy balance profile as our control profile, $T_s^0(\phi)$, for all of the following experiments.

2.2.3 Initial Condition Ensembles

A number of perturbation experiments were then created using Gaussian shaped zonally symmetric SST perturbations added to the control profile:

$$T_s(\phi) = T_s^0(\phi) + \delta T \exp\left(-\frac{1}{2}\left(\frac{|\phi - \phi_0|}{\Delta\phi}\right)^2\right) \tag{2.2}$$

where δT is the amplitude of the perturbation, ϕ_0 is the center of the perturbation, and $\Delta\phi$ is the width of the perturbation. By construction both the initial SST profile as well as the SST perturbation are zonally symmetric.

The values of ϕ_0 used are 45°, 55° and 65°; the values of δT used are 2.5K, 5.0K, 7.5K; and the value of $\Delta\phi$ used is 5°. This generates a total of 9 experiments (see the upper right panel in figure 2.1 for three examples).

The shape and width of the perturbations were chosen so that the SST perturbations were sufficiently localized while still being well resolved by the IMM. The location of the perturbations were chosen to test the impact of displacement from the pole and the overlying stratification above the SST anomaly. At $\phi_0 = 45°$ the tropospheric column is in a weakly unstable regime, at $\phi_0 = 55°$ the tropospheric column is in a weakly stable regime, and at $\phi_0 = 65°$ the tropospheric column is in a strongly stable regime. The values of δT were chosen to range from approximately one standard deviation of the daily SST in the energy balance surface condition to the maximum SST deviation from the mean SST in this integration.

Initial condition ensembles were created by taking an initial state from the final 10 years of the control experiment, instantaneously applying an SST perturbation, and then integrating for 90 days. The initial states were chosen to be 30 days apart. We assume this to be sufficient to gaurentee independence, since the e-folding decay times of zonal mean θ_e is approximately 2 weeks. This choice results in each initial condition ensemble consisting of 120 members.

2.3 Atmospheric response to surface heating

2.3.1 Thermal and moisture response

The ensemble-mean response of the atmosphere averaged over the polar caps (defined here as latitudes poleward of 75°) shows a transient response in both θ_e and specific humidity q to imposed midlatitude SST perturbations (shown for the $\delta T = 7.5K$ experiments in figure 2.2; other experiments are similar). An initial response of θ_e occurs in the PMT that peaks between 10 and 20 days. Importantly, the response in the PMT is not preceded by a surface signal. The specific humidity response occurs at the same time as the response in θ_e but its maximum occurs lower in the troposphere.

After 30 days, the polar cap response begins to drift away from the model mean state, as seen by the large warming seen, for example, at the top of the tropopause in the top panel of figure 2.2. This suggests using a 10-20 day period to capture the initial transient development of the response to midlatitude warming, before the model evolves to a different mean state. This is why we limit our analysis to results after the first 10-20 days, so that the difference between the perturbed climate and the control climate can be interpreted as the transient respose to this warming.

Next we look at the distribution of $\overline{\theta_e}$ averaged over days 10-20 to identify the features of the circulation that lead to the development of the PMT response (figure 2.3). All of the responses are positive and extend to the PMT. This corresponds to a warming and moistening of air in this region. These responses have a large horizontal scale; for example in the $\phi_0 = 45°$ experiments, the horizontal length between the SST perturbation and the pole corresponds to just under 15% of the circumference of the globe.

The strength of the response is approximately proportional to the strength of the surface perturbation. Moving from top to bottom in figure 2.3 shows a strengthening of both the MNS response and the PMT response. However, the vertical extent of the $\overline{\theta_e}$ responses above the MNS remains roughly the same for all perturbation amplitudes δT at a given ϕ_0.

The structure of the response depends strongly on where the perturbation is located. For example,

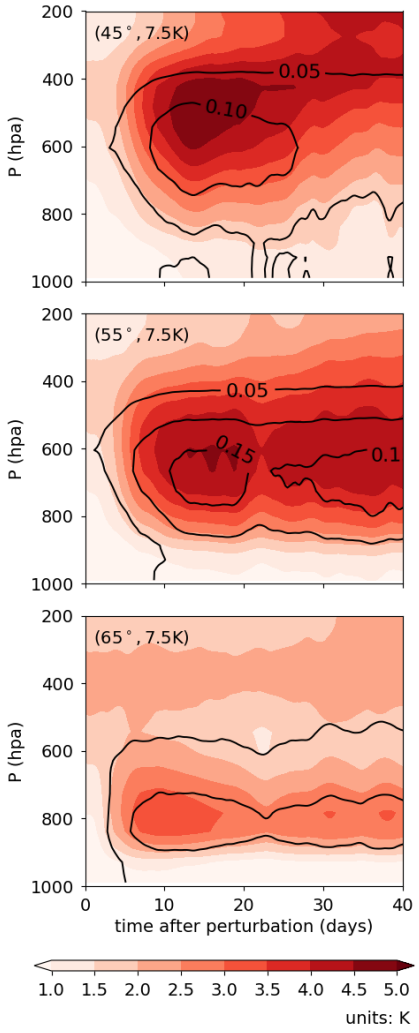

Figure 2.2: The time series of the ensemble mean atmospheric response of θ_e (filled contours; units of K) and q (black contours; units of $\mathrm{g\,kg^{-1}}$) averaged over the polar cap for the $\delta T = 7.5$K experiments. From top to bottom, for perturbations located at $\phi_0 = 45°$, $\phi_0 = 55°$ and $\phi_0 = 65°$.

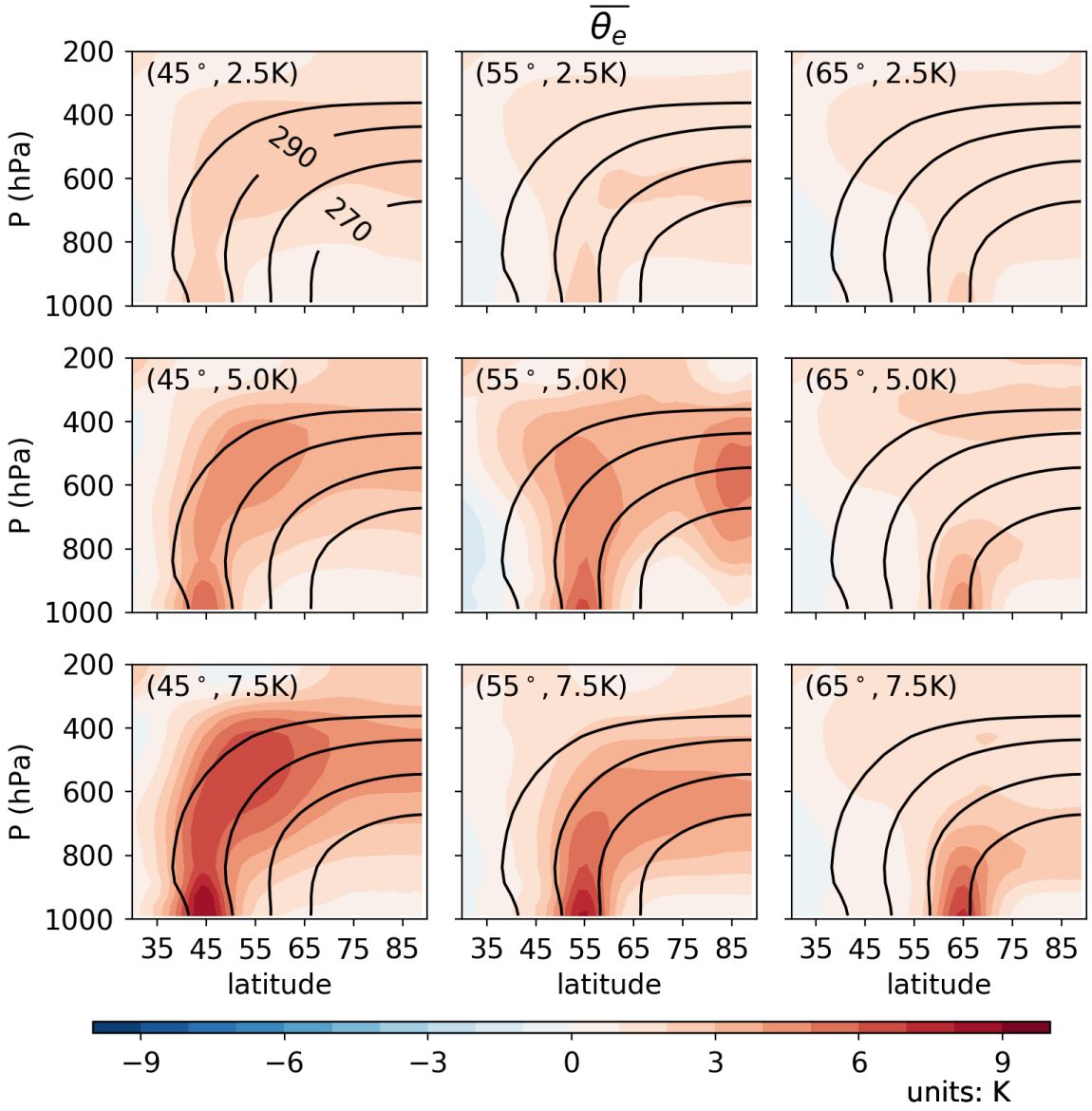

Figure 2.3: The response in zonal and time mean potential temperature, $\overline{\theta_e}$, represented as the difference between the ensemble time mean over days 10-20 and the control climatology (shading), and the control climatology of $\overline{\theta_e}$ (black contours; contour interval is 10K starting with 270K).

for $\delta T = 7.5$K, the $\phi_0 = 45°$, 55°, 65° perturbation responses extend vertically to 400, 500 and 700 hPa above the perturbed region and then propogate poleward and achieve maximum PMT responses at 500, 600, and 800 hPa. For the $\delta T = 5.0$K and 2.5K cases a similar structure is observed, although the signal is not as clear. The responses of $\overline{\theta_e}$ that occur highest in the PMT are from the most distant locations.

The magnitude of the near-surface response is also dependent on the location of the perturbation. The closer the SST perturbation is to the equator, the larger the near surface response of $\overline{\theta_e}$. This is due to Clausius-Clapeyron scaling. Since the background SSTs are warmer near the equator, a SST perturbation creates a larger perturbation of $\overline{\theta_e}$ since θ_e incorporates both the warming and the moistening of the surface air.

To further understand the impacts of the near-surface increase in $\overline{\theta_e}$, we contrast it with the response of dry $\overline{\theta}$ for the $\delta T = 7.5$K experiments (figure 2.4; top row). The response of dry $\overline{\theta}$ for the $\phi_0 = 45°$ perturbation experiment shows a clear maximum above the surface, although the vertical and horizontal extent of the total response is similar. By comparing the dry and moist response to the control dry and moist isentropes (solid black lines in figure 2.3 and figure 2.4 respectively), we see that the response of $\overline{\theta}$ crosses the dry isentropes from the control experiment near the surface, the response of $\overline{\theta_e}$ more closely follows the control moist isentropes near the surface. This reflects the inclusion of latent heating in the formulation of θ_e. Since θ_e is approximately conserved during condensation but not during evaporation of water vapor into unsaturated air, sensible and latent fluxes in the boundary layer will lead to an increase in θ_e. By contrast, only sensible heat fluxes will act to increase θ. As the air from the surface is raised up by baroclinic eddies and adiabatically cools, it will eventually reach saturation, and latent heating will occur. Although the parcel conserves its θ_e during condensation, condensation acts as a source of θ that contributes to the flow across dry isentropes.

Since $\theta_e = \theta$ for dry air parcels, the difference $\overline{\theta_e} - \overline{\theta}$ indicates where the moisture in the lower part of the atmosphere is located. From the bottom row of figure 2.4 the majority of the water vapor response is concentrated below 800 hPa, with the total water vapor tapering off above. This indicates that the region of latent heating is mostly occurring below 800hPa. The magnitude of the MNS response of dry $\overline{\theta}$ is about half of the MNS response of moist θ_e. Although the $\phi_0 = 55°$ and $\phi_0 = 65°$ perturbation experiments do not show the same clear maximum aloft, both show the same ratio of the response of $\overline{\theta_e}$ to $\overline{\theta}$ near the surface perturbation. However the θ_e and θ responses a few degrees poleward of the surface perturbation are approximately the same for a given ϕ_0. This is because most of the air aloft has already been saturated and its water content reduced. Thus, although remote latent heating helps set the temperature of the response in the PMT, the majority of the air that is transported to the PMT has a low specific humidity. Above the boundary layer, the only significant source or sink of θ_e or θ

is radiative cooling (since diffusion is also small in this region). This is why the response of the PMT occurs at lower θ_e than in the control climatology over the perturbed region (figures 2.2 and 2.3). As warm moist air propagates poleward it is cooled radiatively and sinks to a lower level. Since this process acts on both θ_e and θ the distribution of them is approximately the same in the PMT.

The results of figures 2.3 and 2.4 suggest that a simple model of homogenization along control θ_e surfaces explains our results. As air is warmed and moistened near the surface, midlatitude weather systems act to raise up moistened air parcels to their saturation level. After this point, air parcels are able to propagate poleward through eddy mixing along θ_e surfaces. It should be noted that this interpretation is dependent on the time scale that we have chosen to look at. At 10-20 days we have chosen a time where we can study the transient impulse response to warming at the surface, but before the atmospheric circulation has a chance to adjust to a substantially changed zonal mean state. If longer time scales were considered, then the atmospheric circulation could shift relative to the initial control climate, and as a result the response might no longer follow the control run's moist isentropic surfaces, instead following the moist isentropic surfaces of the new climate.

This simple picture of moist isentropic propagation helps to explain some of the features seen in figure 2.2. The PMT response occurs higher in the troposphere in the $\phi_0 = 45°$ perturbation experiment than in the other cases because the moist isentropic surfaces that connect the MNS and PMT intersect the PMT at a higher altitude. Additionally, this also explains why the largest θ_e responses correspond to the $\phi_0 = 45°$ perturbation experiment, since this is the experiment with the largest MNS responses. The moisture responses in the PMT also show the influence of the transport pathway, since the moist response also occurs in the PMT without a surface precursor. The confinement of the moist response to lower altitude is also explained by the moist isentropic propagation mechanism. As air propagates along θ_e surfaces at high altitudes it precipitates. Although this leaves the parcels θ_e approximately unchanged, it means that air parcels that are able to ascend to a higher altitude are less moist than lower altitude parcels.

The response of the $\phi_0 = 55°$, $\delta T = 5K$ experiment is somewhat unique, in that the response has a similar magnitude in the PMT and the MNS. The response also shows a stronger response in the subtropics than the $\phi_0 = 45°$ $\delta T = 5K$ experiment. One possible explanation for this behaviour is that the stratification between the surface and the top of the boundary layer is approximately 5K in this region, so that this experiment might be subject to thresholding behaviour, the nature of which is left to future research.

We calculate the distribution of responses over the polar cap by integrating $\delta\theta_e$ over days 10-20 (shown in figure 2.3) over latitudes poleward of 75°, and then finding percentiles from the 120 member

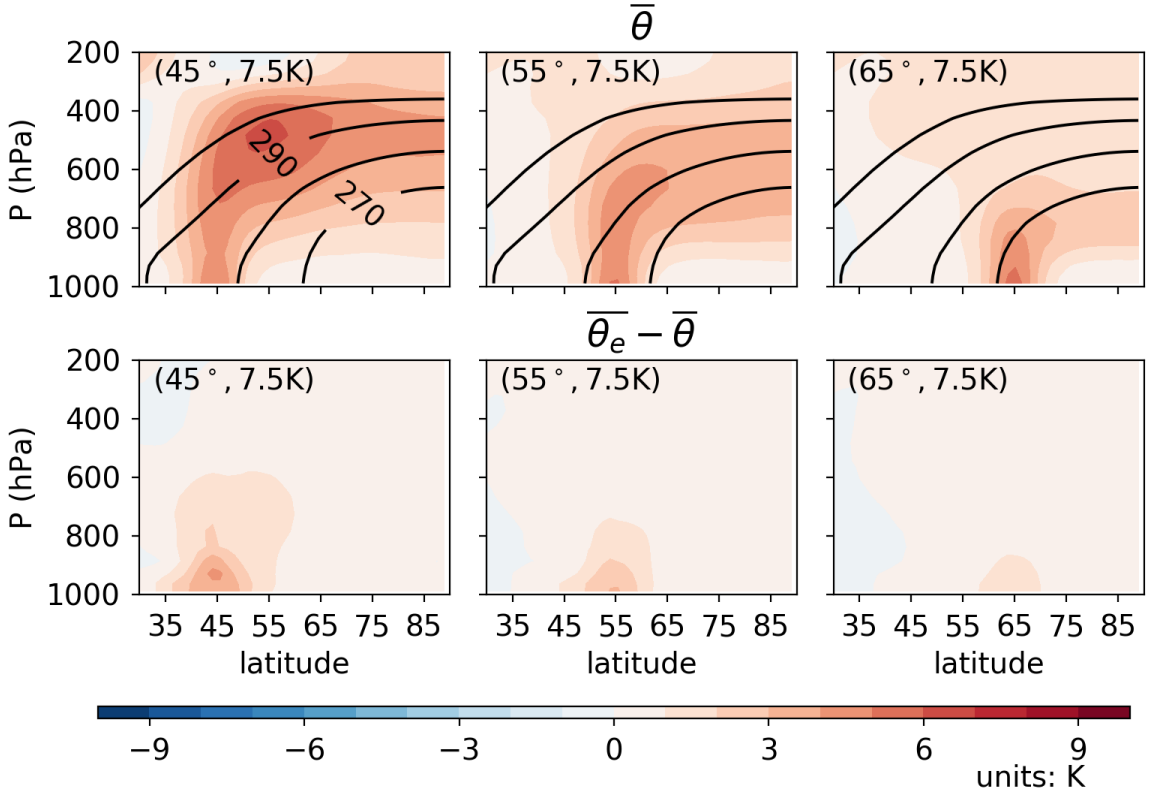

Figure 2.4: Top Row: The $\overline{\theta}$ response represented as the difference between the ensemble time mean over days 10-20 of the perturbed experiments and the control climatology (shading), and the control climatology of $\overline{\theta}$ (black contours). Contour interval is 10K starting with 270K. Bottom row: As for the top row but for the difference between the response inclusive of moisture and the response exclusive of moisture, $\overline{\theta_e} - \overline{\theta}$ (shading).

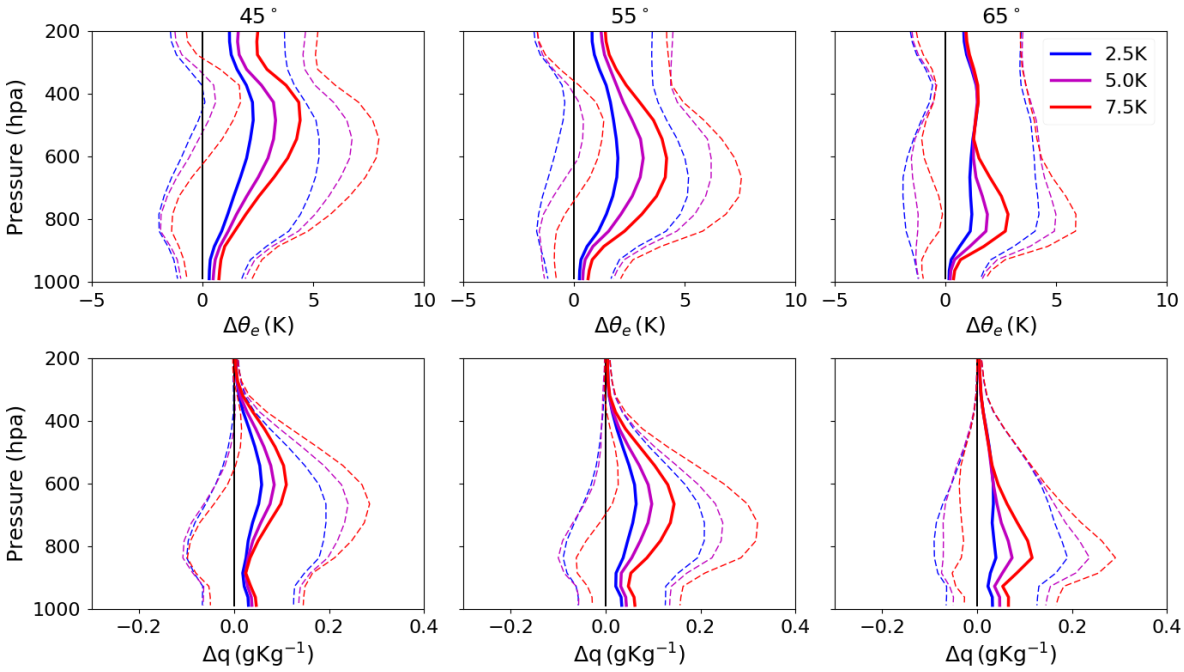

Figure 2.5: The median response (thick lines) and the 10^{th} and the 90^{th} percentiles (dotted lines) of the polar cap averages $\Delta\theta_e$ (top row) and Δq (bottom row) over days 10-20.

ensemble (figure 2.5). The 50th percentile response line shows a maximum value that is less than the applied SST perturbation δT for all of the θ_e and q responses. This is likely because of radiative cooling reducing the θ_e of air before it reaches the PMT. The heights of the maximum of the anomalies follow the patterns shown in figure 2.2; the maximum response occurs higher in the troposphere for ϕ_0 closer to the equator and the q response is at a lower altitude than the θ_e response.

The 90th and 10th percentiles follow a pattern similar to the median, so that the largest variability in the response is where the largest median response is. The distribution of the θ_e response is is wider and shifted to a higher median temperature proportional to the degree of SST perturbation.

Although the variability is quite large, the maximum 10^{th} percentile response in θ_e reaches its maximum above the line of zero response for some of the experiments, including all of the experiments perturbed at $\phi_0 = 45°$, indicating that 90% of the ensemble members show a positive response to the surface forcing. This is equivalent to a non-parametric test of the hypothesis that the response of θ_e over the polar cap is positive; where the 10^{th} percentile is greater than the zero line the null hypothesis can be rejected at the 90% level. Similar analysis in the midlatitudes shows that the results are also statistically significant over much of the midtroposphere (not shown). For the experiments perturbed at $\phi_0 = 65°$, only the $\delta T = 7.5K$ has the 10^{th} percentile close to the zero response line, and the response is much weaker.

For all of the experiments it is only a small section of the column where the 10^{th} percentile crosses the zero response line; most of the atmospheric column does not meet this test. This is in agreement with figure 2.3, which does not show a uniform response in the polar column.

The perturbations for $\delta T = 2.5K$, scaled by δT are larger than the perturbations for $\delta T = 7.5K$. In other words, the weaker SST perturbations tend to result in relatively larger amounts of heat and water vapor transport to the polar mid-troposphere per unit of SST forcing, even though the absolute anomaly is smaller and the signal weaker. Individual realizations show responses reflecting internal variability (not shown). In many realizations a cooling or drying of the PMT can occur after the surface heating is applied. If such realizations were studied in isolation, it would misleadingly suggest the opposite response to surface heating. It is only with large ensembles that we can robustly capture the response forced by the surface perturbation.

2.3.2 Response of the stratification

The latent heating of the atmosphere from the condensation of moisture is an important control on the static stability of the midlatitude atmosphere (Juckes, 2000; Frierson, 2008). The zonal mean bulk

stability is defined as

$$\Delta_{\theta_e}(p) = \overline{\theta_e(p)} - \overline{\theta_e(p_l)} \tag{2.3}$$

where p_l is the pressure at the lowest model level (approximately 983 hPa). Wherever Δ_{θ_e} is negative, an air parcel is potentially unstable to a process that would bring it from the surface to that level, assuming that there is a force to lift the air mass to its saturation level (see Emanuel, 1994, section 6.7). In the extratropics of the IMM, cyclonic systems supply this initial lifting (e.g. Schemm et al., 2013). A positive Δ_{θ_e} shows how much the θ_e of the parcel needs to be increased at the value of p_l before it is able to become potentially unstable. We will also make use of the analogous dry bulk stability, Δ_θ.

The distributions of Δ_{θ_e} for the $\delta T = 7.5$K experiments are shown in figure 2.6 (top row). All experiments show a decrease in Δ_{θ_e} over the SST perturbation and an increase in Δ_{θ_e} above and poleward of the perturbation. This is consistent with the transport pathway that was identified in figure 2.3. Since the MNS SST perturbation increases θ_e at the surface, Δ_{θ_e} is decreased above the surface perturbation. As the warmed air is raised and moves poleward of the perturbation, it increases the stability of the atmosphere because there is no corresponding increase in θ_e at the surface polewards of the perturbation. Thus the surface perturbation acts to increase the stability in the PMT while it is warming it.

In the $\phi_0 = 45°$ experiment, the changes in the bulk stratification are important, since the decrease in bulk stability occurs in a region where the bulk stability in the control experiment is near neutral. The perturbed distribution of Δ_{θ_e} shows that air is potentially unstable up to 600 hPa, and $\Delta_{\theta_e} \approx 10$K at 400 hPa; above this point the stratification increases rapidly. Note that since the stratification is based on zonal and ensemble averages, individual air parcels can exceed the stratification, which is why the response is able to extend to 400hPa and not be trapped at 600 hPa. In the $\phi_0 = 55°$ and $\phi_0 = 65°$ experiments, the $\Delta_{\theta_e} = 0$ line only extends to approximately 600 and 850 hPa respectively and the surface perturbations are not strong enough to overcome the stratification and so the θ_e responses are trapped lower in the troposphere. In these experiments the surface perturbation is not able to mix as high into the troposphere since the perturbations were placed in more stably stratified regions to begin with.

The change in stratification in the PMT is larger for the $\phi_0 = 45°$ perturbation than for either the $\phi_0 = 55°$ or $\phi_0 = 65°$ perturbation experiments. This reflects control by lower tropospheric stratification at the latitude of the perturbation. If Δ_{θ_e} above the SST perturbation is perturbed but remains positive, then there will not be a large change in the free troposphere, since the troposphere will remain stably stratified on average. The surface response will remain trapped in the lower troposphere above the

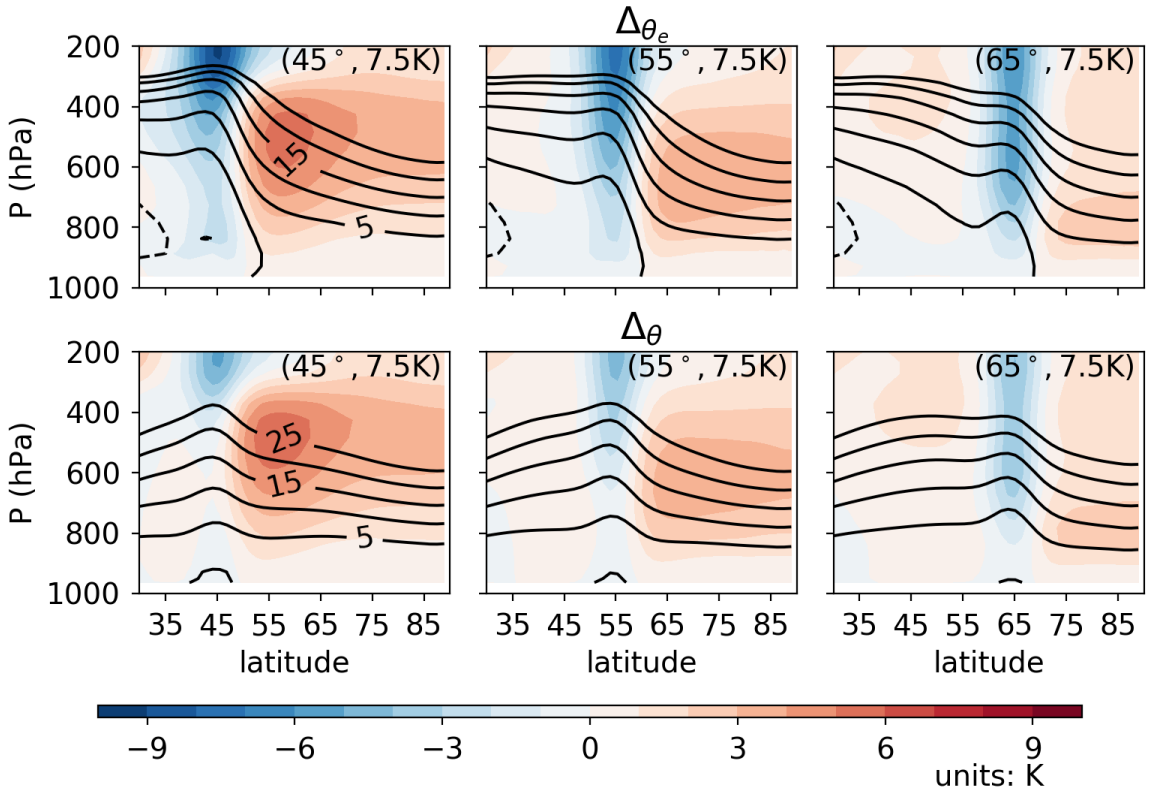

Figure 2.6: Top row: the total ensemble and time mean Δ_{θ_e} over days 10-20 from the perturbed runs (black contours), and the difference from the control climatology (shaded). The contour level is 5K and the contours extend from -5K to 25K, with negative contours dashed. Bottom row: as for the top row, but for dry Δ_θ.

perturbation and not be advected towards the PMT in this case. Alternatively, if there is a change in Δ_{θ_e} which lowers it below zero, then the atmosphere will become potentially unstable, and further increases in surface θ_e will be transmitted to the midtroposphere relatively easily. Since, in the control climatology, the region around $\phi_0 = 45°$ is weakly unstably stratified then even relatively small perturbations in this region will have a large impact. For the $\phi_0 = 65°$ experiments, the atmosphere is strongly stratified, so even for the $\delta T = 7.5$K the surface perturbations remain trapped in the lower troposphere. For the $\phi_0 = 55°$ experiments the atmosphere is close to neutral stratification, and suggests threshold behavior; although the $\delta T = 7.5$K perturbation is able to overcome the surface stratification, the weaker perturbations leave the stratification close to neutral. We hypothesize that this is why the $\phi_0 = 55°$ experiments show a stronger dependence on the size of δT than the other experiments.

Although the distribution of θ shows a decrease in stratification near the surface (bottom row of figure 2.6), nowhere except very close to the surface does the average atmosphere become neutrally stable with respect to dry adiabatic perturbations ($\Delta_\theta \approx 0$). The increase in Δ_θ is approximately the same as $\Delta\theta_e$ poleward of the surface perturbation. This is consistent with the difference between the response of $\overline{\theta_e}$ and $\overline{\theta}$.

The response of the stratification considering only the dry θ is somewhat paradoxical, particularly for the 45 ° experiment. By heating the surface, we have increased the stratification aloft; at odds of what might be normally expected when heating a stratified fluid from below. This paradox is once again resolved by thinking about how latent heating introduces a heating in θ aloft; creating a vertical offset in the response of θ. Mechanical forcing is able to raise air to its condensation level, which increases θ at this level. As this air propagates poleward from the source region of θ, it increases the bulk stratification there.

2.3.3 Response of the eddy heat flux

The eddy covariances $\overline{v'\theta'_e}$ and $\overline{v'\theta'}$, which represent the eddy meridional flux of θ_e and θ, also show a response to midlatitude SST perturbations. The control $\overline{v'\theta'_e}$ shows a strong maximum near the surface that is approximately double that of $\overline{v'\theta'}$ (figure 2.7 top row). The response can be quite large: the maximum of the $\overline{v'\theta'_e}$ response for the $\delta T = 7.5$K, $\phi_0 = 45°$ perturbation experiment is approximately 35% the maximum of $\overline{v'\theta'_e}$ in the control climatology. The eddy covariances are increased poleward of the SST perturbation, and decrease equatorward of the SST perturbation. This results in a poleward shift of the maximum eddy flux in the 45° and 55° perturbation experiments. In the 65° perturbation experiment the response of $\overline{v'\theta'_e}$ are too small and far away from the maximum in the eddy flux to

shift it. These changes are consistent with the changes in surface baroclinicity introduced by the SST perturbations. Generally, equatorward of the SST perturbation the surface baroclinicty is decreased, and poleward of the SST perturbation the surface baroclinicity is increased. These results are consistent to the results of Brayshaw et al. (2008) and Michel and Rivière (2014) who see an increase in the strength of the kinetic energy of the storm tracks and a shift in the zone of baroclinic eddies with increased SST gradients.

The responses of the eddy covariance in the $\phi_0 = 45°$ experiment extend from the surface to the upper troposphere. In the $\phi_0 = 55°$ and $\phi_0 = 65°$ experiments the responses of $\overline{v'\theta'_e}$ and $\overline{v'\theta'}$ remain closer to the surface. This is likely because the eddies are unable to overcome the strong stratification in these latitudes and so cannot raise the same amount of warm moist air to the mid-troposphere. This means that the coupling between the eddies and the response in θ_e will be smaller, and so the response of $\overline{v'\theta'_e}$ will be smaller.

The response in $\overline{v'\theta'_e}$ has its strongest amplitude closer to the surface than $\overline{v'\theta'}$ and its peak amplitude is about double that of $\overline{v'\theta'}$. The doubling in both the mean and the response reflects the approximately equal contributions of sensible and latent heat fluxes in large-scale midlatiutde eddies (Peixoto and Oort, 1992; Pauluis et al., 2008; Shaw and Pauluis, 2012; Wu and Pauluis, 2013). The relatively higher altitude response in the dry eddy heat flux reflects the role of condensation as a source of θ.

2.4 Response of the circulation in θ_e coordinates

Streamfunctions in conserved thermodynamic coordinates allow for the zonal mean mass transport by eddies to be quantified. To further explore the response, we compute streamfunctions with a θ_e vertical coordinate using the Statistical Transformed Eulerian Mean (STEM) method (Pauluis et al., 2011). This method separates the mean and eddy circulations, and so provides new diagnostic information that would be difficult to determine using the direct isentropic circulation method of Pauluis et al. (2010).

The STEM streamfunction uses a second order statistical closure to calculate the mass fluxes on θ_e surfaces and is summarized by:

$$\psi(\overline{\theta_e}, \overline{\theta_e'^2}, \overline{v}, \overline{v'\theta'_e}) = \psi_M(\overline{\theta_e}, \overline{\theta_e'^2}, \overline{v}) + \psi_E(\overline{\theta_e}, \overline{\theta_e'^2}, \overline{v'\theta'_e}), \tag{2.4}$$

where ψ, ψ_M, ψ_E are the total, mean and eddy streamfunction in θ_e coordinates, and $\overline{\theta_e}, \overline{\theta_e'^2}, \overline{v}, \overline{v'\theta'_e}$ are the zonal mean distribution of θ_e, the zonal variance of θ_e, the zonal mean meridional velocity, and the eddy covariance of θ_e. The zonal mean statistics in equation (2.4) are computed on pressure surfaces.

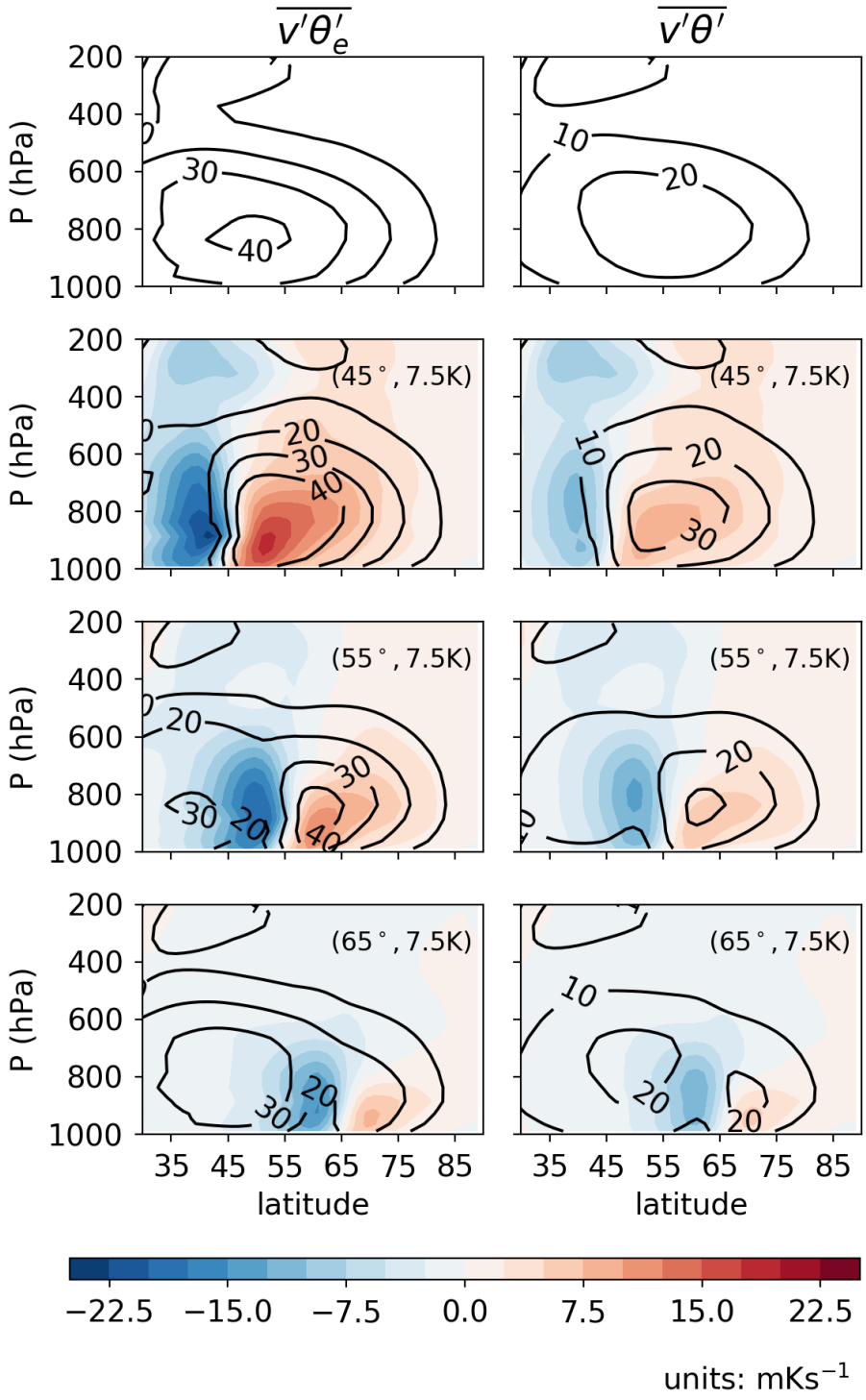

Figure 2.7: Top row: the distribution of $\overline{v'\theta'_e}$ and $\overline{v'\theta'}$ in the control climatology. Bottom rows: the perturbed distribution (contours) and difference from the control climatology (filled contours) of $\overline{v'\theta'_e}$ and $\overline{v'\theta'}$ for the 7.5K experiments. The contour interval is 10ms^{-1}K

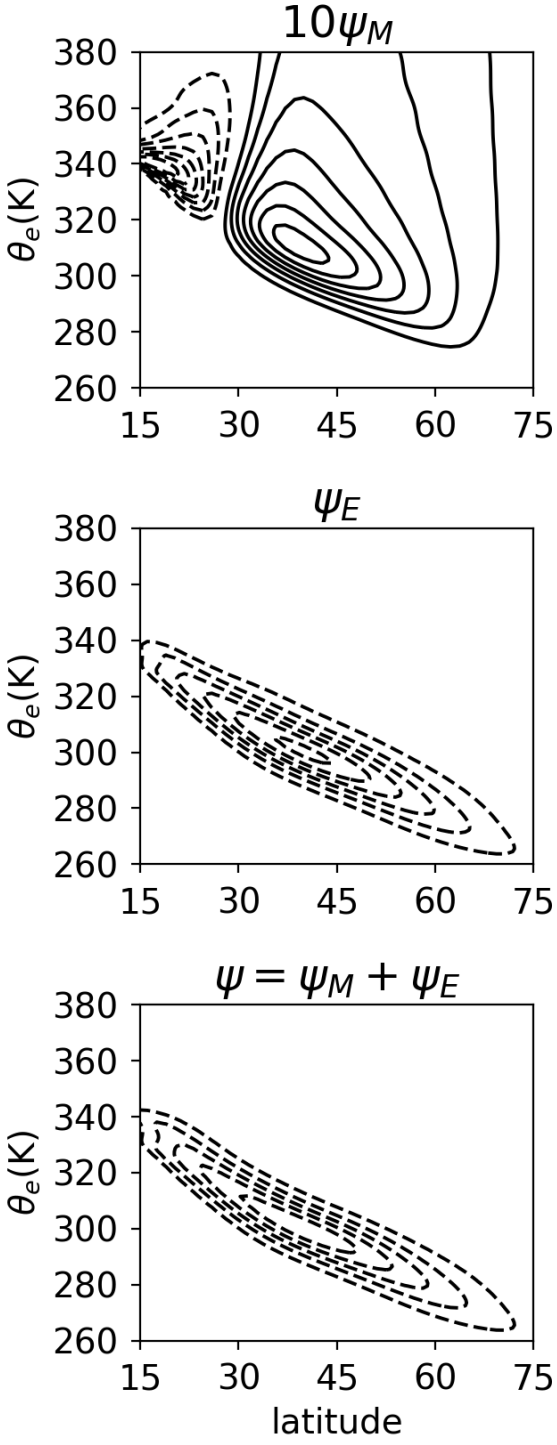

Figure 2.8: The mean (top panel), eddy (middle panel) and total (bottom panel) STEM streamfunctions in θ_e coordinates. Note that ψ_M has been multiplied by a factor of 10 to be comparable to ψ_E. The contours extend from -3.5 to 3.5 $\times 10^{11}\mathrm{kg\,s^{-1}}$ with a 0.5 $\times 10^{11}\mathrm{kg\,s^{-1}}$ contour interval, and the zero contour is not shown.

Further details are given in subsection 1.2.4. ψ_M is independent of $\overline{v'\theta'_e}$, and ψ_E is independent of $\overline{v}$.

Figure 2.8 shows the control simulation's ψ_M, ψ_E, and the total streamfunction, $\psi_M + \psi_E$ calculated using the STEM method. The total streamfunction shows a single overturning cell transporting high θ_e air polewards and low θ_e air equatorwards. ψ_M shows the familiar thermally direct Hadley cell in the tropics and the thermally indirect Ferrel cell in the midlatitudes. We note that ψ_M is closed at statospheric θ_e values, but that the circulation required to close the streamfunction is weak compared to the tropospheric circulation ψ_E dominates over ψ_M, except in the deep tropics where the Hadley cell is an important influence. The shape and range of the cell as well as the partitioning between the mean and eddy components is in qualitative agreement with results from observations shown in Pauluis et al. (2011); however the partitioning is weighted more strongly towards the eddy component in the IMM. This is consistent with the unrealistically strong SST gradients and lower tropospheric baroclinicity in the simulation (figure 2.1). The response in ψ_E (figure 2.9) can be divided into a decrease in the streamfunction at near-surface values of θ_e (the grey line in figure 2.9) near the latitude of the SST perturbation and an increase in the streamfunction poleward of the SST at higher θ_e values. The response near the latitude of the SST perturbation represents an increase in the θ_e of equatorward moving air near the surface. The high latitude responses show an increase in the θ_e of poleward moving air in the mid- and upper-troposphere. These represent upward shifts in the entire streamfunction, although not of equal magnitude. This upwards shift will be further explored by decomposing the streamfunction.

As in section 2.3, perturbations centered at $\phi_0 = 45°$ have a relatively larger impact on ψ_E than the perturbations at either $\phi_0 = 55°$ or $\phi_0 = 65°$. The responses scale approximately linearly with δT.

These streamfunction responses can also be used to calculate the response in total atmospheric enthalpy (heat) transport. Since the mass transport on an isentrope is $-\partial\psi/\partial\theta_e$, the total eddy poleward heat transport (PHT) through a given latitude can be computed as

$$H_E = -C_p \int_0^\infty \theta_e \left[-\frac{\partial \psi_E}{\partial \theta_e} \right] d\theta_e, \tag{2.5}$$

where C_p is the specific heat capacity at constant pressure.

The response in the PHT (figure 2.10) shows a decrease on the equatorward side of the SST perturbation and an increase on the poleward side, which is consistent with the response in baroclinicity and local eddy covariance (figures 2.3 and 2.7). Since the decrease on the equatorward side of the surface forcing latitude ϕ_0 is stronger than the increase on the poleward side, the net result is a reduced PHT, even though the midlatitude forcing increases heat transport into the PMT.

Again, the largest respones are seen for the perturbation at 45°. This is consistent with the largest

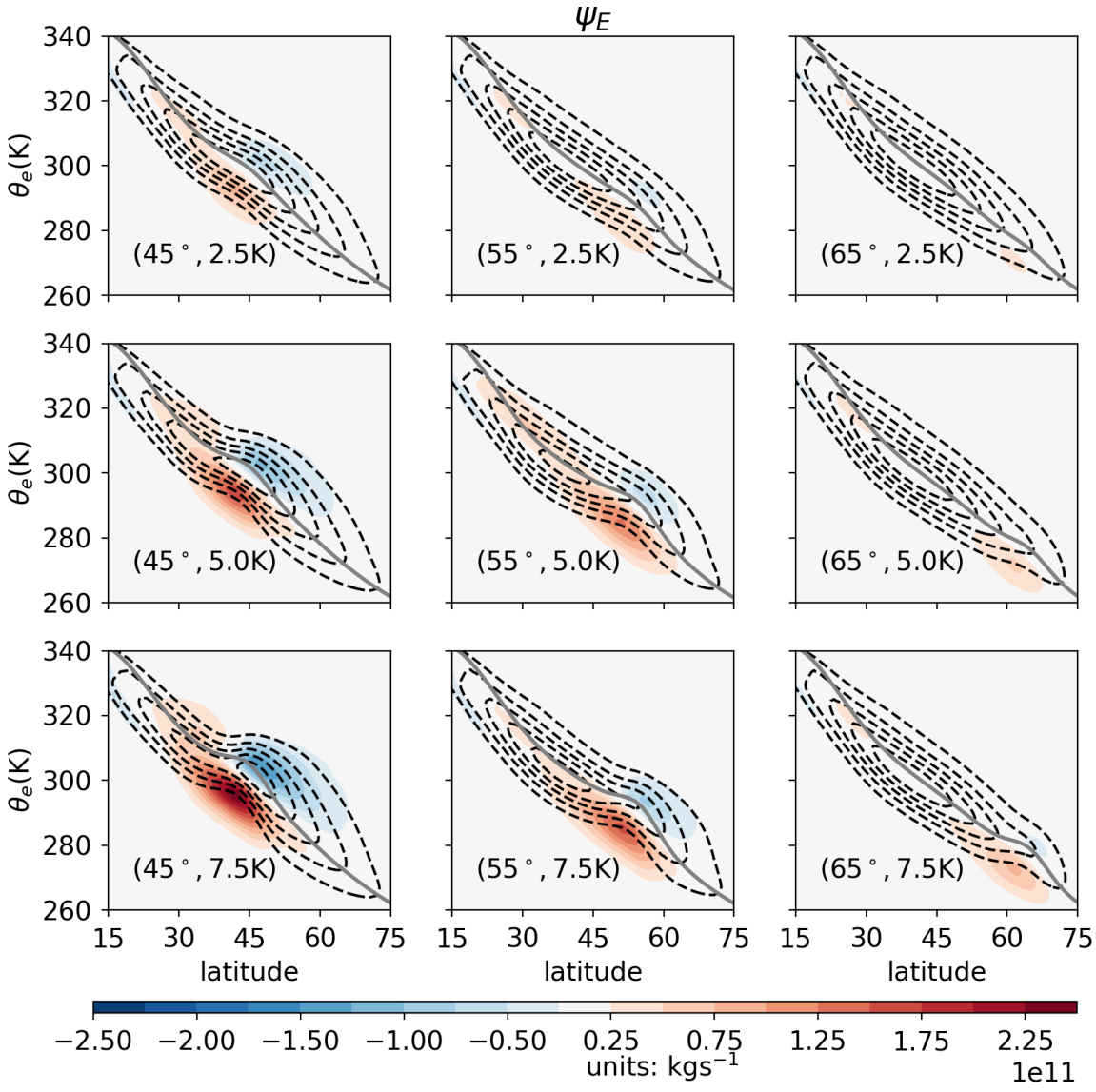

Figure 2.9: The ensemble averaged ψ_E from the perturbed experiments averaged over days 10-20 (dashed contours) and the difference between the perturbed and control streamfunction (filled contours). The dashed contours extend from -0.5 $\times 10^{11}$kg s^{-1} to -3.5 $\times 10^{11}$kg s^{-1} with 0.5 $\times 10^{11}$kg s^{-1} contour interval. The solid grey line is mean θ_e at the model level nearest to the surface.

responses in $\overline{v'\theta'_e}$ being centered here, and suggests that the circulation is more sensitive in regions where it already has the lowest stability. For all experiments, the responses scale approximately linearly per degree of SST perturbation (not shown).

We can further separate the contribution from perturbations in these streamfunctions to perturbations in the input quantities, by using the method of Wu and Pauluis (2013). Denoting the control variables by $(\overline{\theta_e}^c, \overline{\theta'^2_e}^c, \overline{v'\theta'_e}^c)$, and perturbation variables by $(\overline{\theta_e}^p, \overline{\theta'^2_e}^p, \overline{v'\theta'_e}^p)$, we define the perturbations of ψ_E due to $\overline{\theta_e}^p$ by

$$\delta_{\overline{\theta_e}}\psi_E \equiv \psi_E(\overline{\theta_e}^p, \overline{\theta'^2_e}^c, \overline{v'\theta'_e}^c) - \psi_E(\overline{\theta_e}^c, \overline{\theta'^2_e}^c, \overline{v'\theta'_e}^c), \tag{2.6}$$

and similarly for $\delta_{\overline{\theta'^2_e}}\psi_E$ and $\delta_{\overline{v'\theta'_e}}\psi_E$. Then the total perturbation can be written as

$$\delta\psi_E = \psi_E(\overline{\theta_e}^p, \overline{\theta'^2_e}^p, \overline{v'\theta'_e}^p) - \psi_E(\overline{\theta_e}^c, \overline{\theta'^2_e}^c, \overline{v'\theta'_e}^c) = \delta_{\overline{\theta_e}}\psi_E + \delta_{\overline{\theta'^2_e}}\psi_E + \delta_{\overline{v'\theta'_e}}\psi_E + R_\psi, \tag{2.7}$$

where R_ψ is a residual for this calculation. This decomposition amounts to assuming that the perturbations are approximately linear, or that the residual is small. We have verified that the size of R is sufficiently small for the technique to be justified (not shown).

Here we apply (2.7) to the $\phi_0 = 45°, \delta T = 7.5$K experiment (left column of figure 2.11); the other experiments have similar results. Comparing $\delta_{\overline{\theta_e}}\psi_E$ and $\delta_{\overline{v'\theta'_e}}\psi_E$ we see that changing θ_e has a very different impact from changing $\overline{v'\theta'_e}$. The $\delta_{\overline{\theta_e}}\psi_E$ term shows an upward shift in the streamfunction - the streamfunction is decreased at lower values and then increased at higher values of $\overline{\theta_e}$. This shift occurs at the same latitude as the SST perturbation and the responses are isolated to within a small range of that latitude. This change can be interpreted as an increase in the θ_e of poleward moving parcels and as an increase in the θ_e of equatorward moving parcels near the latitude of the SST perturbation. This contrasts with the $\delta_{\overline{v'\theta'_e}}\psi_E$ term which shows a change in the poleward mass transport. The transport is decreased on the equatorward side of the SST perturbation and increased on the poleward side of the SST perturbation. Small remote responses can also be seen in the Tropics, although this is unimportant for the analysis here. This term shows that the perturbed circulation is increased on the poleward side of the SST perturbation and reduced on the equatorward side of the SST perturbation. The total streamfunction response shows the combination of these two effects. The upward shift in the streamfunction is primarily a result of the change in $\overline{\theta_e}$, while the increase in the streamfunction poleward of the SST perturbation is due to the change in $\overline{v'\theta'_e}$.

The difference in these terms can be interpreted in terms of the impact of the SST perturbation on the atmospheric statistics. By perturbing the SST, $\overline{\theta_e}$ is raised immediately over the perturbation

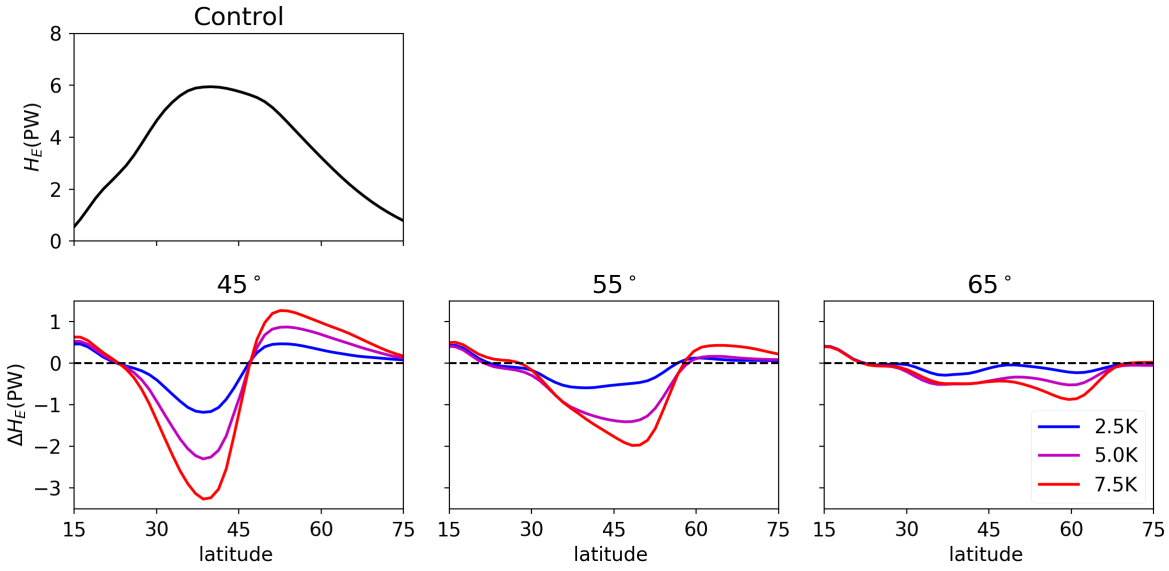

Figure 2.10: The response of the total eddy heat flux H_E calculated using equation (2.5). The lines correspond to: red, $\delta T = 7.5$K; magenta, $\delta T = 5.0$K, and blue, $\delta T = 2.5$K

.

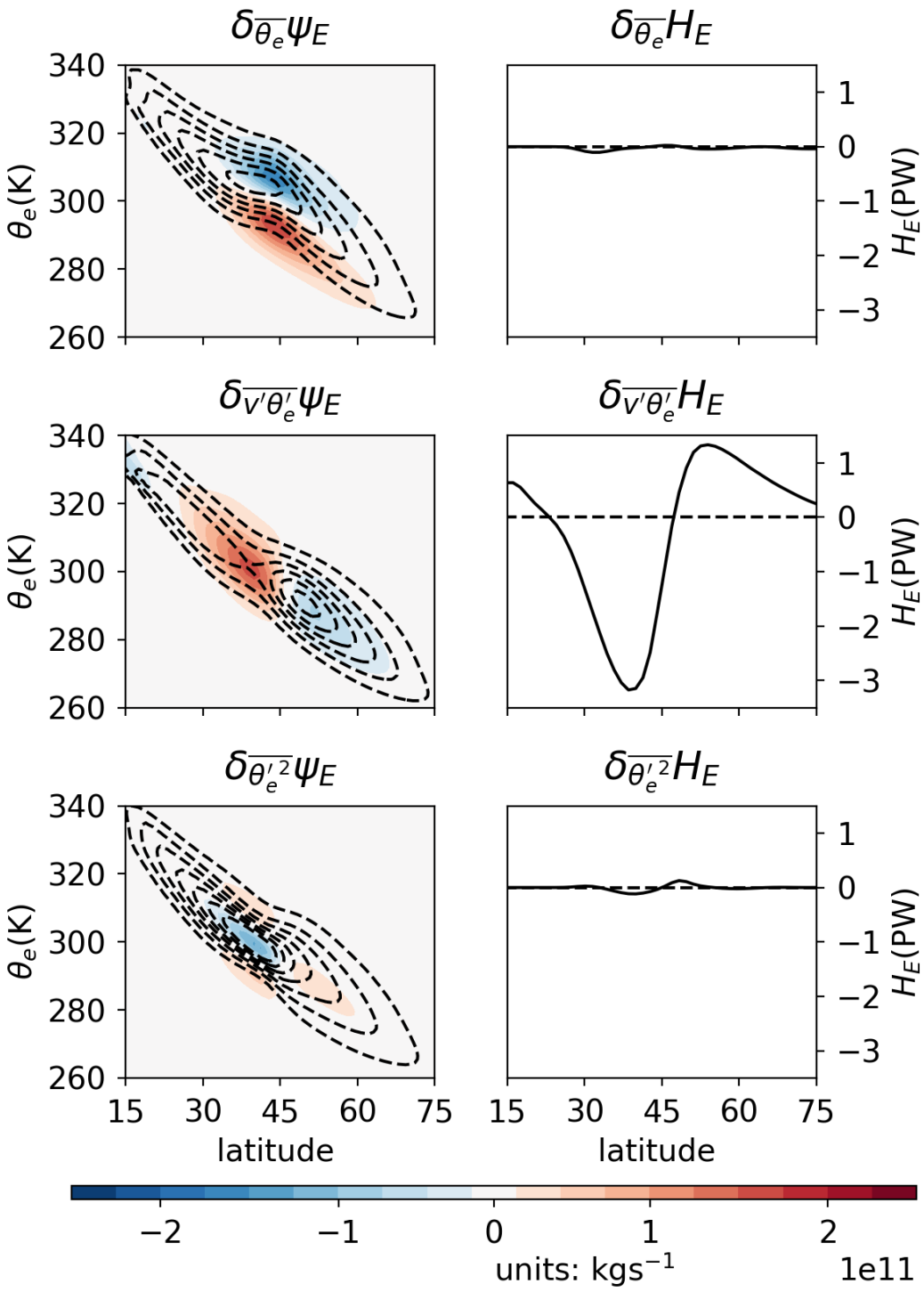

Figure 2.11: Left column: the difference in the ensemble mean ψ_E averaged over days 10-20 of the $\delta T = 7.5$K, $\phi_0 = 45°$ perturbation experiment, decomposed according to equation (2.7) (shading) and the sum of the difference and the control climatology (contours), e.g. the top column is $\psi_E(\overline{\theta_e}^p, \overline{\theta_e'^2}^c, \overline{v'\theta_e'}^c)$ (dashed contours, intervals as for figure 2.9). Right column: the corresponding total atmospheric eddy heatflux responses δH_E.

by warming and moistening through a vertical heat flux. It also increases the $\overline{\theta_e}$ in the mid- and upper-troposphere by decreasing the static stability, which further encourages vertical motion. This has the effect of raising $\overline{\theta_e}$ by similar amounts in both the equatorward flow near the surface as well as the poleward flow in the mid- and upper-troposphere. There is also a poleward shift of the maximum circulation, consistent with the responses in eddy covariance (figure 2.7).

These results are consistent with Wu and Pauluis (2013), who showed that the responses in the eddy covariance to CO_2 doubling have a large impact on the eddy component of the moist isentropic circulation. Although their experiment is quite different, the decomposition of responses in the eddy streamfunction to $\delta_{\overline{\theta_e}}\psi_E$ and $\delta_{\overline{v'\theta'_e}}\psi_E$ show that responses in $\overline{\theta_e}$ result in an upward shift of the moist isentropic circulation and that responses in $\overline{v'\theta'_e}$ result in a change in the strength of the circulation. In our experiment, reflecting differences in forcing and model, the responses in $\overline{v'\theta_e}$ are relatively larger than in their study.

The same decomposition technique can be used to separate the PHT response. Equations (2.5) and (2.7) can be combined:

$$\delta H_E = \delta_{\overline{\theta_e}} H_E + \delta_{\overline{\theta'^2_e}} H_E + \delta_{\overline{v'\theta'_e}} H_E + R_H. \tag{2.8}$$

where R_H is the residual for this calculation. Using equation (2.8), the different impacts of changes in $\overline{\theta_e}$ and $\overline{v'\theta'_e}$ can also be seen on the heat flux (right column of figure 2.11). Most of the heat flux response comes from $\delta_{\overline{v'\theta'_e}} H_E$, while $\delta_{\overline{\theta_e}} H_E$ contributes very little to the total heatflux response.

The shift from $\delta_{\overline{\theta_e}}\psi_E$ to higher $\overline{\theta_e}$ leads to an increase in the θ_e in the poleward moving airmass, but also to a compensatory increase in the equatorward moving airmass. A similar observation can be made of $\delta_{\overline{\theta'^2_e}}\psi_E$. As the circulation contracts onto a smaller range of isentropes there is a cancellation between the increase of the circulation on the mid isentropes and the decrease in circulation on the upper and lower isentropes.

In contrast, the anomaly $\delta_{\overline{v'\theta'_e}}\psi_E$ shows an increase in the circulation at higher latitudes and a decrease in circulation at lower latitudes. This results in an increased heat flux at higher latitudes since high θ_e air is being moved to higher latitudes and the low θ_e air is being removed with no cancellation. The only way for a cancellation effect in the $\delta_{\overline{v'\theta'_e}}\psi_E$ term at a given latitude would be to have the $\overline{v'\theta'_e}$ response change sign with altitude, and this was not observed in any of our experiments.

2.5 Conclusions

The main conclusions of this study can be summarized as follows:

1. In an idealized moist model, midlatitude surface temperature perturbations create surface temperature and moisture responses that are transported to the polar midtroposphere approximately along moist isentropic surfaces from the control climate. The time scale of the response is 10-20 days.

2. Perturbations near regions where the stratification is weak in the control experiment show the largest impacts on the polar midtroposphere and on the stratification over the polar cap.

3. The moist response is located near to the surface and can be used to understand the cross isentropic motion and distribution of stability changes in the extratropical atmosphere.

4. The surface perturbations result in an increase of the local eddy heat flux poleward of the surface perturbation and a decrease equatorward of the surface perturbation.

5. The moist isentropic eddy circulation deforms around the surface temperature perturbation, with responses in both the equatorward surface flow and the poleward flow aloft.

6. The response in moist isentropic eddy circulation can be decomposed into a upward shift onto warmer isentropes related to a response in the zonal mean distribution of isentropes $\overline{\theta_e}$, a poleward intensification of the circulation related to a response in the eddy covariance, $\overline{v'\theta'_e}$, and a reduction of the range of isentropes related to a response in the zonal variability of isentropes, $\overline{\theta'^2_e}$

7. The total poleward enthalpy transport is more sensitive to a change in the eddy covariance than it is to changes in the distribution of the zonal mean or zonal variance of isentropic surfaces.

The approach taken in this study was deliberately simple, using zonally symmetric control and perturbation boundary conditions and thus exploiting zonal symmetry in the statistics. However zonal variations in the control and the perturbations will need to be taken into account in order to understand the practical relevance of this analysis, including the impact of stationary waves on how moist isentropic transport operates in a regional context. For instance, Kaspi and Schneider (2013) showed that zonal asymmetric boundary conditions in the IMM can increase the poleward energy flux. Additionally, the idealized nature of the model used here precludes a further investigation of the impact of $\overline{\theta_e}$ anomalies in the AMT on Arctic surface conditions. Water vapor and lapse rate feedbacks have been shown to have an important role in Arctic amplification (Pithan and Mauritsen, 2014), and observational studies show

that large moisture transport events into the Arctic can create downward longwave radiative heating at the surface (Woods and Caballero, 2016). However, a detailed investigation of these mechanisms would require a more realistic radiative transfer scheme that allows for the radiative impacts of water vapor. Another interesting direction of future research would be to examine the moist isentropic propagation mechanism in a dry model, or with the moisture scaling of Frierson et al. (2006) to further examine the role of latent heating in the connection. Although Laliberté and Kushner (2014) demonstrated a linkage between the MNS and the AMT on intraseasonal time scales during boreal summer, it is unclear how this linkage operates in boreal winter, or how the seasonal cycle impacts the transport between the two regions. All of these impacts and effects could be explored as we move up the climate modeling hierarchy towards the realism of a comprehensive atmospheric general circulation model.

Chapter 3

The Sensitivity of the Statistical Transformed Eulerian Mean Circulation to Climate Perturbations

3.1 Introduction

The statistical transformed Eulerian Mean (STEM) framework (Pauluis et al., 2011) provides a powerful tool for analyzing the global circulation. Recall that the STEM, introduced in Chapter 1, allows calculation of the circulation in θ_e coordinates using first and second order eddy statistics calculated in pressure coordinates. Its form allows a straightforward numerical procedure, which we used in Chapter 2, to gain additional insight into the response to midlatitude thermal perturbations. The technique we used was originally developed by Wu and Pauluis (2013), who linearized perturbations to the STEM around a control simulation by perturbing the input variables to the STEM one at a time. In this Chapter, we develop a perturbation theory that justifies this numerical approach and that provides additional insight into controls on the overturning circulation embodied within the STEM.

To begin with, we briefly review the numerical linearization procedure of the STEM and some of the past studies that have used it. Denoting variables in a control state by ($\overline{v}^c$, $\overline{\theta_e}^c$, $\overline{\theta_e'^2}^c$, $\overline{v'\theta_e'}^c$), and perturbation variables by ($\overline{v}^p$, $\overline{\theta_e}^p$, $\overline{\theta_e'^2}^p$, $\overline{v'\theta_e'}^p$), we define the perturbations of ψ due to a perturbation of

$\overline{\theta_e}$ by

$$\delta_{\overline{\theta_e}}\psi \equiv \psi(\overline{v}^c, \overline{\theta_e}^p, \overline{\theta_e'^2}^c, \overline{v'\theta_e'}^c) - \psi(\overline{v}^c, \overline{\theta_e}^c, \overline{\theta_e'^2}^c, \overline{v'\theta_e'}^c), \tag{3.1}$$

and similarly for perturbations to the other control variables $\overline{v}$, $\overline{\theta_e'^2}$, and $\overline{v'\theta_e'}$, resulting in analogous expressions for $\delta_{\overline{v}}\psi$, $\delta_{\overline{\theta_e'^2}}\psi$ and $\delta_{\overline{v'\theta_e'}}\psi$. Then the total perturbation can then be written as

$$\delta\psi = \psi(\overline{v}^p, \overline{\theta_e}^p, \overline{\theta_e'^2}^p, \overline{v'\theta_e'}^p) - \psi(\overline{v}^c, \overline{\theta_e}^c, \overline{\theta_e'^2}^c, \overline{v'\theta_e'}^c) = \delta_{\overline{v}}\psi + \delta_{\overline{\theta_e}}\psi + \delta_{\overline{\theta_e'^2}}\psi + \delta_{\overline{v'\theta_e'}}\psi + R_\psi, \tag{3.2}$$

where R_ψ is a residual for this calculation. If we assume that the difference between the control and perturbed variable scales as a constant parameter, ϵ, which is the same for all of the control parameters, then R_ψ is second order in ϵ. Additionally, we can obtain a second level of decomposition if we separate $\delta\psi$ into mean and eddy components.

This decomposition has been used in several previous studies, with different GCMs. to analyze the responses to a variety of climate perturbations. In the original application, Wu and Pauluis (2013) used a slab ocean model coupled to a comprehensive atmospheric GCM (the Community Atmospheric Model 3) to analyze the circulation response to doubling of CO_2. Their study used a preindustrial, "1xCO_2" experiment as *control*, and a "2xCO_2" experiment as a perturbed state. They found: 1) a relatively large upwards shift in $\psi(\phi, \theta_e)$ towards greater (warmer) values of $\overline{\theta_e}$, which is largely due to the change in $\delta_{\overline{\theta_e}}\psi$; 2) and a relatively small intensification of ψ in the tropics largely attributable to $\delta_{\overline{v}}\psi$ and 3) an intensification in the midlatitude circulation attributable to $\delta_{\overline{v'\theta_e'}}\psi$. In the context of these experiments, the linearization technique is useful for separating the relatively small dynamical changes (i.e. the response in ψ to changes in $\overline{v}$ and $\overline{v'\theta_e'}$) from the relatively large thermodynamical changes (i.e. to changes in $\overline{\theta_e}$).

In a paleoclimatic application, Mantsis et al. (2014) used a coupled ocean atmospheric model (the Geophysical Fluid Dynamics Laboratory Climate Model, version 2.1) with two different obliquities to study differences in the circulation and heat transport. Similarly to Wu and Pauluis (2013), they find that $\delta_{\overline{\theta_e}}\psi_E$ is responsible for an upward shift in the Northern Hemisphere circulation on θ_e surfaces, but does not change the strength of the circulation. By contrast $\delta_{\overline{v'\theta_e'}}\psi_E$ is responsible for changing the intensity of the circulation in the midlatitudes.

In Chapter 2, which was published as Fajber et al. (2018), this decomposition is applied to an idealized moist model, and localized midlatitude surface warming are used as a perturbation. The decomposition revealed large, localized increases in $\delta_{\overline{\theta_e}}\psi_E$ in the vicinity of the warming, $\delta_{\overline{v'\theta_e'}}\psi_E$ results in a poleward

shift of the maximum of $\psi_E(\phi, \theta_e)$, and $\delta_{\overline{\theta_e'^2}}\psi_E$ results in a widening of $\psi_E(\phi, \theta_e)$.

Finally, in work in preparation, Audette et al. (in prep.) are analyzing a suite of GCMs that are participating in the prescribed ocean and sea-ice GCM contributions to the polar amplification model intercomparison project (PAMIP, Smith et al., 2019). In this case, the control variables are drawn from a GCM simulation using present-day sea surface temperatures (SSTs) and sea ice, and the perturbation experiments represent the separate driving from either future SST increases in the tropics and midlatitudes or from Arctic SST increases and sea ice loss, both resulting from projected greenhouse warming diagnosed from future climate simulations. For the SST warming experiments, $\delta_{\overline{\theta_e}}$ is large, and the cell shifts to higher θ_e values globally. When Arctic forcing is applied, $\delta_{\overline{\theta_e}}\psi_E$ is positive in the Arctic, while $\delta_{\overline{v'\theta_e'}}\psi_E$ is negative in the Arctic. These two effects cancel in the upper branch of $\psi_E(\phi, \theta_e)$, but in the lower branch there is an increase in θ_e, which causes an overall reduction in heat transport. Thus, in this case, the STEM numerical linearization technique elucidates the compensating effects that can arise in the projected response of the circulation to climate change, which have been identified in other studies of the response of the circulation to sea ice loss (Oudar et al., 2017; Blackport and Kushner, 2017; McCusker et al., 2017).

Despite the diversity of models and forcings considered, these studies reviewed here reveal consistent changes associated with each of the STEM variables: changes in $\overline{v}$ change the mean circulation, changes in $\overline{v'\theta_e'}$ change the strength of the eddy circulation, changes in $\overline{\theta_e}$ change the location of the circulation in the θ_e coordinate, and changes in $\overline{\theta_e'^2}$ change the width of the streamfunction. These similarities prompts us to study how these responses might be anticipated from the mathematical structure of the STEM. In this Chapter we seek to explain these previous numerical results by analyzing the STEM parametrization in more depth.

In Section 3.2 we review the STEM circulation and show how a change of variables simplifies the interpretation of the STEM. In Section 3.3 we calculate the functional derivatives of the STEM, which quantify how perturbations in the STEM variables, calculated in pressure space, project onto thermodynamic coordinates. By analyzing these functional derivatives we show how the features common to the previous studies are related to the mathematical structure of the STEM. In Section 3.4 we illustrate a "toy model" application in which we divide the troposphere into two layers, to further elucidate the STEM circulation and the functional derivatives. In Section 3.5 these results are applied to realistic GCM experiments of climate change to evaluate the observed changes. In Section 3.6 we briefly summarize the results of the previous Sections and discuss some future research directions.

Throughout this Chapter we will use the STEM with equivalent potential temperature θ_e coordinates, unless otherwise specified. The results, however, apply to other thermodynamic coordinate choices.

3.2 Expressions for the STEM

The STEM parametrizes the moist isentropic circulation using the four zonally averaged input variables $\{\overline{v}, \overline{v'\theta'_e}, \overline{\theta_e}, \overline{\theta'^2_e}\}$ by approximating the mass flux as a joint normal distribution (Pauluis et al., 2011; Wolfe, 2014). We have found that the following changes of input variables is advantageous in the variational calculations carried out below. In particular, changes in the mean flow variable $\overline{v}$ and the eddy flux variable $\overline{v'\theta'_e}$ lead to responses in the mean and eddy contributions to ψ that are challenging to compare to in part because the four input variables each have distinctive physical dimensions. Alternatively, we define the input variables as $\{\overline{v}, \overline{e}, \overline{\theta_e}, s\}$, where

$$s \equiv \sqrt{\overline{\theta'^2_e}} \tag{3.3}$$

is the standard deviation of θ_e, which, like $\overline{\theta_e}$, has units of temperature, and

$$\overline{e} \equiv \frac{\overline{v'\theta'_e}}{s}. \tag{3.4}$$

is an effective eddy velocity, which, like $\overline{v}$, has units of velocity. The effective eddy velocity is equal to the product of the variance of v and the correlation between v and θ_e.

This change of variables also crudely encodes some information about the structure of the eddies. If we imagine a vertically uniform eddy composed of a warm sector of air with $\theta_e = \overline{\theta_e} + s/2$ moving polewards with a velocity $\overline{e}$, and a cold sector of air with $\theta_e = \overline{\theta_e} - s/2$ moving equatorwards with a velocity of $\overline{e}$, the net poleward transport of θ_e (per unit length) from the eddy would be $\overline{v'\theta'_e}\Delta p/g = \overline{e}s\Delta p/g$, where Δp is the depth of the eddy in pressure. We can think of two end member cases, the first where the air moves very quickly but the contrast between the warm and cold sectors is very small, and the second where the air moves very slowly, but the contrast between the warm and cold sectors is very large. Both cases would lead to the same heat transport and $\overline{v'\theta'_e}$, but describe very different dynamics.

With these input variables, the STEM joint mass fluxes (between p surfaces and θ_e surfaces) are, starting from (Pauluis et al., 2011),

$$m_M\left[\phi, \overline{v}\left(\phi,p\right), \overline{\theta_e}\left(\phi,p\right), s\left(\phi,p\right), \theta_e\right] = L_x\,\overline{v}\left(\frac{1}{s\sqrt{2\pi}}\exp\left[-\frac{1}{2}\left(\frac{\theta_e-\overline{\theta_e}}{s}\right)^2\right]\right) \tag{3.5}$$

$$m_E\left[\phi, \overline{v}\left(\phi,p\right), \overline{\theta_e}\left(\phi,p\right), \overline{e}\left(\phi,p\right), \theta_e\right] = L_x\,\overline{e}\left(\left[\frac{\theta_e-\overline{\theta_e}}{s}\right]\frac{1}{s\sqrt{2\pi}}\exp\left[-\frac{1}{2}\left(\frac{\theta_e-\overline{\theta_e}}{s}\right)^2\right]\right) \tag{3.6}$$

where $L_x = 2\pi a\cos\phi$. Both expressions represent the product of 1) a scaling L_x that accounts for

the spherical geometry of the earth; 2) a factor ($\overline{v}$ or $\overline{e}$) that quantifies the strength of the circulation; and 3) a distribution function in large parentheses that relates information in pressure space (provided by the functions $\overline{\theta_e}$ and s, which are known, pre-calculated functions of p and ϕ) to information in θ_e space. The distribution function spreads the mass flux from either $\overline{v}$ or $\overline{e}$ over a region in θ_e space. The projection from a point in pressure space to a point in θ_e will be localized around its value of $\overline{\theta_e}$, but the shape of the distribution will be peaked about $\overline{\theta_e}$ for m_M and will be a dipole with a node at $\overline{\theta_e}$ for m_E. One feature about this projection which is sometimes overlooked is that both m_M and m_E will have mass fluxes on θ_e surfaces that do not exist in the atmosphere, including with $\theta_e < 0$ surfaces. This is a consequence of using exponential functions in the definition of m_M and m_E. Although having a mass flux on $\theta_e < 0$ surfaces is unphysical, it does not end up affecting the calculations very much, because the θ_e values are very far away from zero, and most of the mass flux is within a few standard deviations of $\overline{\theta_e}$ (see Section 1.5-1.6 in Chapter1 for further discussion).

When the joint mass fluxes are integrated over all θ_e values, then the mass flux averaged on p surfaces is recovered, i.e.

$$\begin{aligned} \int_{-\infty}^{\infty} m_M d\theta_e = &\quad L_x \overline{v} \\ \int_{-\infty}^{\infty} m_E d\theta_e = &\quad 0, \end{aligned} \tag{3.7}$$

so if the circulation is projected onto θ_e surfaces using the STEM, and then back onto p surfaces, the same result is obtained as if the circulation were just averaged onto pressure surfaces.

Using these variables we can define some convenience functions

$$f_M = \int_{-\infty}^{\theta_e} m_M d\theta_e' \tag{3.8}$$

$$= L_x \overline{v} \frac{1}{2} \mathrm{erf}\left(\frac{\theta_e - \overline{\theta_e}}{\sqrt{2}s}\right) \tag{3.9}$$

$$f_E = \int_{-\infty}^{\theta_e} m_E d\theta_e' \tag{3.10}$$

$$= - L_x \overline{e} \frac{1}{\sqrt{2\pi}} \exp\left[-\frac{1}{2}\left(\frac{\theta_e - \overline{\theta_e}}{s}\right)^2\right] \tag{3.11}$$

and using these expressions the mean STEM streamfunction can be written

$$\psi_M(\theta_e, \phi) = L_x \int f_M \frac{dp}{-g} \tag{3.12}$$

and the eddy STEM streamfunction can be written

$$\psi_E(\theta_e, \phi) = L_x \int f_E \frac{dp}{-g} \tag{3.13}$$

where $\overline{v}$ and $\overline{e}$ must remain inside the integral in p since they are dependent on p.

Although these expressions do not explicitly appear in the initial formulation of the STEM of Pauluis et al. (2011), they do appear subsequently in the follow on work of Wu and Pauluis (2013) and analogous expressions appear in an oceanographic context in Wolfe (2014) where the thermodynamic coordinate is buoyancy and the analysis is carried out for a Boussinesq fluid.

Additionally, we can calculate the "partial derivatives" of f_M, i.e. the derivative of f_M of with respect to a single input variable with the other variables held constant:

$$\frac{\partial f_M}{\partial \overline{v}} = - L_x \left(\frac{1}{2} \mathrm{erf} \left[\frac{\theta_e - \overline{\theta_e}}{\sqrt{2} s} \right] \right) \tag{3.14}$$

$$\frac{\partial f_M}{\partial \overline{\theta_e}} = - L_x \frac{\overline{v}}{s} \left(\frac{1}{\sqrt{2\pi}} \exp \left[-\frac{1}{2} \left(\frac{\theta_e - \overline{\theta_e}}{s} \right)^2 \right] \right) \tag{3.15}$$

$$\frac{\partial f_M}{\delta s} = - L_x \frac{\overline{v}}{s} \left(\frac{\theta_e - \overline{\theta_e}}{s} \frac{1}{\sqrt{2\pi}} \exp \left[-\frac{1}{2} \left(\frac{\theta_e - \overline{\theta_e}}{s} \right)^2 \right] \right), \tag{3.16}$$

and similarly for f_E

$$\frac{\partial f_E}{\partial \overline{e}} = - L_x \left(\frac{1}{\sqrt{2\pi}} \exp \left[-\frac{1}{2} \left(\frac{\theta_e - \overline{\theta_e}}{s} \right)^2 \right] \right) \tag{3.17}$$

$$\frac{\partial f_E}{\partial \overline{\theta_e}} = - L_x \frac{\overline{e}}{s} \left(\left[\frac{\theta_e - \overline{\theta_e}}{s} \right] \frac{1}{\sqrt{2\pi}} \exp \left[-\frac{1}{2} \left(\frac{\theta_e - \overline{\theta_e}}{s} \right)^2 \right] \right) \tag{3.18}$$

$$\frac{\partial f_E}{\partial s} = - L_x \frac{\overline{e}}{s} \left(\left[\frac{\theta_e - \overline{\theta_e}}{s} \right]^2 \frac{1}{\sqrt{2\pi}} \exp \left[-\frac{1}{2} \left(\frac{\theta_e - \overline{\theta_e}}{s} \right)^2 \right] \right). \tag{3.19}$$

These equations will become useful in defining the functional derivatives of ψ_M and ψ_E.

3.3 STEM Functional Derivatives

Since the values of the streamfunction can be computed for each latitude ϕ separately, we can consider the STEM streamfunction operating on every latitude independently. We here define a functional derivative which represents the separate response of ψ to any of the four input variables. We have formulated functional derivatives in both the original input variables $\{\overline{v}, \overline{v'\theta'_e}, \overline{\theta_e}, \overline{\theta'^2_e}\}$ and the alternate input variables as $\{\overline{v}, \overline{e}, \overline{\theta_e}, \overline{s}\}$, and here only present the analysis on the latter set. The STEM functional derivatives can be found by perturbing the pressure profile of a single input variable, denoted by η with an arbitrary pressure dependent perturbation φ, multiplied by an infinitesimal variable ϵ. In this way, φ

can be similar in size to η, but the small size of the perturbation is guaranteed by making ϵ small. We thus generate a perturbation $\eta \to \eta + \epsilon\varphi$ leading to a perturbed streamfunction ψ

$$\psi(\eta + \epsilon\varphi) = \int f(\eta + \epsilon\varphi)dp/-g. \tag{3.20}$$

where $f = f_M + f_E$.

The functional derivative of ψ with respect to η, $\frac{\delta\psi}{\delta\eta}$ is defined via

$$\lim_{\epsilon\to 0}\frac{\psi(\eta + \epsilon\varphi) - \psi(\eta)}{\epsilon} = \int \left(\varphi\frac{\delta\psi}{\delta\eta}\right)\frac{dp}{-g}, \tag{3.21}$$

since φ, η, and $\delta\psi/\delta\eta$ are all functions of pressure at each latitude, $\delta\psi/\delta\eta$ is a function of p and θ_e which quantifies how the perturbation in η is projected into θ_e space. In other words, for every value of θ_e, we take the convolution of $\delta\psi/\delta\eta$ and φ to project φ onto a perturbation in ψ.

To calculate the STEM functional derivatives, we start by expanding f for small ϵ:

$$f(\eta + \epsilon\varphi) = f(\eta) + \epsilon\frac{\partial f}{\partial\eta}\varphi + O(\epsilon^2) \tag{3.22}$$

and inserting into equation (3.20) in ϵ and the left side of (3.21) to find

$$\lim_{\epsilon\to 0}\frac{\psi(\eta + \epsilon\varphi - \psi(\eta)}{\epsilon} = \int \left(\varphi\frac{\partial f}{\partial\eta}\right)\frac{dp}{-g}. \tag{3.23}$$

By comparing equations (3.21) and (3.23) we find that

$$\frac{\delta\psi}{\delta\eta} = \frac{\partial f}{\partial\eta} \tag{3.24}$$

so that we identify the functional derivatives of ψ with the partial derivatives of f, i.e. equations (3.14-3.19). We note that equation (3.24) assumes that the Taylor expansion for f is possible; this is true for the STEM f since it is the product of various exponential and linear functions.

From equations (3.14) and (3.19) we find that the functional derivatives can be written as the product of three factors:

$$\frac{\delta\psi}{\delta\eta} = -L_x(\phi)S(\phi,p)K\left(\frac{\theta_e - \overline{\theta_e}(\phi,p)}{s(\phi,p)}\right), \tag{3.25}$$

where L_x is a geometric factor, S is a "sensitivity" factor which controls how much each point in the atmosphere contributes to the perturbation in θ_e space, and K is a kernel which controls the projection of the circulation from pressure to θ_e space. The kernel K can also be thought of as determining the

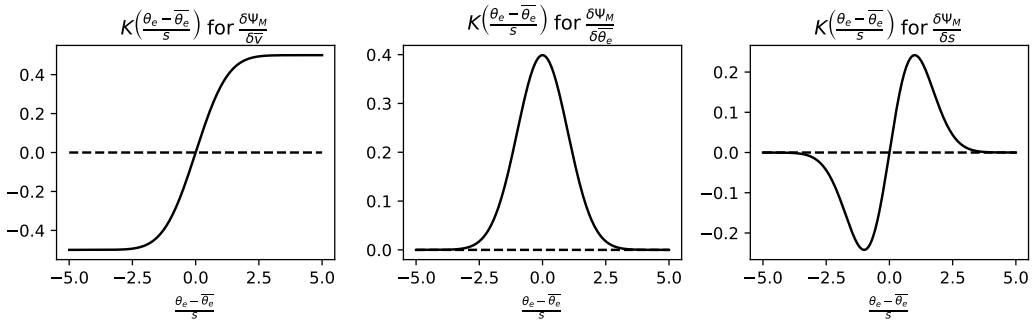

Figure 3.1: The kernels of ψ_M. Note that the geometric factor $2\pi a \cos\phi$ has been neglected.

shape of the perturbation in θ_e space.

The kernels for ψ_M are shown in figure 3.1. The first kernel, $\delta\psi_M/\delta\overline{v}$ shows a smooth step structure which does not decay for $\theta_e \to \pm\infty$. The mean streamfunction perturbation from $\overline{v}$, $\delta_{\overline{v}}\psi_M$, will be closed because for physically realizable perturbations in $\overline{v}$ conserve mass in pressure space, in which case

$$\delta_{\overline{v}}\psi_M(\theta_e \to \pm\infty) = \pm\frac{L_x}{2}\int \pm\delta\overline{v}\frac{dp}{-g} = 0. \tag{3.26}$$

The second kernel, $\delta\psi_M/\delta\overline{\theta_e}$, is proportional to a Gaussian. Increasing $\overline{\theta_e}$ increases the strength of the circulation around the value of $\overline{\theta_e}$ at that given pressure level. The third kernel is $\delta\psi_M/\delta s$ which has a dipole structure. Perturbations to s at a given pressure level will increase the circulation at $\theta_e > \overline{\theta_e}$, and decrease it at $\theta_e < \overline{\theta_e}$.

The sensitivity factor S for $\delta\psi_M/\delta\overline{v}$ is 1, and the sensitivity factor for $\delta\psi_M/\delta\overline{\theta_e}$ and $\delta\psi_M/\delta s$ is $\overline{v}/s$. At each point is uniformly sensitivity to perturbations in $\overline{v}$, but the sensitivity of the atmosphere to perturbations in $\overline{\theta_e}$ and s will depend on the distribution of $\overline{v}/s$ in the atmosphere. For example, where the magnitude of $\overline{v}/s$ is large, a change in $\overline{\theta_e}$ will cause a large perturbation in ψ_M. Note that since

$$\int \overline{v}\frac{dp}{-g} = 0, \tag{3.27}$$

$\overline{v}$ will change sign somewhere in the atmosphere if it is non zero anywhere. This implies that the kernels of ψ_M, when integrated over the entire atmospheric column, will appear with both positive and negative prefactors. As an example, while the kernel of ψ_M is a monopole, when integrated over the entire atmospheric column the affect will appear as a dipole. This will be illustrated with an example in Section 3.4.

The kernels for ψ_E are shown in figure 3.2. The first kernel, $\delta\psi_E/\delta\overline{e}$ shows a Gaussian, since increasing the effective eddy velocity increases the mass flux around the $\overline{\theta_e}$ at ever pressure level. The second kernel, $\delta\psi_E/\delta\overline{\theta_e}$, shows a dipole structure. Increasing $\overline{\theta_e}$ at a single pressure level has the impact of shifting the eddy circulation to higher values of θ_e, since the eddy fluctuations have on average a greater θ_e. The third kernel, $\delta\psi_E/\delta s$, has a tripole structure. When the standard deviation of temperature s is increased, the circulation is increased at the flanks of the distribution, through increasing the standard deviation s in the Gaussian distribution.

The sensitivity factor for $\delta\psi_E/\delta\overline{e}$ is 1, the sensitivity factors for $\delta\psi_E/\delta\overline{\theta_e}$ and $\delta\psi_E/\delta s$ is $\overline{e}/s$. At each point ψ_E is uniformly sensitivity to perturbations in $\overline{e}$, but the sensitivity of ψ_E will depend to perturbations in $\overline{\theta_e}$ and s will depend on the the distribution of $\overline{e}/s$. As stated above, $\overline{e}$ reflects the

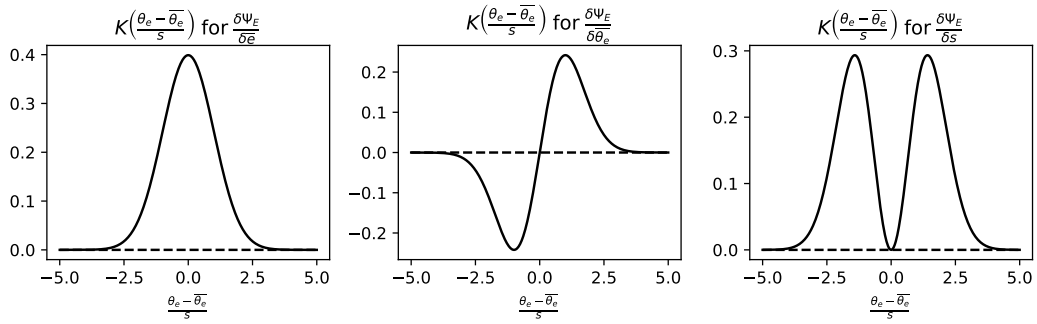

Figure 3.2: The kernels of ψ_E. Note that the geometric factor, $L_x = 2\pi a \cos\phi$, has been neglected.

eddy mass flux, while s depends on the variability of θ_e. The regions of the atmosphere with maximum sensitivity will be regions where the effective eddy velocity is larger, and the variability of s is small. This means that there could be two regions of the atmosphere with the same $\overline{v'\theta'_e}$, but different sensitivity to perturbations in $\overline{\theta_e}$ and s, depending on the decomposition of $\overline{v'\theta'_e}$. In particular, using our simplified picture of an eddy from Section 3.2, regions with eddies which move air very quickly but which have a very low contrast between warm and cold sectors will be the most sensitive to perturbations. This behaviour will be illustrated with a toy model in Section 3.4, and the distributions of $\overline{e}/s$ will be considered in Section 3.5.

Figures 3.1 and 3.2 suggest an answer to one of the key questions that we asked in the introduction. The analytical expressions developed here give yield results that are consistent with those of Wu and Pauluis (2013), and other studies reviewed in the introduction, because as long as the perturbations are not too large, then the mathematical structure of the STEM enforces a robust shape to the response, independently of the model, control climatology and perturbation. A change in $\overline{\theta_e}$ will shift the circulation up or down, a change in $\overline{e}$ or $\overline{v}$ will act to change the intensity of the circulation, localized around the surface $\theta_e = \overline{\theta_e}$, and a changes in s will act to change the width of the circulation.

3.3.1 Poleward heat transport sensitivities

Since the total vertically integrated heat fluxes are the same in pressure coordinates or θ_e coordinates (as shown in Section 1.2.5), we can calculate the heat transport functional derivatives by taking derivatives of the mean and eddy poleward heat transport, defined as

$$\begin{aligned} H_M = &\quad L_x \int \overline{v}\overline{\theta_e} \tfrac{dp}{-g} \\ H_E = &\quad L_x \int \overline{e} s \tfrac{dp}{-g}, \end{aligned} \tag{3.28}$$

so that we obtain the mean heat transport

$$\frac{\delta H_M}{\delta \overline{v}} = L_x \overline{\theta_e} \tag{3.29}$$

$$\frac{\delta H_M}{\delta \overline{\theta}} = L_x \overline{v} \tag{3.30}$$

$$\frac{\delta H_M}{\delta s} = 0 \tag{3.31}$$

and for the eddy heat transport

$$\frac{\delta H_E}{\delta \overline{e}} = L_x s \tag{3.32}$$

$$\frac{\delta H_E}{\delta \overline{\theta}} = 0 \tag{3.33}$$

$$\frac{\delta H_E}{\delta s} = L_x \overline{e}. \tag{3.34}$$

This result is the same if we take the same if we were to take derivatives of the heat transport in either p coordinates or θ_e coordinates. From this expression, we find that perturbing s has no effect on the mean circulation and perturbing $\overline{\theta_e}$ has no impact on the eddy heat transport. For the eddy circulation, perturbing either $\overline{e}$ or s will change the heat transport proportionally to the other. In other words, perturbing the effective eddy velocity is more effective at changing the heat transport where the atmosphere is most variable and vice versa.

An important difference between using the original set of variables from Pauluis et al. (2011), $\left(\overline{v'\theta'_e}, \overline{\theta'^2_e}\right)$, and the set of variables used here, $(\overline{e}, s)$, is that in the former choice $\delta H_E/\delta\overline{\theta'^2_e} = 0$, whereas in the latter choice $\delta H_E/\delta s \neq 0$. This is because the latter explicitly splits the eddy covariance into $\overline{e}$ and s, whereas the original formulation includes the heat flux as a single variable. This means that the conclusions of Chapter 2 (Fajber et al., 2018) are not directly comparable with this Chapter, since Chapter 2 uses a different set of variables and the change in variance will not contribute strongly to the heat transport under that formulation, unlike the formulation here where the change in s, with $\overline{e}$ fixed, which will affect the heat transport.

3.4 Toy Model

To help interpret of the mathematical results in the previous Subsection, we create a toy model to calculate the streamfunction and functional derivatives at a single latitude. This model uses realistic atmospheric data but makes use of vertical (layered) averaging to simplify the analysis. In particular, we break the atmosphere into a small number of uniform layers to simplify the pressure integrals, e.g.

$$\psi_M = L_x \sum_i \overline{v}_i \frac{1}{2} \mathrm{erf}\left(\frac{\theta_e - \overline{\theta_e}_i}{\sqrt{2} s_i}\right) \frac{dp_i}{-g} \tag{3.35}$$

$$\psi_E = L_x \sum_i \overline{e}_i \frac{1}{\sqrt{2\pi}} \exp\left(-\frac{1}{2}\left(\frac{\theta_e - \overline{\theta_e}_i}{s_i}\right)^2\right) \frac{dp_i}{-g} \tag{3.36}$$

where dp_i is the pressure span of layer i, $\overline{v_i}$ is the mean meridional velocity in the ith layer, and the other STEM input variables are defined similarly. The streamfunction perturbation for a perturbed STEM input variable, η, can be written

$$\delta_\eta \psi = \sum_i \frac{\delta \psi}{\delta \eta}_i \delta\eta_i \frac{dp_i}{-g} \tag{3.37}$$

where $\delta\eta_i$ is the perturbation to STEM input variable η in layer i.

The STEM input variables are from the ERA5 reanalysis after a zonal and annual mean, taken at 40°N, to be representative of a midlatitude circulation. We divide the troposphere between 1000 hPa and 200 hPa into two 400 hPa thick layers, centered at 800 hPa and 400 hPa. By choosing the layers to be of equal thickness, a vertical mass weighted mean is just the sum of the upper and lower layers. The inputs for the toy model are obtained by averaging the four input STEM variables over these layers (the line segments in figure 3.3). In the toy model profile for $\overline{v}$ we also remove a vertical mean from the profile so that $\sum_i \overline{v_i} dp_i/-g = 0$. This effectively adds a small meridional flow above 200 hPa into the toy model.

The streamfunctions from the toy model are shown in figure 3.4. The circulation of the toy model is most naturally expressed in units of $L_x 800\text{hPa}/g\text{ms}^{-1}$, which is the mass flux from a 1ms^{-1} wind across the area of the toy model. We will begin with the discussion of the eddy streamfunction due to the relatively large contribution of ψ_E to ψ_M in θ_e space in the extratropics. The contributions from each vertical level show individual Gaussians centered around each $\overline{\theta_e}$. The differences in $\overline{\theta_e}$ separate out the contributions of each layer to a different region of θ_e space: $\psi_E(800)$ is centered at a lower θ_e value than $\psi_E(400)$. A single value of the streamfunction cannot be related to any single point in pressure space because each value of the streamfunction contains contributions from different pressure levels.

The effective eddy velocity $\overline{e}$ is stronger in the lower atmosphere, so the peak of $\psi_E(800)$ is noticeably larger than that of $\psi_E(400)$. The zonal standard deviation of θ_e decreases with height, so the widths of $\psi_E(800)$ is also larger. The total streamfunction is peaked around the vertical mean $\overline{\theta_e}$ of 315 K, but it is slightly asymmetric even though the contributions from each vertical level is symmetric. The asymmetry is caused by the vertical variation of parameters, and not by the projection of the streamfunction onto θ_e space (since m_E is symmetric). The integral over θ of ψ_E is proportional to the heat transport H, and the area is proportional to $\overline{e}s$. The majority of the heat transport in the toy model is dominated by $\psi_E(800)$ because it has more area under the streamfunction than $\psi_E(400)$.

Equation (3.19) is used to calculate the functional derivatives for the toy model ψ_E (figure 3.5). The functional derivatives are localised to different regions of θ_e space; nearer to the surface, the sensitivity is centered at lower θ_e values, and covers a larger range of θ_e values than in the upper troposphere. All

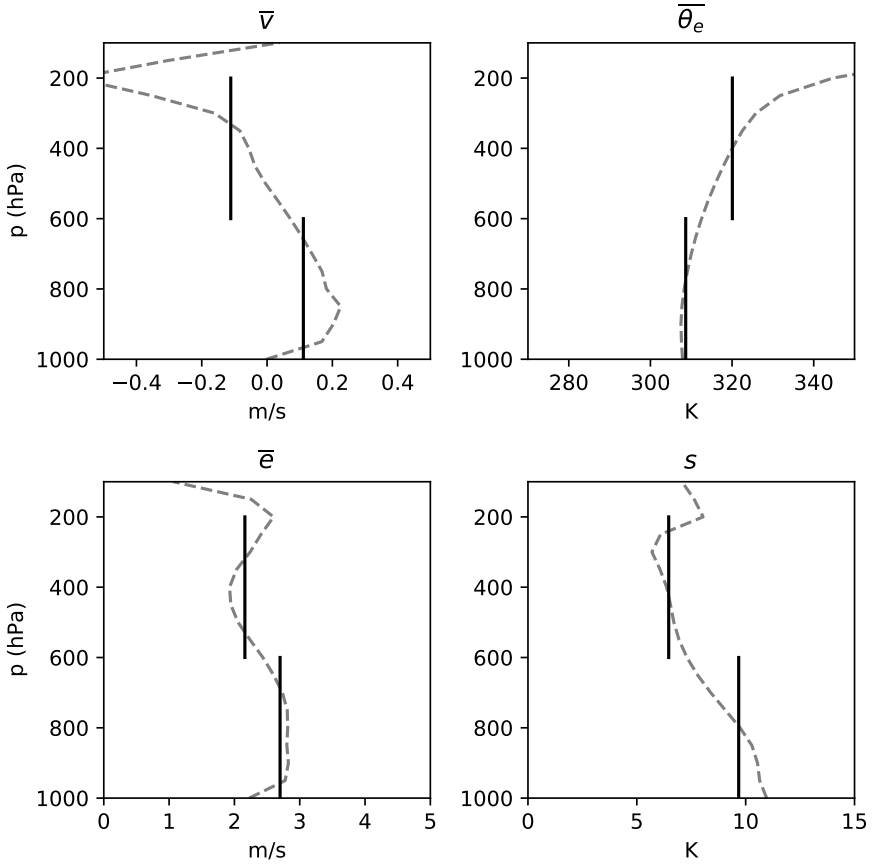

Figure 3.3: Idealized toy model for calculating the STEM streamfunction at a single latitude. The solid lines are the ERA5 zonal mean, annually averaged, data for 40°N, and the vertical line segments show the data averaged over the corresponding layers that make up the toy model.

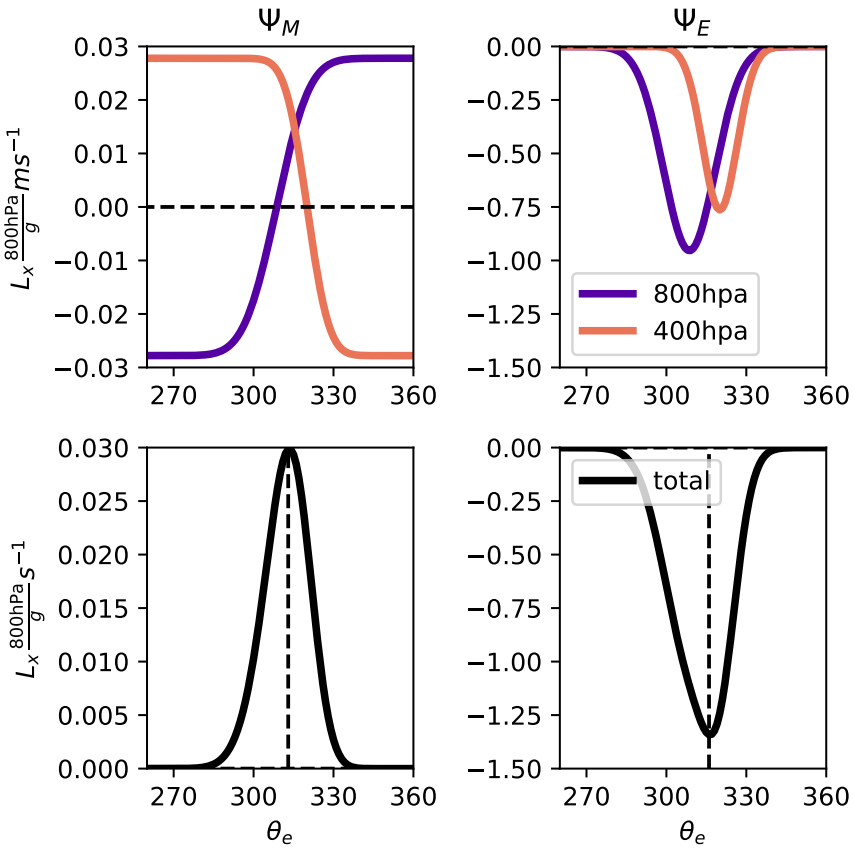

Figure 3.4: The streamfunctions calculated from the toy model. Top row: the contributions to the streamfunction from the different layers; bottom row: the total streamfunction summed over the two vertical layers. Left column: the mean streamfunction contributions; right column: the eddy streamfunction contributions.

of the eddy functional derivatives are closed, so that $\delta\psi_E/\delta\eta \to \pm\infty$. This means that all perturbations will result in a closed circulation.

The functional derivatives $\delta\psi_E/\delta\overline{e}$ are monopoles, that correspond to an intensification of the circulation without changing the range of θ_e of the circulation. Comparing $\delta\psi_E/\delta\overline{e}(800)$ with $\delta\psi_E/\delta\overline{e}(400)$, we see that the integral under the curve of $\delta\psi_E/\delta\overline{e}(800)$ is larger. This is because while $\delta\psi_E/\delta\overline{e}$ integrates to unity over the variable $\left(\theta_e - \overline{\theta_e}\right)/s$ it does not when it is integrated over θ_e. Changes in the $\overline{e}$ are more effective at changing the heat transport when s is larger.

The functional derivatives $\delta\psi_E/\delta\overline{\theta_e}$ are dipoles, corresponding to shifts of the circulation to greater values of θ_e for a warming perturbation. The shifts are centered around the value of $\overline{\theta_e}$ at each vertical level, and the size of the shift is proportional to $\overline{e}$. Layers with greater $\overline{e}$ will have larger shifts as more of the poleward and equatorward mass transport moves with $\overline{\theta_e}$. The shifts in the lower troposphere are more spread out in θ_e space (because of the greater s there), while the shifts in the upper troposphere are concentrated in θ_e space, so that the functional derivatives are more peaked.

The functional derivatives $\delta\psi_E/\delta s$ have two peaks, which are away from the central θ_e value. The total integral under these curve is proportional to $\overline{e}$, and so is larger in the lower troposphere. The sensitivities are more peaked in the upper troposphere where there are smaller values of s, similar to $\delta\psi_E/\delta\overline{\theta_e}$. The streamfunction spreads more in regions where $\overline{\theta_e}$ is larger.

To illustrate how these sensitivities combine over all of the vertical levels and over all of the different input variables, we introduce an idealized atmospheric perturbation, and take the convolution over pressure space (by summing over vertical levels in the toy model) to find the streamfunction changes. We assume that the perturbations are the same in both layers, with $\delta\overline{\theta_e} = 5\text{K}$, $\delta\overline{e} = 0.25\text{m/s}$, and $\delta s = 1K$. The relative sizes in the variables is to make them comparable, to previous global warming experiments, where the changes in ψ_E due to $\delta\overline{\theta_e}$ is much larger than that of the other variables (e.g. Wu and Pauluis, 2013).

The perturbed streamfunctions are shown in figure 3.6. The perturbations in ψ_E with respect to $\overline{e}$ are centered around the maximum of the climatological streamfunction (the dotted line in figure 3.4). The perturbations in the upper troposphere are at greater θ_e values than the maximum of the climatological ψ_E, so the total perturbation is slightly asymmetric. The sum of all of these perturbations is a net intensification, slightly off center of the climatological streamfunction maximum.

The perturbation to $\overline{\theta_e}$ results in two contributions to shift the streamfunction. However the offset of the two streamfunctions result in an asymmetry around the maximum value of the climatological streamfunction. The shift in the lower troposphere is also spread over a broader range of θ_e values than in the upper troposphere, which is more narrowly peaked. The sum of the two reflects this difference

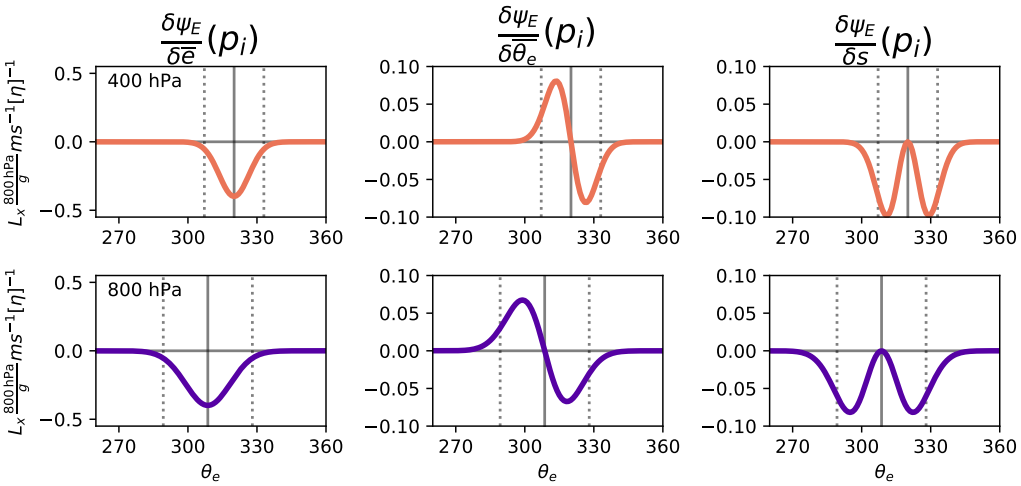

Figure 3.5: The functional derivatives of ψ_E for the toy model. The y axis labels correspond to the different layers. The $[\eta]^{-1}$ in label of the y axis corresponds the to the units of the variable being perturbed.

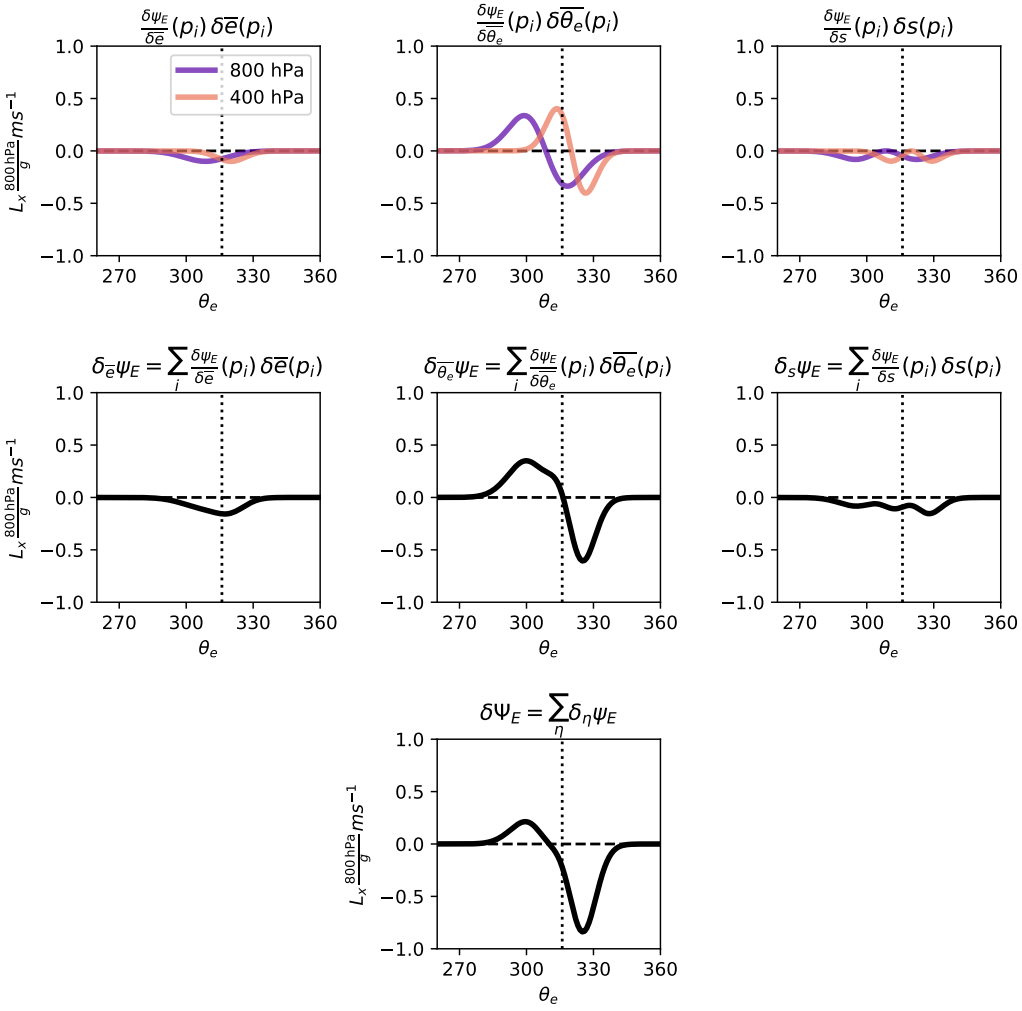

Figure 3.6: The response of ψ_E from the toy model to idealised vertically uniform perturbations of $\delta\overline{\theta_e}$ = 5K, $\delta\overline{e}$ = .25ms^{-1}, δs=1K. Top row: functional derivatives multiplied by the corresponding perturbation, middle row: the streamfunction perturbation calculated by summing over all layers, bottom row: the total perturbation summed over all variables, since the units for the kernels may differ. The dotted vertical line is the maximum of ψ_E, shown in figure 3.4.

between the upper and lower troposphere. The decrease in the streamfunction at low θ_e values is more spread out than the increase in the streamfunction at high θ_e values.

The perturbations in s both increase the streamfunction, however because their ranges do not overlap the increase of the streamfunction is spread over a broad range of θ_e values. The largest increase in the streamfunction occurs near $\theta_e = 330$K, where the the increases from both the lower and upper troposphere mutually reinforce.

The total perturbation in the streamfunction, $\delta\psi_E$, can be calculated by summing over all of the input variables. At lower θ_e values $\delta_{\overline{\theta_e}}\psi_E$, acts to decrease the circulation to shift it to higher θ_e values, while $\delta_{\overline{e}}\psi_E$ and $\delta_s\psi_E$ act to increase the circulation strength at all θ_e ranges. This results in a cancellation of the shift from $\delta_{\overline{\theta_e}}\psi_E$. At higher θ_e values $\delta_{\overline{\theta_e}}\psi_E$ changes signs, and so the shift is reinforced by the other variables. The result of this is that $\delta\psi_E$ is an asymmetric shift.

We note that these results would be different in a strongly stratified atmosphere. In the limit that the stratification over the troposphere (e.g. the difference in $\overline{\theta_e}$ between the top and bottom of the troposphere) becomes much larger than the mean s over the troposphere, then ψ_E becomes controlled by the vertical stratification (e.g. Pauluis et al., 2011, appendix C). Under this limit, each vertical level is essentially localized for all other levels in θ_e space. In the context of the toy model this would mean that the streamfunction contributions from the top and bottom layer would not overlap in θ_e space. The interpretation of actual changes in ψ_E based on results of the toy model are predicated on the assumption that the stratification in θ_e is relatively weak.

Unlike ψ_E, ψ_M contributions are not closed in any individual layer (figure 3.4). However the total streamfunction is closed because the contributions from the individual layers cancel out. Note that ψ_M is small compared to ψ_E, because the latitude we have chosen is in the Ferrell cell, where ψ_M is weak compared to ψ_E. Like ψ_E, the streamfunction is slightly asymmetric because the jump in ψ_M is more concentrated in θ_e space due to the difference in s between the lower and upper troposphere. The functional derivatives for ψ_M are shown in figure 3.8. Like ψ_E, the kernels are localised around the value of $\overline{\theta_e}$ in a given layer, and the kernels in the lower layer are projected onto a wider range of θ_e values because s is larger. Unlike ψ_E, the kernels for ψ_M are dependent on the sign of $\overline{v}$. Increasing $\overline{\theta_e}$ in the upper layer reduces the ψ_M, while increasing $\overline{\theta_e}$ in the lower layer increases ψ_M. This is consistent with the direction of circulation in the Ferrell cell (where ψ_M is positive); a positive change in $\overline{v}$ would increase the strength of the Ferrell cell if it happens in the lower branch, and reduce the strength if it happens in upper branch.

As for ψ_E we consider the response of the toy model to a set of idealised perturbations. The profiles of $\delta\overline{\theta_e}$ and δs are the same, but for $\delta\overline{v}$ we choose a perturbation of -0.01 m/s in the 800 hPa layer and

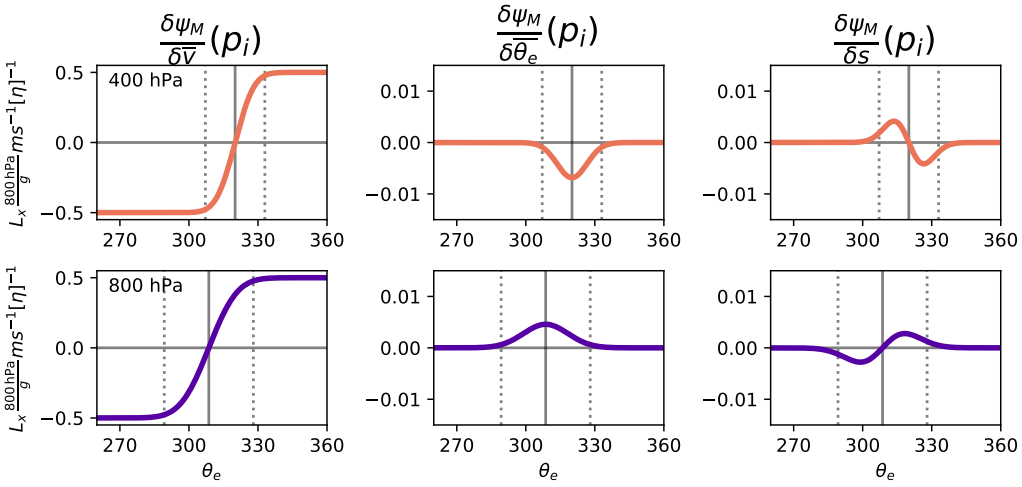

Figure 3.7: As for figure 3.5, but for ψ_M.

a perturbation of 0.01m/s in the 400 hPa layer. By choosing a perturbation that is mass conserving we ensure that the total perturbation that is recovered is also mass conserving.

This is shown in figure 3.7 for $\delta_{\overline{v}}\psi_M$ (left column). By construction the perturbations cancel out as $\theta_e \to \pm\infty$, and so that the only non-zero perturbation to the streamfunction is around the θ of the maximum climatological ψ_M. The perturbation in $\delta_{\overline{\theta_e}}\psi_M$ (center column) has a large increase of the streamfunction in the upper layer, and a large decrease of the streamfunction in the lower layer. The perturbations in s overly each other in a way to create a tripolar pattern (right column). Increasing s increases ψ_M near the central value of θ_e and decrease it near the extreme values. This has the effect of concentrating ψ_M closer to the central θ_e value.

Even though the functional derivatives for ψ_M have one fewer critical points than for ψ_E they produce similar results because $\overline{v}$ changes sign once in the atmosphere. For instance $\delta\psi_M/\delta\overline{\theta_e}$ is a monopole while $\delta\psi_E/\delta\overline{\theta_e}$ is a dipole, but since $\overline{v}$ changes signs between the upper and lower troposphere the net effect of $\delta\psi_M/\delta\overline{\theta_e}$ is dipolar. This means that $\delta_{\overline{\theta_e}}\psi_M$ results in a shift in the circulation, analogous to $\delta_{\overline{\theta_e}}\psi_E$.

3.5 Application to a Climate Change Experiment

To illustrate the application of the analysis in the previous Sections we consider the STEM streamfunction and poleward heat transport response to climate change under different background states. The background states are obtained from different estimates of the observed state of the atmosphere from reanalysis and from a climate model.

3.5.1 Data Sets

To illustrate the response of the isentropic circulation of a climate model with a realistic climate forcing applied, we use the Community Earth System Model (CESM) Large Ensemble Project (LENS, Kay et al., 2015). The annual average zonal mean STEM input variables are calculated from six hourly data on pressure levels for ensemble members two through six, averaged over the years 1990-2004 and 2071-2080 (these two time periods are chosen because six hourly output was chosen for these two time slices). To compare with the CESM data we use two reanalysis products, the ERA5 dataset (Copernicus Climate Change Service Climate Data Store, 2017) and the modern era reanalysis for research and analysis version 2 (MERRA2, Gelaro et al., 2017). The annual average zonal mean STEM input variables are calculated from six hourly data on pressure levels, averaged over the years 1979-2016.

Using these three different datasets lets us assess whether the CESM model has any bias in its modern day climate simulation which might influence its future predictions of the moist isentropic circulation.

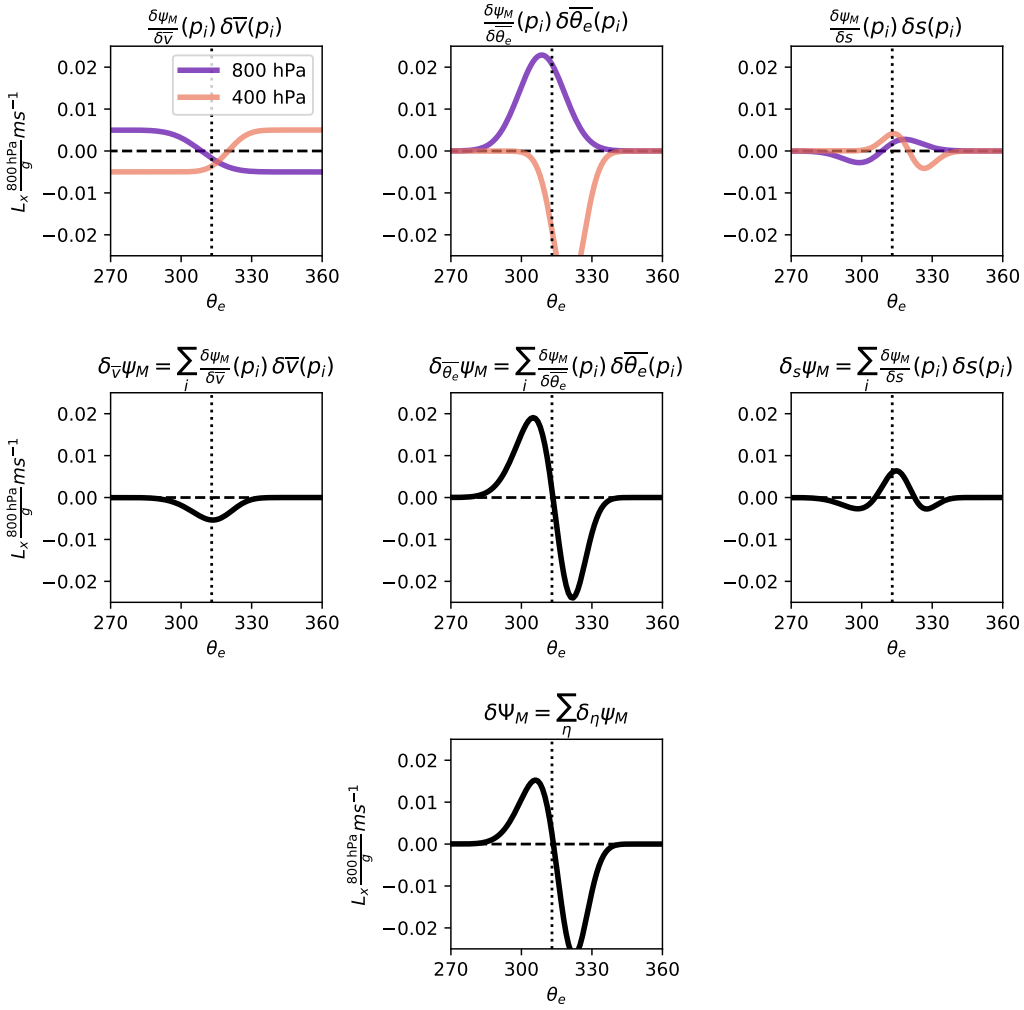

Figure 3.8: As for figure 3.6, but for ψ_M. The profiles of $\delta\overline{\theta_e}$, δs are the same, but $\delta\overline{v}$ is chosen to be -0.01 m/s in the 800 hPa layer and 0.01 m/s in the 400 hPa layer.

Since we do not make an assessment of which reanalysis product is more realistic, the CESM model should be compared to multiple reanalysis products in order to make a fair statement about its realism. As we will show later, the difference between the variability in θ_e surfaces between MERRA2 and ERA5 is larger than the difference between CESM and ERA5.

The four input variables for the STEM are shown in figure 3.9. The overall impression is that CESM and ERA5 are more similar than CESM and MERRA2. The distinctive spatial structure and greater magnitude of the standard deviation of θ_e, s, in MERRA2 compared with the other data sets is particularly striking. Additionally, the maxima of s in both the Northern and Southern Hemisphere are in the midtropopshere, above the boundary layer in MERRA2, while in CESM and ERA5 they occur near the surface. This difference has consequences for the circulation in θ_e coordinates as well as the heat and mass transports, which will be discussed later.

In general the different data sets agree better in the first order statistics $\overline{\theta_e}$ and $\overline{v}$ than they do in the second order statistics related to the eddies $\overline{e}$ and s. The latitudes of the Hadley and Ferrell cells are approximately the same between all of the data sets, and the gross moist stability (see appendix A for discussion) is very similar outside of the tropics, where the increase in tropical moisture in MERRA2 reduces the gross stability there. The southern polar cell is resolved differently between the different data sets, since $\overline{v}$ is notably different polewards of 60° south. This discrepancy is likely to have minimal effects in our analysis, since ψ_E dominates ψ_M in these latitudes, and ψ_E does not depend on $\overline{v}$.

Part of the difference in s between the MERRA2 and ERA5 datasets is possibly due to the differences in the data assimilation methods between the two reanalysis products. The MERRA2 reanalysis uses a 3 dimensional variational analysis (Gelaro et al., 2017) whereas ERA5 reanalysis uses a 4 dimensional variational analysis (Copernicus Climate Change Service Climate Data Store, 2017). The use of the 4 dimensional variational analysis has a smoothing effect on the data which may reduce some of the variability in the atmosphere. Additionally the MERRA2 reanalysis assimilates a large amount of satellite data, including aerosol data, which is not done by the ERA5 reanalysis. These extra observations from a diverse range of sources may also impact the atmospheric variability and s. Another contributing factor could be from the different physical parametrization schemes used in the two underlying models. Further understanding the differences in atmospheric variability represented between these reanalysis is an important topic of future research.

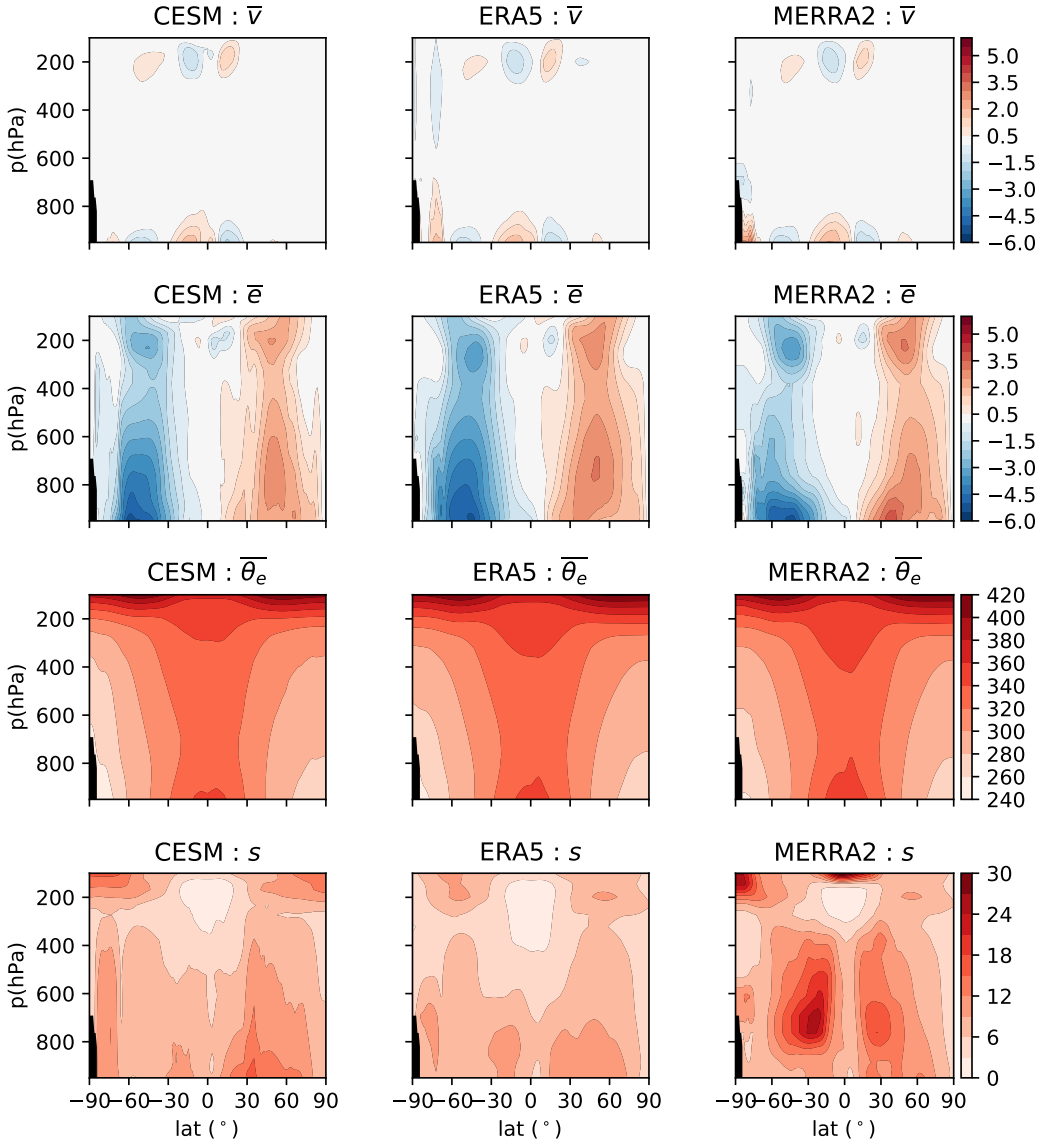

Figure 3.9: The input STEM variables for the 3 different data sets used here. The black region around Antarctica has been masked out.

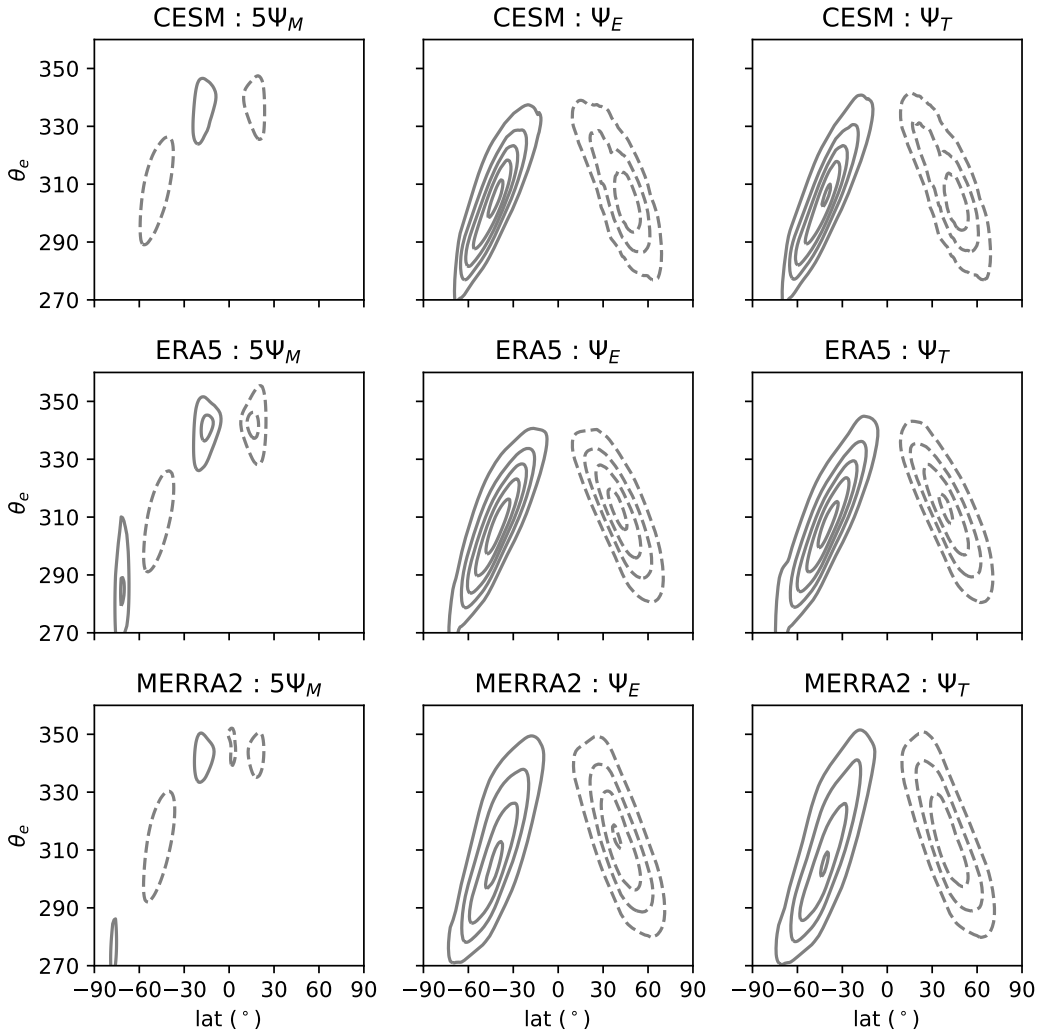

Figure 3.10: The mean, eddy, and total streamfunctions on θ_e coordinates. Top row: from CESM data, Middle row: from ERA5 reanalysis data, Bottom row: from MERRA2 reanalysis data. The contour interval is $4\text{x}10^{10}\text{kgs}^{-1}$, and the zero contour is not shown.

3.5.2 Comparison of Circulations in θ_e space

The streamfunctions ψ_M, ψ_E, and ψ_T are show in figure 3.10. The ψ_M are relatively inconsistent between the different data sets, but the circulation is a small component of ψ_T, so it does not contribute appreciably to the discrepancies among the total streamfunctions. The largest differences in the streamfunctions comes from the eddy contribution. In the Northern Hemisphere midlatitudes the relative maximum of ψ_E consistent for all of the data sets. The circulation center is in different positions, in different data sets, with CESM putting the circulation maximum further polewards by about 5.5° than the other data sets.

The eddy streamfunction in CESM has a weaker circulation in the Northern Hemisphere subtropics.

In the Southern Hemisphere ψ_E in CESM and ERA5 is about 25% greater than in MERRA2. The ψ_E is spread over a narrower range of θ_e values (by about 15 K) in CESM and ERA5 than in MERRA2. This is because s is very large in the Southern Hemisphere storm track in MERRA2, and this spreads the mass transport in those layers over a larger range of θ_e levels than in the other data sets.

The differences in ψ_E imply differences in the way that the eddy heat transport is maintained by the dynamics of the atmosphere. To summarize these differences we split the eddy heat transport, H_E can into a mass flux $\mathcal{M}_E$ and dynamic stratification Δ_E

$$H_E = \mathcal{M}_E \Delta_E. \tag{3.38}$$

$\mathcal{M}_E$ is the total massflux in one branch (either the polewards or equatorwards) of the circulation (see appendix A for the mathematical definitions of $\mathcal{M}_E$ and Δ_E). By mass conservation the total mass fluxes in both branches must be equal. The dynamic stratification, Δ_E, is the difference between the mass flux weighted θ_e in the poleward and equatorward branches of the circulation. The dynamic stratification Δ_E plays an analagous role to the gross moist stability in the calculation of the heat transport by the mean circulation (Neelin and Held, 1987). Pauluis et al. (2011) showed that Δ_E depends on both $\partial_p \overline{\theta_e}$ and also s, being equal to s in the limit of a vertically homogeneous atmosphere.

These quantities are all related to the geometry of ψ_E. The eddy heat transport is the integral of ψ_E, $H_E = \int_{-\infty}^{\infty} \psi_E d\theta_e$. The total mass flux is related to the maximum of ψ_E since if we integrate from one boundary over one branch of the circulation (e.g. we include only the poleward values), we will obtain the extremum of the streamfunction at any given latitude (e.g. Pauluis et al., 2010, , see appendix A for further details). If ψ_E is spread across a wider range of θ_e values, then Δ_E will be larger and vice versa. Using H_E, $\mathcal{M}_E$, and Δ_E summarizes the geometry of ψ_E in a way that facilitates the comparison between different data sets.

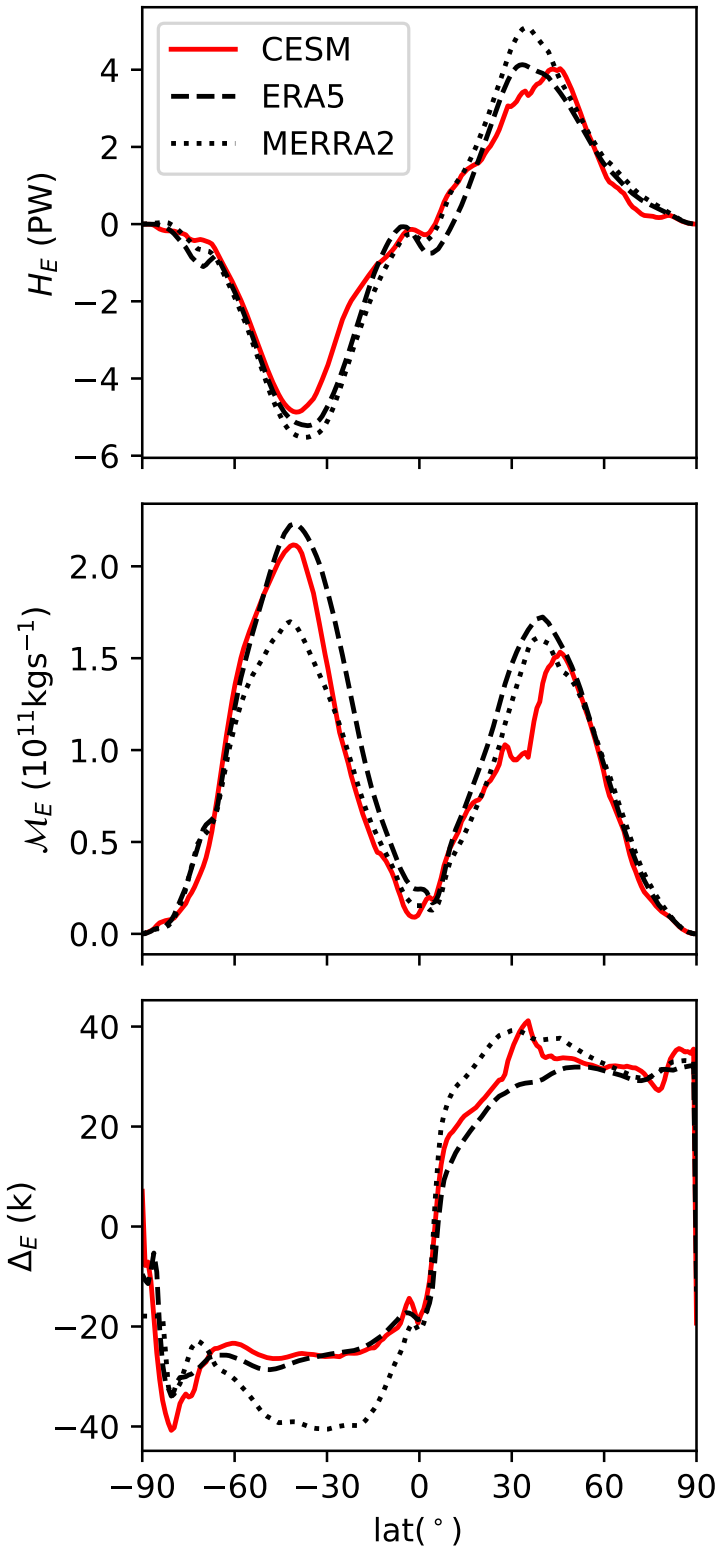

Figure 3.11: Top row: The eddy poleward heat transport for the three data sets, Middle row: the total eddy mass flux $\mathcal{M}_E$, Bottom row: the dynamic stratification Δ_E.

The decomposition of the heat transport using equation (3.38) is shown in figure 3.11. The eddy heat transport is very similar for ERA5 and MERRA2 in the Southern Hemisphere, while CESM has a slightly smaller peak. In the Northern Hemisphere CESM and ERA5 have relatively similar H_E, but MERRA2 has a larger peak heat transport. In the Northern Hemisphere, the disagreement between H_E across data sets is larger than in the Southern Hemisphere.

The net heat transport is constrained by net diabatic heat fluxes in the atmosphere (e.g. Trenberth and Stepaniak, 2003b), however this constraint does not apply to $\mathcal{M}_E$ and Δ_E individually. In the Southern Hemisphere, $\mathcal{M}_E$ is lower for MERRA2 than CESM and ERA5, while the Δ_E is much larger. This is due to the large difference in s between MERRA2 and the other data sets, which acts to spread out ψ_E over a wider range of θ_e values. However; since H_E is similar between the different data sets, $\mathcal{M}_E$ must be smaller for MERRA2. Interestingly, the maximum of $\overline{e}$ is similar in CESM and ERA5, but $\overline{e}$ is more constrained to the lower troposphere in MERRA2 in the southern hemisphere midlatitudes where s is very large. This means that even though the covariances are similar, the sensitivities of the data sets will be different, as shown in the next Section.

3.5.3 Perturbations to the Eddy Streamfunction

The differences between representation of STEM input variables affords us an opportunity to study the impact of the background state on perturbations to the streamfunction in θ_e coordinates. In particular, we can compare the relatively low s background state of ERA5 and CESM to the relatively high s background state of MERRA2. This is especially interesting as both ERA5 and MERRA2 are reanalysis products, so the difference between them gives us some insight into what range of possible responses are spanned by observationally constrained data sets.

To make this comparison, we rewrite the perturbed variables as

$$\eta^p = \eta^c|_d + \delta\eta|_{CESM} \tag{3.39}$$

where $\eta^c|_c$ is the STEM input set from one of CESM, ERA5, or MERRA2, and $\delta\eta|_{CESM}$ is the set of climate change perturbations from CESM. These new variables combine the background state from one of the data sets with the climate change perturbations from CESM. Using equation (3.39) we can calculate the linearizations around any variable using the numerical procedure from equation (3.2).

The new perturbed states mix projected future climate perturbations with the control circulations from climate models and renalysis. This is the inverse of what is done in the context of bias correction, where differing projected climate perturbations are combined with information from a single (usually

observed) control state to generate future climate projections. That method assessed how the differences between model climate responses impact the range of future climate projections. However, in the context of this study, the demonstrated differences between two reanalysis products leads us to ask whether or not the differences in the background circulation also have an impact on the range of future climate projections. Our method is useful in answering this question, since by using the projected climate perturbations from a single model all of the remaining difference is due to the differences in the control circulation. Comparing the results using the CESM control circulation with the two reanalysis circulations allows us to assess what impact the biases in the control climate of CESM will have on the response of the moist isentropic circulation. Our approach is similar to the comparison of radiative kernels calculated from differences in observed and simulated climate states (Soden et al., 2008).

In general, projected differences in future climate change will depend on the background circulation, and so cannot be taken to be independent of the circulation. However, using the climate model perturbations with the reanalysis datasets is justified in part because there are no estimates of future climate change from the reanalysis datasets, and so we can use any estimate of future climate change. Additionally, there is relatively small spreads in the simulated temperature trends compared with the spatial distribution of temperature trends (Vallis et al., 2015), which implies that the response of $\overline{\theta_e}$ may not differ much between different models, so $\delta_{\overline{\theta_e}}\psi_E$ may depend more strongly on the background circulation than on the perturbation.

Since the perturbations in ψ_E are much larger than those of ψ_M, we will focus our analysis on this. The perturbations to the three input variables to ψ_E are shown in figure 3.12. The changes in $\overline{e}$ are mostly concentrated in the upper troposphere, except in the high latitudes. There are increases in the upper troposphere in the subtropics, but decreases in the midlatitudes. There are large deceases in $\overline{e}$ in the Arctic near surface. In the Southern Hemisphere the decrease in $\overline{e}$ extends over the depth of the troposphere. The change in θ_e is a broad tropospheric warming with larger increases in the deep tropics and the Arctic. There are increases in s in the deep tropics and the tropics. In the Arctic, s decreases near the surface but increases in the midtroposphere.

The differences between streamfunctions are show in figure 3.13. Similarly to the climatological streamfunction, the perturbations are much stronger in ψ_E than in ψ_M. The ψ_M perturbations are limited to the tropics, reflecting a shift of the Hadley cell (the cell decreases at relatively low θ_e values and increases at relatively high θ_e values). Although the Hadley cell makes up a relatively small fraction of the total streamfunction, the relative changes in the Hadley cell are of similar magnitude to the strength of the Hadley cell in the control circulation, reflecting that the shift of the Hadley cell to higher θ_e values. The location of the outer edge of the Hadley cell is controlled by $\overline{v}$ in both pressure and θ_e

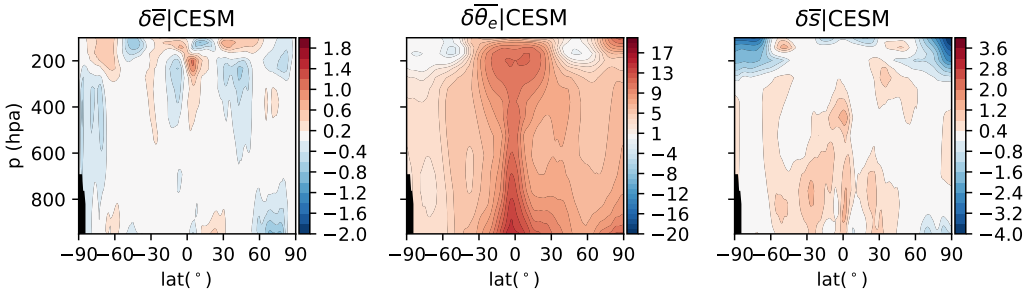

Figure 3.12: The response of $\overline{e}$,$\overline{\theta_e}$, and s for RCP8.5 forcing for 2071-2080, with respect to historical forcing for 1990-2004, from the CESM LENS experiment.

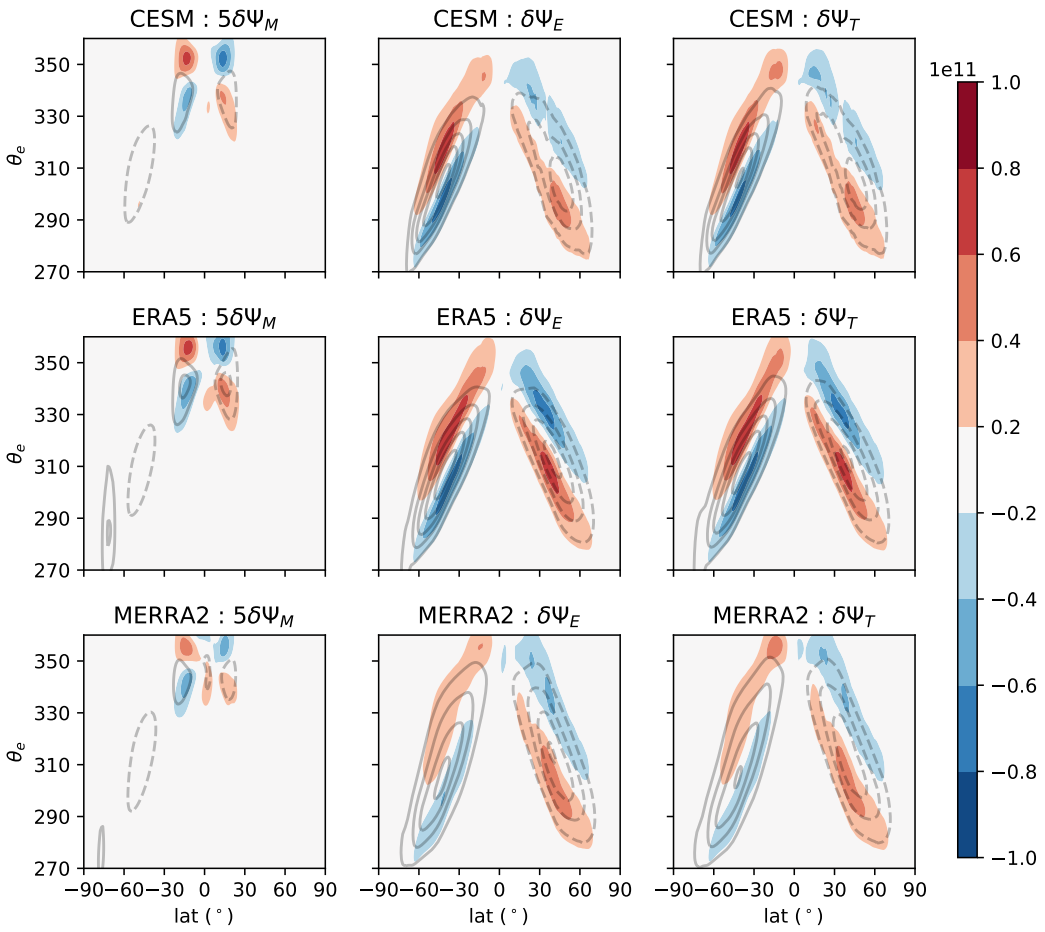

Figure 3.13: As for 3.10, but for the streamfunctions calculated using the different control climates with the CESM perturbations. Filled contours: difference between the perturbed and control streamfunction; contours: control streamfunction. The scale between figures is the same to accommodate a direct comparison between the two.

space, and so using ψ_M to study tropical expansion yields the same results as using $\overline{v}$. The agreement between the different datasets on the edge of the Hadley circulation reflects the agreement of $\overline{v}$ shown in figure 3.9.

Many features of $\delta\psi_E$ are common across all of the different data sets. The largest changes to the streamfunction are in ψ_E in the midlatitudes. The overall change is best interpreted as an upward shift of the global cell. In the tropics the increases of ψ_M and ψ_E happen at approximately the same θ_e value. Over the Arctic there is a decrease of ψ_E.

There are some differences in $\delta\psi_E$ between the different data sets; the perturbations applied to the CESM background state are relatively less effective at perturbing the circulation in the subtropics. In the Southern Hemisphere the perturbations applied to the MERRA2 data set are less effective than when they are applied to the other data sets.

To decompose the differences in the perturbations of ψ_E we apply the linearization procedure, equation (3.2), shown in figure 3.14. The difference between using the linearization procedure and using the functional derivatives explicitly is not visible on the contouring intervals we have used here, so we can use the functional derivatives to interpret the results of the linearization procedure. Qualitatively the results of the linearization match our expectations from the STEM functional derivatives. $\delta_{\overline{e}}\psi_E$ shows almost vertically uniform changes in the intensity of the streamfunction, without changing the range of θ_e values that it operates over. The perturbation from $\overline{\theta_e}$, $\delta_{\overline{\theta_e}}\psi_E$ shows an upwards shift of the streamfunction around the mean $\overline{\theta_e}$ values, so the broad warming and moistening of the atmosphere shifts ψ_E to larger θ_e values. The shift is lower in the tropics than the extratropics however, even though $\delta\overline{\theta_e}$ is largest in the tropics. $\delta_s\psi_E$ shows a widening of the streamfunction, corresponding to an increase in s in the tropics and subtropics. Similar to $\delta_{\overline{\theta_e}}\psi_E$ it is largest in the midlatitudes, even though δs is largest in the tropics.

The largest changes in ψ_E come from $\delta_{\overline{\theta_e}}$. This is not unsurprising because the pattern of $\overline{\psi}_E$ matches the upward shift that we would expect from the kernels. Also, $\delta\overline{\theta_e}$ is much larger than either $\delta\overline{e}$ or δs. However, as shown in Subsection 3.3.1, $\delta_{\overline{\theta_e}}\psi_E$ does not contribute to the change in H_E. This is an important feature of this linearization; it distinguishes the changes in ψ_E which change H_E from the much larger change in $\delta_{\overline{\theta_e}}\psi_E$. There are small differences in $\delta_{\overline{\theta_e}}\psi_E$ between the different data sets; most notably there is less of perturbation to the ψ_E in the northern hemisphere using MERRA2 as the control. The $\delta_{\overline{\theta_e}}$ term is the most important term for all of the data sets. These results are consistent with the results of Wu and Pauluis (2013), who find that $\delta_{\overline{\theta_e}}\psi_E$ is the largest term in a CO_2 doubling experiment.

The changes from the eddy mass flux $\delta_{\overline{e}}\psi_E$ causes a decrease in ψ_E in the Northern Hemisphere midlatitudes and high latitudes. Similar results are found by Laliberté and Pauluis (2010), who found

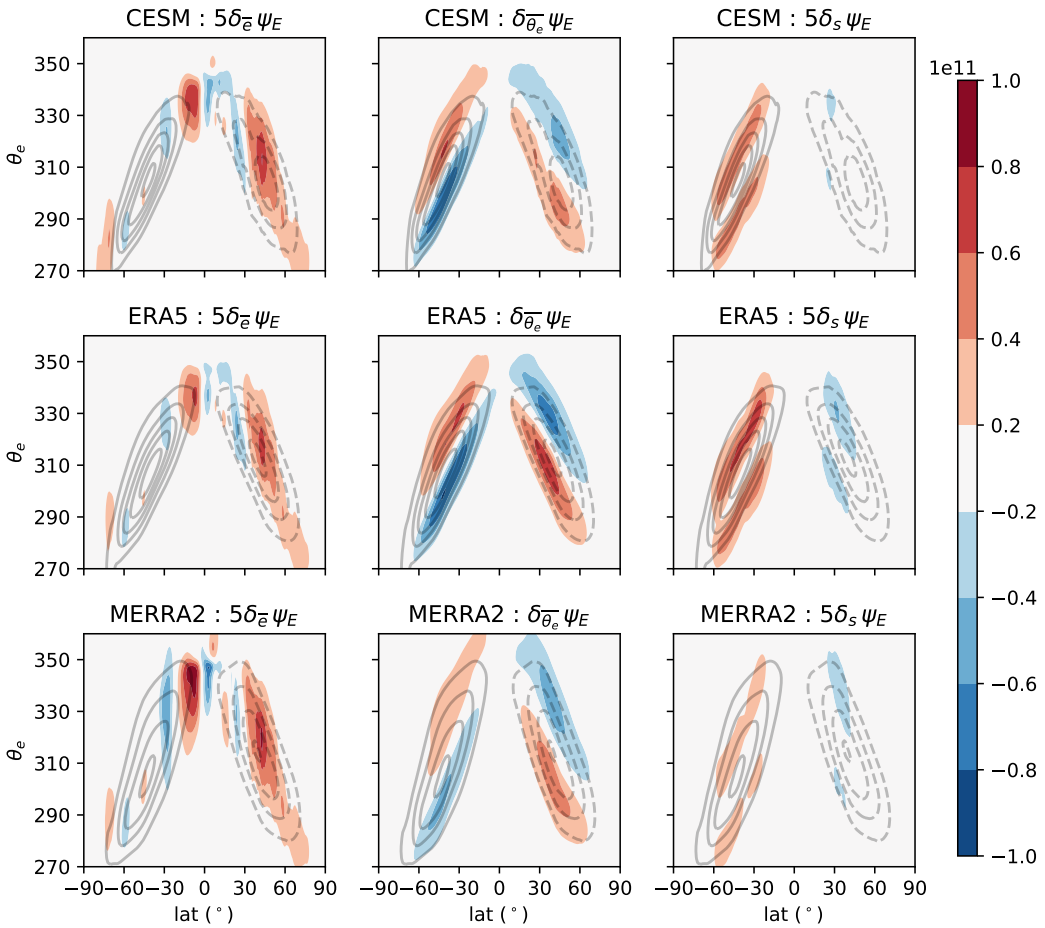

Figure 3.14: Filled contours: the linearization of the STEM eddy streamfunction using the three input variables and the three different climatologies; contours: the control ψ_E from each of the three different climatologies.

that there is a decrease in the total mass flux associated with the Northern Hemisphere winter storm track. Since the sensitivity factor for $\overline{e}$ is 1, the differences in $\delta_{\overline{e}}\psi_E$ between different data sets is due to the differences in how perturbations from a single grid cell are projected into θ_e space. Differences in θ_e and s between data sets control these projections, and a data set with higher s will project $\delta_{\overline{e}}\psi_E$ onto a larger range of values. This is particularly visible in the Southern Hemisphere tropics and subtropics, where $\delta_e\psi_E$ is spread across a wider range of θ_e values for the MERRA2 data set than the other data sets.

The changes from the variability of θ_e, $\delta_s\psi_E$, mostly increase the width of the cell in the Southern Hemisphere, although the perturbations have less of an effect on ψ_E taken from the MERRA2 data set. The response in the Northern Hemisphere is not very robust across data sets: the $\delta_s\psi_E$ from CESM exhibits almost no change, $\delta_s\psi_E$ from ERA5 has a small widening in the subtropics, and $\delta_s\psi_E$ from MERRA2 shows only a small widening in one branch of the cell.

The perturbation $\delta_{\overline{\theta_e}}\psi_E$ can be written as a convolution using the functional derivative.

$$\delta_{\overline{\theta_e}}\psi_E = -L_x \int \overline{e}/s \left(\left[\frac{\theta_e - \overline{\theta_e}}{s} \right] 1/\sqrt{2\pi} \exp\left[-1/2 \left(\theta_e - \overline{\theta_e} \right)^2 / s^2 \right] \right) \delta\overline{\theta_e} dp/-g \tag{3.40}$$

The sensitivity factor, $\overline{e}/s$, and $\delta\overline{\theta_e}$ are functions of latitude and p only. If $\overline{e}/s$ and $\delta\overline{\theta_e}$ have their maxima at the same vertical level, then $\delta_{\overline{\theta_e}}\psi_E$ will be large, but if $\delta\overline{\theta_e}$ is large where $\overline{e}/s$ is small then $\delta_{\overline{\theta_e}}\psi_E$ will also be small. A similar expression for $\delta_s\psi_E$ can also be formed. For $\delta_{\overline{e}}\psi_E$ the sensitivity factor is unity, so a similar expression is not needed.

To understand the differences in the response of ψ_E using the different data sets we consider how the sensitivity factor $\overline{e}/s$ combines with the $\delta\overline{\theta_e}$ and δs. This is shown in figure 3.15. The sensitivity factors of the functional derivative are computed from all three of the input data sets, and then are multiplied by the CESM perturbations, $\delta\overline{\theta_e}$ and δs. The sensitivity factors are most different for MERRA2 in the southern hemisphere compared to the other data sets because of the high s values in the midlatitude midtroposphere in MERRA2. The effect of this is that MERRA2 has very little sensitivity in the midlatitude midtroposphere. The broad changes in $\overline{\theta_e}$ in the midtroposphere have no effect on the streamfunction because the atmosphere has no sensitivity there. By contrast, CESM and ERA5 have relatively high sensitivity factors throughout the southern hemisphere midtroposphere, and so are much more sensitive to the broad pattern of $\delta\overline{\theta_e}$. In the Southern Hemisphere the broad extension of δs into the midtropopshere overlaps with the broad sensitivity factors in the midlatitudes.

In the tropics $\delta\overline{\theta_e}$ and δs are both relatively large compared to the extratropics, but they are not effective in changing ψ_E. This is because $\overline{e}$ is very weak in the tropics. Even though there are large

perturbations, the eddy transport is weak, so they have very little effect on ψ_E. The sensitivity factors for $\delta_s\psi_M$, $\overline{v}/s$ (not shown) also does not line up very well with δs, so that the δs in the tropics also does not perturb ψ_M. The broad changes in $\overline{\theta_e}$ overlap with the high sensitivity factors at both the top and the bottom of the Hadley cell, This is what is responsible for creating the upwards shift in ψ_M seen in figure 3.13.

3.6 Summary and Discussion

The STEM streamfunction parametrizes the circulation in terms of first and second order statistics that are averaged in pressure space. This functional dependence can be exploited to analytically calculate the functional derivatives of the STEM, which project the perturbations in the STEM input variables at a single pressure-latitude point into θ_e space. Control values of the STEM input variables were calculated for one comprehensive climate model in the modern era and a projected future decade and two different reanalysis data sets. By combining the changes in the input variables from the climate model with the climatologies from the different data sets we found the differences in the sensitivities of the different data sets. The key points of this Chapter are summarized below.

1. Perturbations in $\overline{v}$ and $\overline{e}$ change the strength of the circulation, perturbations in $\overline{\theta_e}$ shift the streamfunction to a different range of θ_e values, and changes in s strengthen or weaken the streamfunction at extreme values of θ_e. For ψ_M this is a consequence of $\overline{v}$ changing sign in the atmosphere.

2. The sensitivity of the moist isentropic circulation to zonal mean changes in the position of θ_e surfaces, or the variability in θ_e surfaces is inversely proportional to the variability in the θ_e surfaces. This means that data sets with high moist thermodynamical variability will have weaker responses of the moist isentropic circulation to climate perturbations.

3. There is higher variability of the moist isentropic surfaces, s, in MERRA2. This makes the background circulation represented by MERRA2 less sensitive to climate perturbations.

4. The projected response of the streamfunction are dominated by changes in $\overline{\theta_e}$. Thus, to first order, the response of the moist isentropic circulation can be approximated as a thermodynamic response with fixed dynamics.

5. The broad changes in $\overline{\theta_e}$ and s are localized by the strength factor $\overline{e}/s$ into the midlatitudes, so that only some regions of the atmosphere are sensitive to climate perturbations.

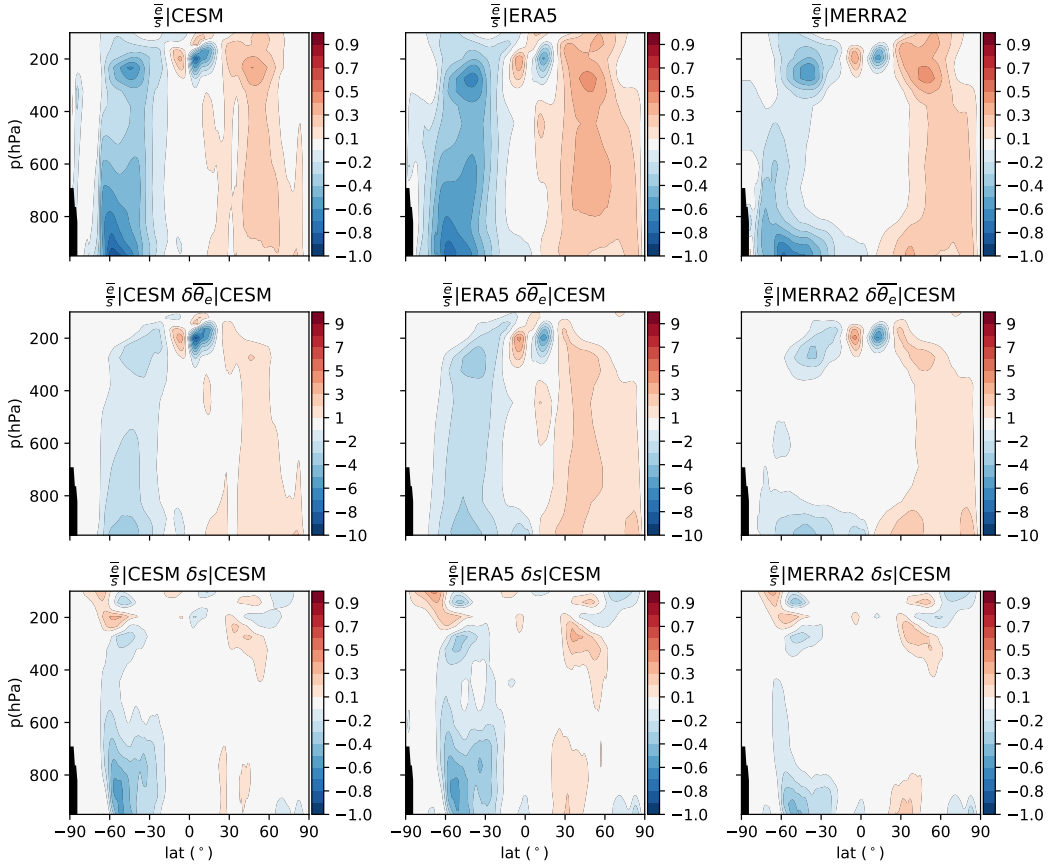

Figure 3.15: Top row: The sensitivity factors taken from the three different datasets; middle row: the sensitivity factor from each of the three datasets multiplied by $\delta\overline{\theta_e}$ from CESM; bottom row: the sensitivity factor from each of the three datasets multiplied by δs. Note that the colour bar for the middle row is 10 times larger than the other rows (reflecting the relatively large magnitude of $\delta\overline{\theta_e}$.

6. The changes in the Northern Hemisphere storm tracks are mostly a reduction in ψ_E caused by a decreased eddy mass flux, while the changes in the Southern Hemisphere storm tracks are an increase in the eddy heat flux caused by an increase in s.

The results of this Chapter demonstrate that the STEM circulation has three separate responses to climate change: a shift of the circulation to higher or lower θ_e values, a change in the strength of the circulation, and a change in the range of θ_e values that the circulation extends over. The qualitative nature of these results are independent of the model and perturbation considered (with some small caveats, discussed later), so that the results from any experiment can be decomposed and analyzed using this method. Importantly, the shift of the streamfunction does not contribute much to the global heat transport, since the changes are relatively uniform in height, similar to the results shown in Chapter 2. This is because the shifts in the streamfunctions do not change the total strength of the circulation. However, these shifts locally represent greatest magnitude responses compared to the other terms. Using the linearization procedure is useful to find the changes in the moist isentropic circulation that are related to the changes in the total heat flux.

The fact that the sensitivity factors vary inversely to the standard deviation of θ_e is an important conclusion; models that have higher variability will have a less sensitive overturning circulation in θ_e coordinates. This result was previously unknown before the analysis conducted in this Chapter. While the total diabatic heating rate constrains the total heat transport in the atmosphere, it does not determine the decomposition of the transport between different dynamical mechanisms. A model that has a high $\overline{e}$ but a low s will have higher sensitivity to perturbations than a model with high s but low $\overline{e}$, even if it has the same heat flux. This implies that using a single climate model to study this decomposition might not lead to robust results, since it is dependent on the background climatology.

From the evidence presented here it is not possible to determine how accurate the projections of the moist isentropic circulation from CESM are because of the large differences between the two reanalysis products. In particular the large difference in the standard deviation of θ_e between the two reanalysis products leads to diverging answers about the sensitivity of the moist isentropic circulation. A model with a variability closer to that of MERRA2 will have a very different response to climate perturbations than a model that has a variability closer to ERA5. In order to determine which response is correct the modern day circulation, particularly s would need to be better constrained.

Laliberté and Pauluis (2010) studied the response of H_E, $\mathcal{M}_E$, and Δ_E in an ensemble of comprehensive climate models, and found that there was a wide range of simulated values. A followup study to analyze the spread of the standard deviation of θ_e in a similar set of climate models, to see whether

it could explain the differences in heat transport, is warranted, based on the differences between the reanalysis products documented here.

Consistently throughout this Section we have made assumptions about the atmosphere that are valid for modern day, Earth-like conditions: $\overline{v}$ changes sign once in the troposphere (to interpret ψ_M) and the vertical stratification of θ_e is relatively weak (so that the spread in ψ can be related mostly to s). If $\overline{v}$ change signs multiple times in the atmosphere, or the stratification were much stronger, then the analysis in this Chapter would need to be revisited. The assumption about stratification may need to be revisted if the STEM were applied to exoplanets or radically different paleoclimates, like a hard snowball earth, where moisture plays a much smaller role in the global circulation (Pierrehumbert, 2002). Still, for modern and expected end of century climate change projections, these assumptions will remain valid and the STEM sensitivity will be a useful tool for understanding the sensitivity of the circulation in θ_e coordinates.

A future study that took advantage of multiple climate models run using the same experimental protocol would be an important extension of the research done here. This would allow a more apples-to-apples comparison, and help determine what features of the response are independent of the control circulation. At the present moment, climate do not report the statistics required to compute the STEM, but if high frequency data is output, then the zonal mean statistics can still be calculated.

Appendix A: Dynamical Stability and The Eddy Mass Flux

Here we describe the dynamic stability and how to calculate $\mathcal{M}_E$ and Δ_E from ψ. For a steady circulation the net heat transport can be written as

$$H_M = \Delta_p \mathcal{M}_M \tag{3.41}$$

where Δ_P is the gross moist stability, i.e. the difference in $\overline{\theta_e}$ between the bottom and top of the troposphere, and $\mathcal{M}_M$ is the mass flux of the circulation (e.g. Neelin and Held, 1987). For the Hadley circulation, $\mathcal{M}_M$ is the circulation in either the upper or lower branch (which must be equal for mass conservation), and Δ_P is the difference in $\overline{\theta_e}$ between the two branches.

The goal of the dynamic stratification (as presented here) is to find an equivalent definition to the gross moist stability for the eddies. Using the circulation in θ_e coordinates provides a straightforward way to do this. Since the circulation is composed of a poleward and equatorward branch we can find the mean θ_e in both of these branches and use it to define the stability in θ_e coordinates. First we calculate

the mass flux in the poleward branch of the circulation:

$$\mathcal{M}_E = \int_0^\infty M_E(\phi, \theta_e) I\left(M_E\right) d\theta_e \tag{3.42}$$

where $I(x)$ is 1 when x is greater than 0 and 0 otherwise. For the eddy circulation to conserve mass at every latitude, $\mathcal{M}_E$ must be equal and opposite in the poleward and equatorward branches.

The mass flux weighted average θ_e in the upper branch is

$$\theta_e^+ = \left(\mathcal{M}_E\right)^{-1} \int_0^\infty M_E(\phi, \theta_e)\theta_e I(M_E) d\theta_e \tag{3.43}$$

and after a similar calculation in the equatorward branch we define the dynamic stratification in θ_e coordinates as

$$\Delta_E = \theta_e^+ - \theta_e^-. \tag{3.44}$$

Since the heat flux in the poleward branch is $\mathcal{M}_\mathcal{E}\theta_e^+$ and in the equatorward branch is $\mathcal{M}_E\theta_e^-$, the net heat transport is

$$H_E = \Delta_E \mathcal{M}_E, \tag{3.45}$$

as in equation (3.38).

The mass flux in the either branch is also related to the maximum value of ψ, assuming that M_E only changes signs once in the atmosphere, which is true of the circulation in θ_e space. The extremum of ψ_E must occur where M_E switches signs, by the extreme value theorem, and since M_E only changes sign once, this will occur at the average θ_e value, $\langle\theta_e\rangle = 1/2\left(\theta_e^+ + \theta_e^-\right)$. In the northern hemisphere, ψ_E is negative, and so

$$min(\psi_E) = \int_{\langle\theta_e\rangle}^\infty M_E d\theta_e,$$

and since (in the northern hemisphere) M_E is only positive for $\theta_e > \langle\theta_e\rangle$, then

$$\begin{aligned} min(\psi_E) = &\int_{\langle\theta_e\rangle}^\infty M_E I\left(M_E\right) d\theta_e \\ = &\int_0^\infty M_E(\phi, \theta_e) I\left(M_E\right) d\theta_e \end{aligned}$$

which is the expression for $\mathcal{M}_E$ above. This is the expression used in Pauluis et al. (2010), amongst others.

Chapter 4

Using "Heat Tags" to Understand the Remote Influence of Atmospheric Diabatic Heating

4.1 Introduction

How do we assess the remote effects of diabatic processes on the atmosphere's heat content and thermal structure? Diabatic heating must be locally balanced by transport in the climatological mean (Peixoto and Oort, 1992), but this does not provide information about remote diabatic heating. For example, latent heating from condensation in the tropics is balanced by an export of heat out of the tropics, while radiative cooling at higher latitudes is balanced by an import of heat into the region. However, these balances do not relate the low and high latitudes since local thermodynamic balances do not provide direct insight into thermodynamics processes in remote regions that are linked through transport of air masses.

Those air masses warmed by tropical convection and midlatitude storm-tracks condensation are ultimately cooled by longwave emission spread throughout the troposphere (Peixoto and Oort, 1992; Ling and Zhang, 2013; Zhang et al., 2017), implying transport of air masses from the regions of heating to the regions of cooling. However, more information is required to determine which air masses contribute to the thermal structure of the atmosphere. For instance, we can ask if air warmed by condensation in the Hadley cell travels rapidly enough to reach the poles without significant cooling. To understand the

ultimate fate of the heat in an air mass we need to keep track of which processes warmed the air mass and the history of that air mass as it undergoes transport far from its region of generation.

Our goal in this study is to quantify the contributions from different sources of diabatic heating on the thermal structure of the atmosphere in the presence of long-range transport. We do this by using a set of tracers, referred to as 'heat tags', that serve to decompose the potential temperature field into separate contributions from different sources of diabatic heating. The heat tags are added whenever the atmosphere is heated, removed whenever the atmosphere is cooled, and otherwise transported with the potential temperature field. As a result, heat tags encode local generation information and remote connections involving material transport. The method is global rather than local, Eulerian rather than parcel based, and allows for a complete decomposition (the potential temperature can be written as a sum of the tracers). The heat tag equations are constructed to retain positive and finite values for extended climate simulations.

Several previous studies have constructed Green's functions to study atmospheric transport from surface sources (e.g. Holzer, 1999; Orbe et al., 2013, 2015a), or from the tropopause (Orbe et al., 2013; Waugh and Hall, 2002). The Green's function method can also be used to analyse the timescale of the transport (Waugh and Hall, 2002; Holzer and Hall, 2008; Orbe et al., 2016). Such "boundary layer propagators" methods transport tracers, subject to boundary conditions, typically with linear sources or sinks (for example the proportional loss functions in Orbe et al., 2016). For instance, Orbe et al. (2015a) analyzed the location of last boundary layer contact of air parcels in the Arctic troposphere, and find that only air masses in the lower part of column have origins in the Arctic. These methods are useful for problems that involve transport from a specified boundary surface and (mostly) conservative transport through the bulk of the domain. For the problem of tracking potential temperature in the atmosphere this poses a challenge, however, since the diabatic heating and cooling is spread throughout the atmosphere. This means that if Green's functions are used they need to be added and removed throughout the domain, instead of being simply included at a boundary. This poses a computational problem, since all the Green's functions would need to be stored. Instead of using Green's functions, we solve tracer equations with sources and sinks that evolve in time and space along with the atmospheric flow. This eliminates explicit information about transit time, but instead of having to store an entire age spectrum of Green's functions we only have to store a single tracer for each tagged process.

The method presented here is inspired in part by studies of water tagging (Sodemann et al., 2009; Singh et al., 2016; Dyer et al., 2017), tracers of last saturation humidity (Galewsky et al., 2005), or the tagging of carbon monoxide and ozone (Wang et al., 2011; Fisher et al., 2017), but generalizes the methods to work with sources and sinks that are not sign definite and without linearising any terms.

Martínez-Alvarado and Plant (2014) use a system similar to the one presented here, but with both positive tags for heat sources and negative tags for heat sinks. Although this has some advantages for initial value problems such as the weather forecast simulations that are considered in that study, their tag system would not remain finite in a long-term climate simulation. Our method overcomes this limitation by splitting the heating and cooling tendencies and treating cooling as a sink acting proportionally to all heat tags present (Section 4.2), but at the cost of having to solve non-linear equations.

A complementary approach to that presented here is to use Lagrangian tracking of parcels undergoing heating and cooling as they pass through atmospheric blocks (e.g. Pfahl et al., 2015) or other circulation features. This requires tracking of a given feature and, unless a code is instrumented diagnostically, an offline tool to be developed that uses frequent snapshots. In the method we present, the heat tags constitute an additional set of tracers (four in the present study) that are integrated consistently with the numerical methods used with other tracers like water vapor or chemical constituents, and thus are relatively easy to add to an already developed general circulation model (GCM). We use an idealized moist model to provide an initial demonstration of the implementation and analysis of heat tags in a setting relevant to climate science. In particular, we use the idealized aquaplanet first developed by Frierson et al. (2006), and later by O'Gorman and Schneider (2008); Vallis et al. (2018). The numerical methods and physical parameterizations used by the model also simplifies the implementation of the heat tags for reasons that will be detailed in Section 4.2.

The remainder of this chapter is structured as follows. In Section 4.2, we describe the method of tracer tagging, and then apply it to the potential temperature in the idealized model to generate the equations for the heat tags. In Section 4.3, the mean state of the heat tags is reported and discussed. In Section 4.4, the variability of the heat tags and interrelationships between them are analyzed. The heat tag framework leads to new results on poleward heat transport of dry and moist static energy that are discussed in Section 4.5. We then consider the mean and transport response of the heat tags in a CO_2 doubling experiment in Section 4.6. In Section 4.7, the key conclusions of the paper are summarized and future research directions are discussed in Section 4.8.

4.2 Methods

4.2.1 Tracer Tagging

For a hydrostatic atmosphere in pressure coordinates, the conservation equation for a tracer c is

$$\frac{\partial c}{\partial t} = -\nabla \cdot (\underline{v} c) + D_H(c) + \sum_{i=1}^{N_S} S_i, \tag{4.1}$$

where $\underline{v} = (u, v, \omega)$ is the non-divergent fluid pressure-coordinate velocity satisfying $\nabla \cdot \underline{v} = 0$ and $S_i = \{S_1, \ldots, S_{N_S}\}$ represents a set of N_S source and sinks of c. The term $D_H(c)$ represents horizontal diffusive flux of c. This represents a linear operation on c; in this work it is considered to reflect numerical constraints and is not a focus for physical analysis. *Tracer tagging* decomposes the tracer c into a system of N_S *tags*, $\{c_1, \ldots, c_{N_S}\}$ satisfying conservation of total field c at each point in space and time by locally constraining the tendency to conserve the total $\partial c/\partial t$

$$\sum_{i}^{N_S} \frac{\partial c_i}{\partial t} = \frac{\partial c}{\partial t} \tag{4.2}$$

and by identifying a time t_0 for which $\sum_{i=1}^{N_S} c_i(t_0) = c$ at each spatial point.

We wish to constrain c_i to be positive semi-definite:

$$c_i \geq 0, \ i = 1, \ldots, N_S. \tag{4.3}$$

This constraint will be violated by the simple decomposition of (4.1)

$$\frac{\partial c_i}{\partial t} = -\nabla \cdot (\underline{v} c_i) + D_H(c_i) + S_i, \ i = 1, \ldots, N_S \tag{4.4}$$

in which each tag c_i has a corresponding source or sink S_i, and for which sink processes will tend to generate negative c_i while conserving the total $c = \sum_{i=1}^{N_S} c_i$. Martínez-Alvarado and Plant (2014) used such a system to track sources and sinks of potential temperature in short-term weather forecasts. In the context of climate analysis, however, such a system leads to non-stationary behavior in the tags. For example, if $S = S_0 + S_1$ where S_0 is positive everywhere and S_1 is negative everywhere [e.g. if c represents potential temperature, S_0 could represent latent heating and S_1 longwave cooling, analogously to Martínez-Alvarado and Plant (2014)], c_0 and c_1 would diverge to positive and negative infinite values even while conserving the total c.

To guarantee (4.3), we first decompose S_i at each spatial and temporal point into positive sources

and negative sinks:

$$S_i = S_i^+ + S_i^-, \text{ where} \tag{4.5}$$

$$S_i^+ = I(S_i)S_i \text{ and} \tag{4.6}$$

$$S_i^- = I(-S_i)S_i, \tag{4.7}$$

for $i = 1 \ldots, N_S$. In (4.6)-(4.7), I is the Heaviside function, which is 1 for a positive argument and 0 otherwise. Thus, S_i^+ represents the positive source of S_i and S_i^- represents the negative sink of S_i.

If we wish to track different sources of c in the atmosphere, then it makes sense to have each tag c_i correspond to each S_i^+, which we will use as a source for that tag. To create the sink for the tag we will assume that the tags in any given air parcel are well mixed, and that the total tracer sink,

$$S^- = \sum_{i=1}^{N_S} S_i^-, \tag{4.8}$$

does not act to preferentially remove any given tracer tag. Under these assumptions, the sink term for c_i can be written as

$$S_i^- := \frac{c_i}{c} S^- = \chi_i S^-, \text{ where } \chi_i := \frac{c_i}{c} \tag{4.9}$$

is a *tag fraction* for tag i. In other words, the sink removes different tags proportionally to their amount inside the parcel. Putting together these considerations gives the system of tracer tags

$$\frac{\partial c_i}{\partial t} = -\nabla \cdot (\underline{v} c_i) + D_H(c_i) + S_i^+ + \chi_i S^-, \; i = 1, \ldots, N_S, \tag{4.10}$$

where the S_i^+ are defined by (4.5)–(4.6) and where we have used (4.9). The c_i are initialized at t_0 to have a positive value and satisfy

$$c(t_0) = \sum_{i=1}^{N_S} c_i(t_0); \tag{4.11}$$

initialization of the tracer tags is discussed further below. It is easily shown that (4.10) satisfies (4.2).

The tag fractions $\{\chi_i\}$ defined in (4.9) sum to unity

$$\sum_{i=1}^{N_S} \chi_i = 1. \tag{4.12}$$

Their evolution equations can be obtained by first recognizing that

$$\frac{\partial(\cdot)}{\partial t} + \nabla \cdot (\underline{v}\cdot) + D_H(\cdot)$$

is a linear differential operator on its argument (for non-divergent pressure-coordinate $\underline{v}$). Taking c^{-1} times (4.10) and subtracting $\chi_i c^{-1}$ times (4.1) then yields

$$\frac{\partial \chi_i}{\partial t} = -\nabla \cdot (\underline{v}\chi_i) + D_H(\chi_i) + (1-\chi_i)\,\frac{S_i^+}{c} - \chi_i \sum_{j\neq i} \frac{S_j^+}{c}. \tag{4.13}$$

Note that the sink terms S_i^- does not explicitly appear in this equation, which demonstrates the trade-offs between the relative fraction of the tags: although S_i^- do not decrease χ_i, sources of other tags, ($\{S_j^+\}_{j\neq i}$), will act to decrease χ_i to guarantee (4.12). This observation will prove useful in understanding the distribution of heat tag fractions in Section 4.3.

Equation (4.13) demonstrates that if the tracer field c is positive, the tag fractions c_i are also positive because $(1-\chi_i)\,\frac{S_i^+}{c}$ will not increase χ_i above 1, and $-\chi_i \sum_{j\neq i} \frac{S_j^+}{c}$ will not decrease χ_i below 0, so $0 \leq \chi_i \leq 1$. Since $c_i = \chi_i c$, then $0 \leq \chi_i \leq 1$.

Lastly, since the $\{c_i\}$ are positive and, via (4.2) and (4.11), sum to c for all time, they remain bounded by the greatest value of c. This ensures that the system will not diverge even under long time integration.

4.2.2 Numerical implementation in an idealized moist general circulation model

We use the implementation of the class of idealized moist general circulation model developed in Frierson et al. (2006); Frierson (2007); O'Gorman and Schneider (2008) that is found in the Isca framework (Vallis et al., 2018). This model, coded with the NOAA GFDL Flexible Modeling System, solves the moist hydrostatic primitive equations on the sphere using a pseudospectral method. The Isca framework provides a set of standard physical parameterizations, including updated radiative transfer schemes. The horizontal resolution of the spectral core is T85 and in the vertical there are 30 levels evenly spaced in the model's sigma coordinate. A fourth order hyperviscosity with a base coefficient of 0.1 days^{-1} that is applied to the highest resolved wavenumber is used. The atmosphere is situated above a global slab ocean with a depth of 100 m. The model is run with annual average insolation and without a diurnal cycle. The boundary conditions and boundary forcing are zonally homogeneous and hemispherically symmetric about the equator. The long-term statistics are expected to respect these related symmetries such as hemispheric symmetry and no stationary waves.

Potential temperature and tracers, including water vapor, are advected using the model's standard spectral advection scheme. For water vapor solely, a hole-filling scheme is used to preserve non-negativity. Although a spectral advection scheme does not guarantee non-negativity (Rasch and Williamson, 1990), negative values were mitigated by reducing the time step of the model to 150s for both the dynamics and physical parameterizations.

Of the various combinations of subgrid scale physical parameterizations and radiative transfer available within the Isca framework, we select the following:

1. A two-stream, two-plus-one band, grey radiation scheme, described in Section 4.2 of Vallis et al. (2018). The scheme parameterizes the optical depth in terms of a nominal CO_2 concentration value and of the water vapor field simualted by the model. It includes a shortwave window, a longwave band that treats the infrared window region of the spectrum, and another longwave band that treats the rest of the spectrum. The radiative scheme used in our version of the model has a nominal CO_2 value of 360ppm (documented in Section 4.2 in Vallis et al. (2018)). In Section 4.6, this value is doubled to explore the response to climate change.

2. A vertical diffusion that parameterizes turbulent boundary layer fluxes using simplified Monin-Obhukov similarity theory (Frierson et al., 2006). The effect of this parameterization is to spread the surface fluxes of enthalpy, moisture and momentum over the model planetary boundary layer. This parameterization also accounts for the surface fluxes of heat, moisture, and momentum.

3. A large-scale condensation scheme that removes water vapour and adds latent heat to a grid cell if the grid cell reaches saturation. The water vapour is assumed to be immediately removed from the atmosphere without allowing for re-evaporation. This is different from Frierson et al. (2006), but is the same formulation that was used in O'Gorman and Schneider (2008).

4. A subgrid scale convection scheme that is the 'shallower' option documented in Frierson (2007). The convection scheme checks if there is convective available potential energy in a column, and, if there is, relaxes the column towards a moist adiabatic profile in a manner that conserves total column enthalpy.

The tracer tagged here is potential temperature, θ, which evolves according to

$$\frac{\partial \theta}{\partial t} = -\nabla \cdot (\underline{v}\theta) + D_H(\theta) + \Pi Q, \tag{4.14}$$

where the Exner function $\Pi = \left(\frac{p_0}{p}\right)^{\kappa}$ and Q represents the sum of the model's parameterized heating

rates. We use equation (4.10) as follows: we identify θ with c, set $N_S = 4$ tags

$$\theta = \sum_{i=1}^{N_S} \theta_i = \theta_{conv} + \theta_{cond} + \theta_{diff} + \theta_{radi}, \tag{4.15}$$

and split the heating terms into θ sources and sinks

$$\Pi Q = \Pi Q^+ + \Pi Q^-, \tag{4.16}$$

with

$$\Pi Q^+ = \Pi Q^+_{conv} + \Pi Q^+_{cond} + \Pi Q^+_{diff} + \Pi Q^+_{radi} \tag{4.17}$$

and

$$\Pi Q^- = \Pi Q^-_{conv} + \Pi Q^-_{diff} + \Pi Q^-_{radi}. \tag{4.18}$$

Here, the subscripts *conv, cond, diff, radi* indicate, respectively, heating from the subgrid scale convection scheme, the large-scale condensation, the vertical diffusion in the boundary layer parameterization, and the shortwave and longwave radiative transfer schemes. Note the absence of Q^-_{cond} in (4.18). This is zero by design, because the model precipitation scheme has no re-evaporation of falling water vapour (cooling and hence a θ sink). Applying equation (4.10) to θ yields a set of tracers that evolve according to

$$\frac{\partial \theta_{conv}}{\partial t} = -\nabla \cdot (\underline{v}\theta_{conv}) + D_H(\theta_{conv}) + \Pi \left(Q^+_{conv} + \frac{\theta_{conv}}{\theta} Q^- \right) \tag{4.19a}$$

$$\frac{\partial \theta_{cond}}{\partial t} = -\nabla \cdot (\underline{v}\theta_{cond}) + D_H(\theta_{cond}) + \Pi \left(Q^+_{cond} + \frac{\theta_{cond}}{\theta} Q^- \right) \tag{4.19b}$$

$$\frac{\partial \theta_{diff}}{\partial t} = -\nabla \cdot (\underline{v}\theta_{diff}) + D_H(\theta_{diff}) + \Pi \left(Q^+_{diff} + \frac{\theta_{diff}}{\theta} Q^- \right) \tag{4.19c}$$

$$\frac{\partial \theta_{radi}}{\partial t} = -\nabla \cdot (\underline{v}\theta_{radi}) + D_H(\theta_{radi}) + \Pi \left(Q^+_{radi} + \frac{\theta_{radi}}{\theta} Q^- \right). \tag{4.19d}$$

The source and sinks are separated at every grid point and time step in the model. For instance, in a convectively unstable column the convection scheme heats higher model levels, contributing locally to Q^+_{conv}, and cools lower model levels, contributing locally to Q^-_{conv} and hence to Q^- [in equations (4.18) and (4.19a)]. Apart from small numerical errors discussed in the next subsection, the tag sum should satisfy (4.15) at every time step and grid point.

For heat tag fractions

$$\chi_i = \frac{\theta_i}{\theta},\ i = 1, \ldots 4, \tag{4.20}$$

the corresponding evolution [see equation (4.13)] is,

$$\frac{\partial \chi_i}{\partial t} = -\nabla \cdot (\underline{v}\chi_i) + D_H(\chi_i) + (1 - \chi_i)\,\frac{\Pi Q_i^+}{\theta} - \chi_i \sum_{j \neq i} \frac{\Pi Q_j^+}{\theta}. \tag{4.21}$$

The model tagging procedure generates physical tendencies at every time step, separates them into their positive and negative parts, generates the tracer tendencies above, and then passes these to the tracer advection scheme. This numerical procedure is simplified for the idealized moist model, since it only has a single timestep for both the physics and dynamics. Subgrid scale vertical velocities are neglected since they are not explicitly calculated in the simple physical parameterizations used here. Adding, for example, convective mass flux based estimates of vertical velocity into the tag transport is left as future work.

We have tested the numerical procedure by ensuring that (4.15) is well satisfied at all points. The details of the test are given in Appendix A. Apart from a region in the upper stratosphere the errors are very small and can be ignored. We also describe the initialization procedure in Appendix B, and show how a judicious choice of initial tracer state can reduce the amount of time for the model to equilibrate. After statistical equilibrium is achieved, an additional 2500 d of simulation is used as an analysis period for all simulations presented here. Additionally, we carry out another model integration of the same length but with the CO_2 value doubled, which we refer to as 2xCO_2. The control simulation with CO_2 value of 360 ppm is referred to as the CLIM when it needs to be distinguished from the 2xCO_2 (Section 4.6).

The model climatology is represented in Figure 4.1. We denote by an overbar the time and zonal mean and by a prime the departure from this mean. The zonal mean, climatological mean equivalent potential temperature $\overline{\theta}_e$ (figure 4.1a) features moist adiabatic conditions in the tropics, marginally stable stratification in the mid-latitudes and stable stratification in the polar region. The corresponding climatological mean, potential temperature $\overline{\theta}$ (figure 4.1b) features strong vertical gradients in the tropical to midlatitude upper troposphere and increasing lower tropospheric vertical gradients towards the poles. The Eulerian-mean, zonal-mean streamfunction,

$$\overline{\psi} = 2\pi a \cos\phi \int \overline{v} \frac{dp}{g}, \tag{4.22}$$

(figure 4.1c) shows a simulated Hadley cell that is about twice the observed strength. As a measure

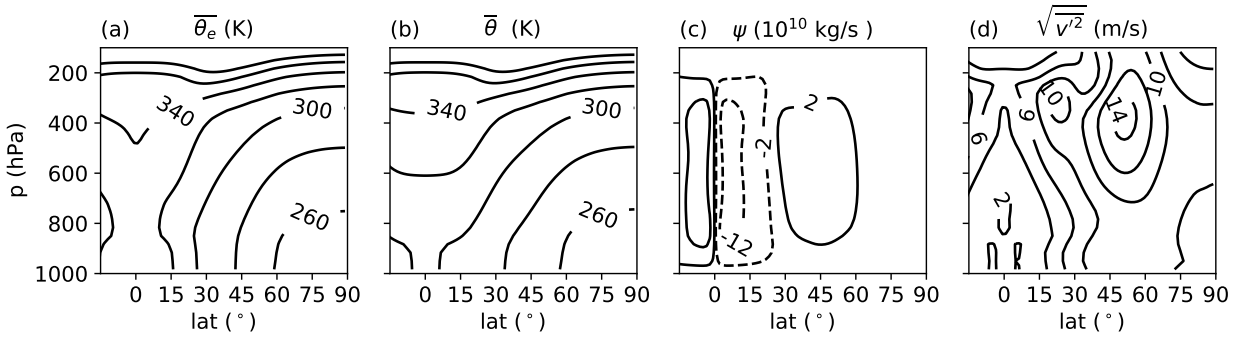

Figure 4.1: (a): The zonal mean climatological equivalent potential temperature θ_e (contour interval 10K). (b): As in (a), but for the potential temperature θ. (c): The Eulerian mean streamfunction $\overline{\psi}$ (contours are -12,-2,2, and 12 10^{10}kg/s). (d): As in a for the root mean square eddy meridional velocity $\sqrt{\overline{v'^2}}$ (contours are 2 $(\mathrm{m/s})^2$).

of the strength of the eddy variability [similar to Holzer and Boer (2001)] the root mean squared eddy meridional velocity, $\sqrt{\overline{v'^2}}$, where prime denotes a departure from a zonal mean (figure 4.1d) features a maximum in the extratropical upper troposphere that overlies the model eddy-driven jet (zonal mean wind not shown).

4.3 Climatology of the heat tags

The climatological distribution of tag sources for θ, $\{\Pi Q_i^+\}$, are shown in figures 4.2a-d and the climatological distribution of tag sinks for θ, $\{\Pi Q_i^-\}$, are shown in figures 4.2e-h. The distribution of convection and condensation sources (ΠQ_{conv}^+ and ΠQ_{cond}^+, figures 4.2a-b) shows the partitioning between large-scale and subgrid scale latent heating. In the tropical midtroposphere, most of the latent heating happens through the subgrid scale convective parameterization. There is a strong isolated maximum in condensation source in the tropical upper troposphere that is approximately half the maximum of the convection source. This reflects saturation of air that is explicitly resolved by the model, which occurs at the top of the Hadley cell's region of strong vertical ascent (figure 4.1a). A small amount of shallow convection heat tag source also extends into the subtropics and mid-latitudes. In the mid-latitudes, condensation becomes the dominant tag source of latent heating (figure 4.2b). In this region, regions of vertical ascent associated with baroclinic eddies create conditions for large-scale saturation. Cooling in the convective parameterization (ΠQ_{conv}^-) only occurs weakly in a location near the tropical surface (figure 4.2e), reflecting the rare occasions when the convective parameterization acts to cool the lower troposphere. By definition, ($\Pi Q_{cond}^- \equiv 0$). Overall latent heating is the greatest source of heating in the model, and plays a very minor role in cooling.

The diffusive heat tag source, ΠQ_{diff}^+ (figure 4.2c), is greatest near the surface, and its distribution reflects the height of the planetary boundary layer in the model atmosphere (Frierson et al., 2006). There is also strong diffusive heating near the tropical surface, where the hot surface provides large sensible heat fluxes into the atmosphere. There is cooling present throughout the lower- and mid-troposphere from the diffusive parameterization (ΠQ_{diff}^-, figure 4.2g). This cooling is due to boundary layer mixing that occurs when the boundary layer extends relatively deeper into the troposphere. This pattern of diffusive heating below the boundary layer and diffusive cooling above the boundary layer is also seen in the storm tracks (Ling and Zhang, 2013).

Radiative heating is the only Q^+ term in the stratosphere, visible in these plots only towards the equator. This heating reflects the parameterized shortwave absorption by ozone. As expected, the cooling from the radiative scheme (figure 4.2h) extends throughout the atmosphere. The greatest cooling rates

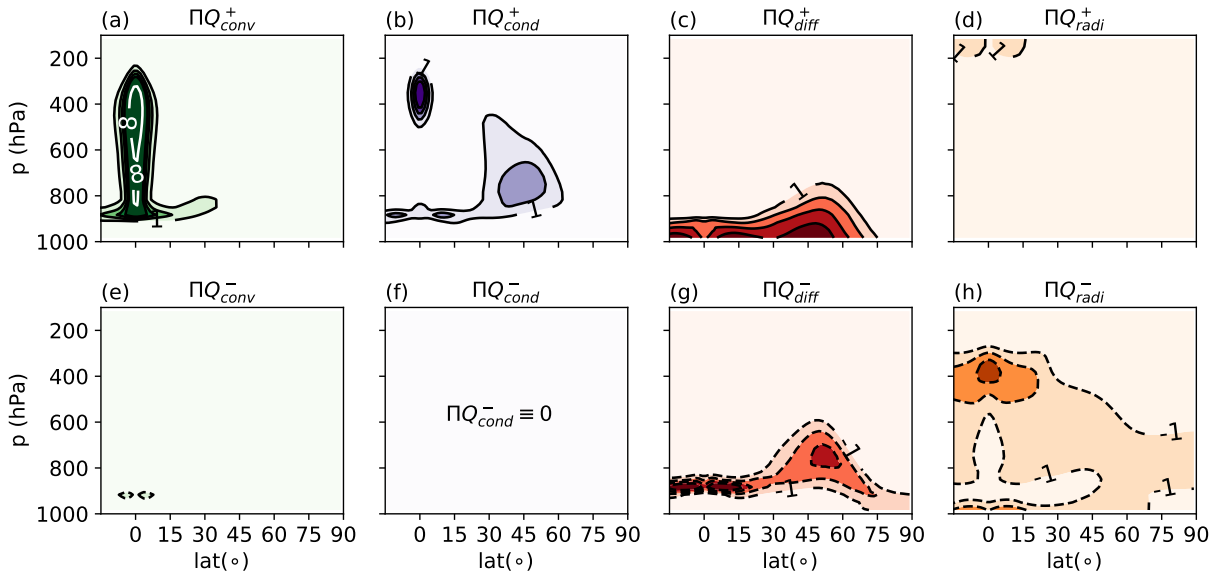

Figure 4.2: (a): zonal mean climatological positive θ tendency from Q_{conv} (contour interval 1K day^{-1}). (b-d): As in (a), but for Q_{cond}, Q_{diff}, Q_{radi}. (e-h): As in (a-d), but for the negative θ tendency. Extra contours are marked in white.

are in the tropical upper troposphere, where the strong temperatures and thin optical depth above allows for the upwelling radiation to leave the atmosphere.

The heat tag source distribution, using (4.21), allows us to estimate the global mean tracer fractions. We denote by angle bracket the climatological global mean. The evolution equation for the tag fraction implies that if the $\{\chi_i\}$ are well mixed with constant value throughout the atmosphere, their value should satisfy

$$\langle \chi_i^{mixed} \rangle \approx \left\langle \frac{\theta_i}{\theta} \right\rangle \approx \frac{\left\langle \frac{\Pi Q_i^+}{\theta} \right\rangle}{\left\langle \frac{\Pi Q^+}{\theta} \right\rangle}. \tag{4.23}$$

The well-mixed values for the four heat tags, shown in table 4.1, suggests that in this model just under one third of the θ content of the atmosphere is generated by each of subgrid-scale convection, large-scale convection, and vertical diffusion. The remaining small fraction of heat tag arises from shortwave radiation in the stratosphere. The differences between the well-mixed estimates and the actual values reflect the transport of the tags. For example if the transported tag is closer to a region of high S^- then χ_i will be decreased relative to its well-mixed estimate, and conversely if the tag is transported to a region of relatively low S^- then χ_i will be increased relative to its well-mixed estimate.

Also shown in table 4.1 is the global mean $\{< \chi_i >\}$ as calculated in the model. The well-mixed estimate of $\langle \chi_{conv} \rangle$, $\langle \chi_{cond} \rangle$, and $\langle \chi_{diff} \rangle$ are within 20% of their actual values, suggesting that these heat tags, especially the convective tag, are indeed rapidly mixed throughout the atmosphere. The $\langle \chi_{cond} \rangle$ and $\langle \chi_{conv} \rangle$ are somewhat lower than their their well-mixed estimates, suggesting that diabatic cooling acts more efficiently on these tracers, for reasons that we will explore below. The radiative tag fraction is a factor of four greater than its well-mixed estimate, suggesting strong isolation and relatively little loss from radiation.

The zonal mean climatology of the heat tags $\{\overline{\theta_i}\}$ and their zonal mean fraction $\{\overline{\chi_i}\} = \left\{\overline{\left(\frac{\theta_i}{\theta}\right)}\right\}$, are shown in figure 4.3. By construction, the $\{\overline{\theta_i}\}$ sum to $\overline{\theta}$ (shown in figure 4.1b). The distribution of the heat tags reflects their creation and loss by diabatic heating and cooling (figure 4.2) as well as atmospheric transport. Such transport is required to reach a steady state, since it is evident in figure 4.2 that the local sources are not balanced by local sinks. For instance, θ_{diff} is produced only below about 700 hPa, but the tag is mixed throughout the atmosphere. This is because there is insufficient cooling near the surface to balance the tag source, and so the tag must be distributed though a larger region of the atmosphere.

The convective heat tag, θ_{conv}, has a maximum in the deep tropics where the greatest source is located (figure 4.3a). The large transfer of energy from the surface to the atmosphere in the deep tropics has two effects on the distribution of $\overline{\theta_{conv}}$ there. Firstly, it generates convection, creating large amounts

	tag	$< \chi_i^{mixed} >$	$< \chi_i >$	$\left\langle \frac{\theta_i}{\theta_e} \right\rangle$
0	conv	0.337	0.325	0.320
1	cond	0.299	0.264	0.259
2	diff	0.299	0.274	0.269
3	radi	0.051	0.139	0.139
4	$\frac{L_v}{C_p} q$	-	-	0.015

Table 4.1: Well-mixed estimate, globally averaged tag fractions with respect to θ, $\langle \chi_i \rangle$, and the globally averaged tag fractions with respect to θ_e, $\left\langle \frac{\theta_i}{\theta_e} \right\rangle$.

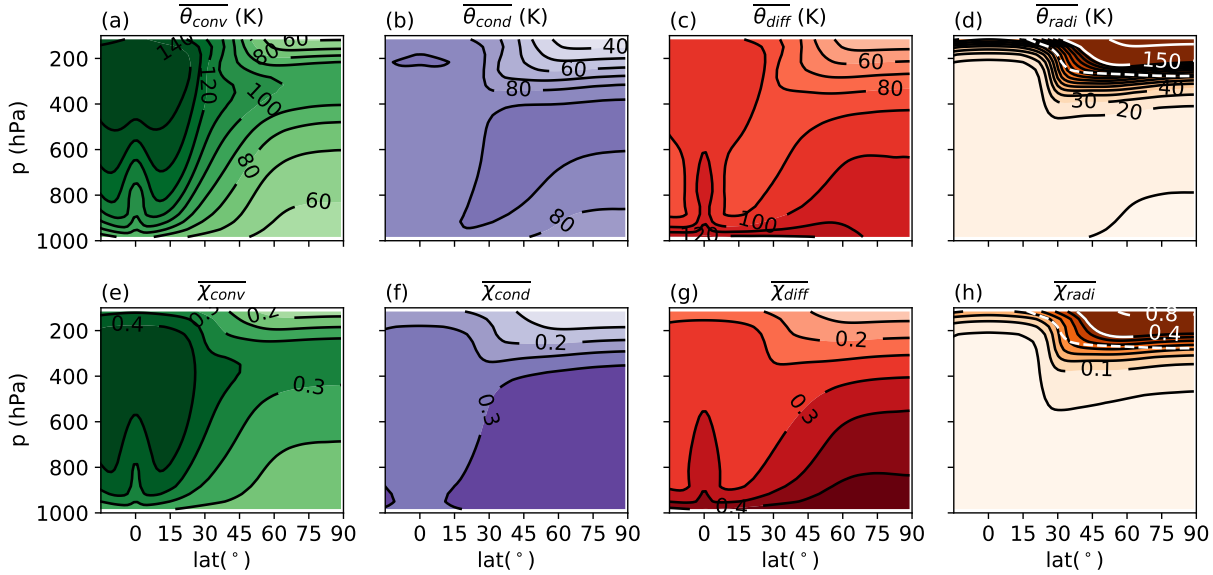

Figure 4.3: (a): zonal mean climatologies of θ_{conv} (contour interval 20K). (b-d): As in (a), but for θ_{cond}, θ_{diff}, θ_{radi}. The dashed white line in (d) is the estimate of the dynamical tropopause described in the text. (e-h): As in (a-d), but for the corresponding tag fractions χ_i (contour interval 0.05). Extra contours are marked in white.

of θ_{conv}. Secondly, it drives the Hadley circulation, which transports θ_{conv} from the lower troposphere to the upper troposphere. These effects combined create a large amount of θ_{conv} in the deep tropics with a strong vertical gradient from the surface to the upper troposphere. Thus, the tropical upper tropospheric gradient of $\overline{\theta}$ (figure 4.1a) is attributable to this convective process. Between 15° and 30° the vertical gradient is significantly reduced. This region is in the downwelling branch of the Hadley cell, which transports θ_{conv} from the upper troposphere to the lower troposphere.

Outside of the tropics $\overline{\theta_{conv}}$ has a large meridional extent, with values as high as 60-90 K over the poles: at a given altitude, warm air masses produced in the tropics are able to retain over 60% of their heat as they are transported to the poles. In the extratropics $\overline{\theta_{conv}}$ is greatest in the upper troposphere. The strength of the eddy field $\sqrt{\overline{v'^2}}$ is large in the subtropical and midlatitude upper troposphere (figure 4.1), suggesting that the eddies work to transport the convective heat tag polewards throughout the extratropics. We will return to this point in Section 4.6.

The condensation tracer tag, θ_{cond}, has a maximum in the midlatitudes, near 45°. This is a region of descent in the climatological zonal mean, so the vertical uplift required to bring parcels to saturation is occurring within the ascending regions (warm conveyor belts) of baroclinic eddies. As stated above, the strong surface temperature gradients, which produce strong eddies in the midlatitudes, not only generate Q^+_{cond} but also help to transport θ_{cond} away from the region where it is produced. Indeed the midlatitude maximum of θ_{cond} is not co-located with the midlatitude maximum of ΠQ^+_{cond}. Instead, the maximum of θ_{cond} is shifted upwards and polewards. This is indicative of the transport of the air that is heated through latent heat realease in warm conveyor belts of midlatitude cyclones before being transported upwards and polewards (Schemm et al., 2013; Pfahl et al., 2015).

The diffusive heat tag, $\overline{\theta_{diff}}$, is greatest near the surface. The strong vertical near-surface gradient from the tropics to the midlatitudes reflects the distribution of sources near the surface and sinks immediately above. In the tropics, there is an intrusion of high θ_{diff} air which extends into the mid troposphere, and compensates for the weak values of θ_{conv} in this region. This leads to a weak meridional gradients of θ in this region (figure 4.1b), and suggests a dynamical compensation between diffusive and convective processes in the deep tropics that will be discussed below. In the midlatitudes there is a strong vertical gradient over the regions where Q^+_{diff} is non-zero. Polewards of this, the vertical gradient is reduced, suggesting vertical mixing of θ_{diff} as air masses are advected poleward. There is a tongue of relatively low θ_{diff} air extending from the midlatitude upper troposphere into the subtropics. This tongue aligns approximately with $\overline{\theta}$ surfaces (figure 4.1b), which suggests that the low $\overline{\theta_{diff}}$ values in the subtropics could be linked to equatorwards descent along isentropic surfaces. This is reminiscent of the analysis of Galewsky et al. (2005), who showed that relatively dry air parcels in the midlatitude

upper troposphere descending into the subtropics controls subtropical relative humidity.

Because there is little shortwave heating in the troposphere, θ_{radi} is primarily found in the stratosphere and dominates the other heat tags there. We compare the distribution of θ_{radi} with an estimate of the dynamical tropopause. We estimate the zonal mean potential vorticity from the zonal mean climatology:

$$P \approx (f + \partial_y \overline{u})\, \partial_p \overline{\theta} \tag{4.24}$$

(the relative vorticity term is small compared to the planetary vorticity term in the upper troposphere, justifying using the climatological values in the calculation), and take the tropopause as the $\overline{P} = 1.5$PVu surface. The strong gradients of θ_{radi} effectively trace out the dynamical tropopause in the extratropics (dashed white line in figure 4.3d). In this model, stratospheric air intrusions into the troposphere are too infrequent and/or weak to maintain large values of $\overline{\theta_{radi}}$ in the presence of radiative cooling (θ_{radi} sink) in the troposphere.

Regarding the distribution of $\overline{\chi_i}$ (figures 4.3e-h), as discussed in Section 4.2, equation (4.13) suggests tradeoffs between different tag sources in this field. Thus $\overline{\chi_{conv}}$ is dominant in the upper troposphere where there is strong convective heating and $\overline{\chi_{radi}}$ (figure 4.3h) is reduced in the troposphere where other tag sources dominate.

The convective tag fraction $\overline{\chi_{conv}}$ (figure 4.3e) peaks in the tropics and accounts for just under half the total θ content in that region. The χ_{conv} tag fraction extends into the polar upper troposphere, where it remains as much as 30% of the total, consistent with its well-mixed estimate. This complements the analysis of Orbe et al. (2015a), who show that a large amount of tropical airmass sourced at the tropical surface and undergoing conservative advection is then transported to the tropical upper troposphere and then to the Arctic upper troposphere. For the heat tags as formulated here, the identity of convective tag is robust even in the presence of diabatic cooling from radiation.

The condensation tag $\overline{\chi_{cond}}$ is greatest in the extratropics, and accounts for about 30% of the θ content of mid-latitude free troposphere and polar tropospheric air (figures 4.3b and 4.3f), which is, again, consistent with its well-mixed estimate. The maximum θ_{cond} in the Arctic is located in the mid-troposphere, below the upper tropospheric maximum of Arctic θ_{conv}. These characteristics resemble air sourced at the midlatitude surface and undergoing conservative advection (Orbe et al., 2015a). The large contribution to θ in the polar column could also be anticipated from Fajber et al. (2018) (chapter 2) who showed that the poleward transport of warm air was associated with latent heating in the mid-latitudes.

It should be noted that $\overline{\chi_{cond}} + \overline{\chi_{conv}}$ amounts to more than 60% throughout most of the polar troposphere, which is consistent with a picture of rapid mixing by the eddy field. This is despite the

lack of latent heating in the polar atmosphere, indicating that the majority of the θ content in the polar troposphere is transported from remote sources, with moist processes contributing greatly (Section 4.5).

The diffusive tag makes up at least 40% of the potential temperature in the boundary layer, and this fraction increases from the equator to the pole. This follows the change in the ratio of the surface sensible to surface moisture fluxes, which also increases from the equator to the pole. As the boundary layer air gets colder it also becomes drier at a faster rate. This has the effect of increasing the fraction of the diffusive tracer tag near the polar and mid-latitude boundary layer. Low amounts of χ_{diff} are seen in the subtropical upper troposphere. This is similar to the results of Galewsky et al. (2005) who show that air in the subtropics is transported there from the upper troposphere, where the air mass has relatively little θ_{diff}.

The distribution of $\overline{\chi_{radi}}$ is similar to the distribution of $\overline{\theta_{radi}}$. Since the tropospheric radiative heating is so small compared with the other sources of tropospheric heating, $\overline{\chi_{radi}}$ is very small compared to the other tag fractions there.

4.4 Dynamical variability of the heat tags

The distributions of the individual heat tags $\{\overline{\theta_i}\}$ (figures 4.3a-d) feature more spatial structure than their sum ($\overline{\theta}$, figure 4.1b), suggesting that the distributions are not independent. Such relationships are also evident in snapshots like figure 4.4, which shows, at a typical time in the simulation, the vertical mean of the anomaly from the zonal mean of the mixing ratios for each tag. In the tropics and midlatitudes, there are regions with coincident opposite-signed anomalies of χ_{cond} and χ_{conv}. Anomalies of χ_{cond} and χ_{radi} are relatively weak in the tropics and strong in the extratropics, and also feature coincident opposite signed anomalies. The subsequent analysis explores these suggested relationships in more depth.

Given (4.15) we can decompose potential temperature variance into the variance of the heat tags and the covariance between heat tags. Denoting $\mathrm{cov}(\theta_i, \theta_j) \equiv \overline{\theta_i' \theta_j'}$ and $\mathrm{var}(\theta_i) \equiv \mathrm{cov}(\theta_i, \theta_i)$,

$$\mathrm{var}\left(\theta_i\right) = \sum_{i=1}^{N_S} \sum_{j=1}^{N_S} \mathrm{cov}\left(\theta_i, \theta_j\right) = \sum_{i=1}^{N_S} \left(\mathrm{var}\left(\theta_i\right) + \sum_{j \neq i} \mathrm{cov}\left(\theta_i, \theta_j\right) \right). \tag{4.25}$$

Figures 4.5a-d show the variance of the tags. The greatest variability in θ_{conv} is in the tropical lower troposphere (figure 4.5a). Large variability in convection near the surface and the mixing of high θ_{conv} air masses from the free troposphere into the boundary layer creates high $\mathrm{var}(\theta_{conv})$. There is also strong variability that extends through the subtropics and into the mid-latitudes. This variability is associated with the large transport of θ_{conv} through the mid-latitudes towards the poles.

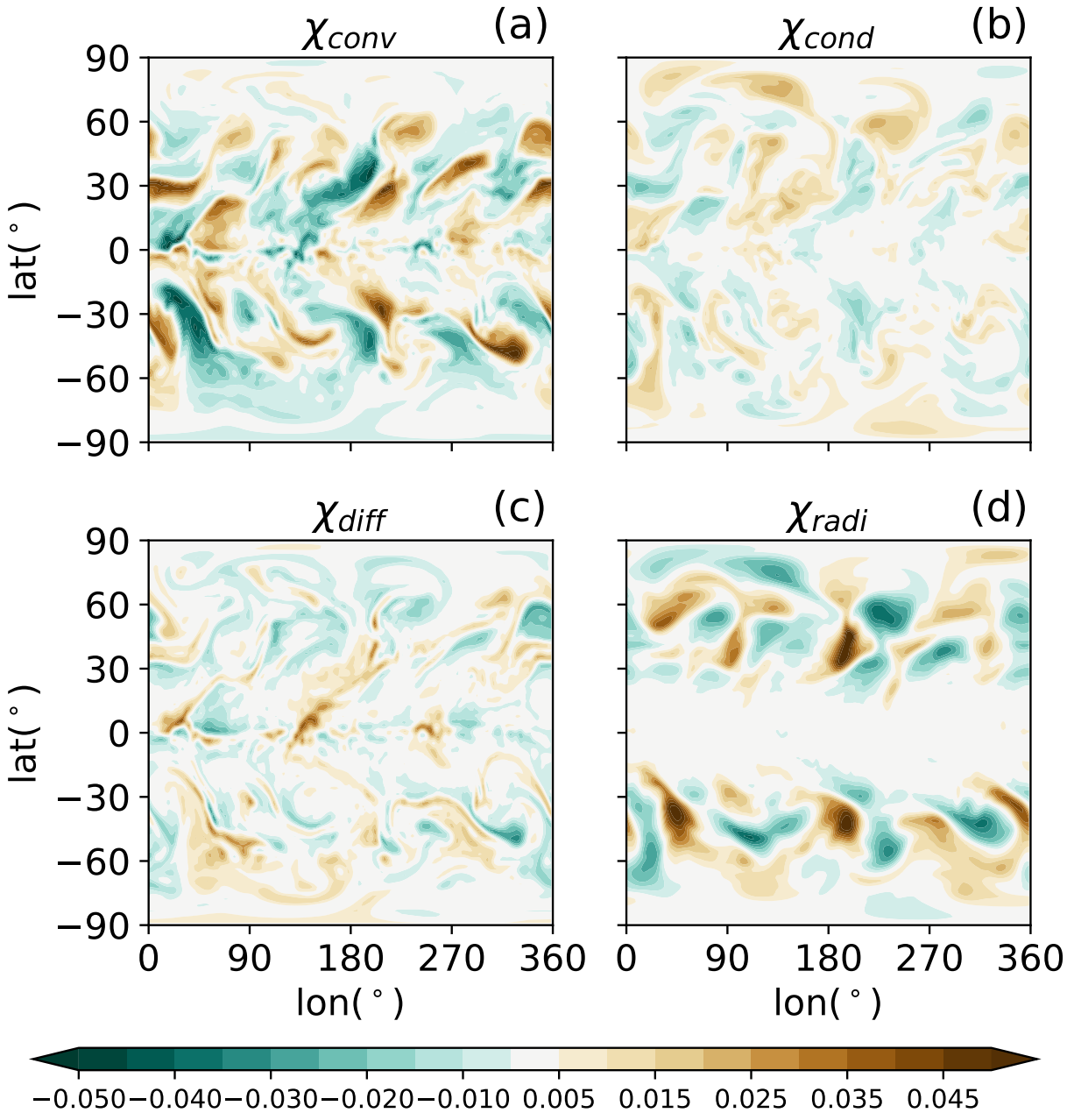

Figure 4.4: a) Representative snapshot of the vertically integrated anomaly from the zonal mean, climatogical mean χ_{conv}. (b-d): as in (a), for χ_{cond}, χ_{diff} and χ_{radi}.

The variance of θ_{cond} is large in the subtropical edge of the Hadley cell (figure 4.5b), the mid-latitude upper troposphere and also the mid-latitude near surface (around 45°). We note that the large variability in the subtropics is not near regions of large Q^{+}_{cond} (figure 4.2b). The mismatch between regions of high variability and regions of high mean θ_{conv} and θ_{cond} highlight the role of transport and dynamics in creating variability in the heat tags. If the tags were produced and removed from the atmosphere locally, then the variability would be greatest in the regions where the tags were produced, and would be attributable to variability in the source and local sink. Patterns of variance that extend far from the source reflect interactions between the tags and dynamical processes in the atmosphere.

The greatest variability in θ_{diff} is found near the surface (figure 4.5c). In contrast to θ_{conv} and θ_{cond}, θ_{diff} appears to be locally controlled in the boundary layer: variability is greatest where most of the tag is produced (figure 4.2c). This could be due to the alternating pattern of Q^{+}_{diff} and Q^{-}_{diff} (figure 4.2c and f). As θ_{diff} leaves the boundary layer it passes through a region of high Q^{-}_{diff}, which removes it from the atmosphere, and variability in this process seems to be reflected in figure 4.5c.

The radiative tag shows large variability in the stratosphere, in line with figure 4.3. Stratospheric variability in θ_{radi} represents variability in the transport of tropical stratospheric tagged air within the Brewer-Dobson circulation, which in this aquaplanet simulation is associated with upward propagating transient Rossby wave activity (Scinocca and Haynes, 1998; Kushner and Polvani, 2004; Chen et al., 2010). There is a strong gradient in var(θ_{radi}) near the tropopause. Although this model does not have a stratospheric ozone tracer, θ_{radi} is produced in the tropics through shortwave heating and then transported polewards, analogously to stratospheric ozone. The radiative heat tag θ_{radi} has an analogous negative correlation to the tropopause height, and the same dynamics which drive variability in the tropopause height will drive variability θ_{radi}, concentrated at the altitude of the tropopause (Steinbrecht et al., 1998). ree

The total variance of θ (figure 4.5e) has a midlatitude tropospheric maximum of about $50\mathrm{K}^2$ and a separate large maximum greater than $400\mathrm{K}^2$ in the stratosphere. This is much less than the maximum variance of individual tags or the sum over these variances, which indicates that there are large negative covariances between the tags. This is borne out by the terms related to covariability in equation (4.25) (figures 4.5f-h). The greatest negative covariability is between θ_{conv} and θ_{diff} in the tropical planetary boundary layer (figure 4.5g), as suggested by figures 4.4a and c, and reflecting compensation between convection and boundary layer vertical heat transport. That is, if the boundary layer scheme is able to stabilise the lower atmosphere, this will reduce convectively available potential energy and tend to suppress convection. This signature of covariability extends away from tropical surface, indicating enrichment of one tag in favor of the other in airmasses transported away from the tropical boundary

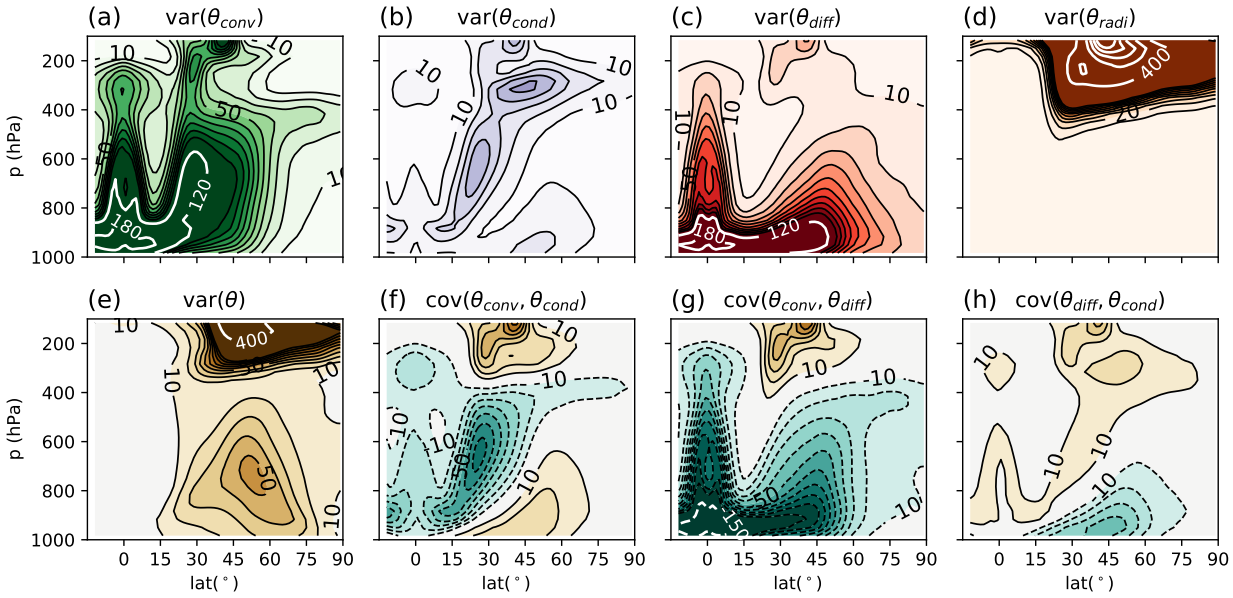

Figure 4.5: Referencing equation (4.25): (a): The zonal mean, climatological mean, variance of θ_{conv} (contour interval $10k^2$). (b-d): As in (a), for θ_{cond}, θ_{diff} and θ_{radi}. (e): As in a) but for the variance of θ. (f): As in (a), but for the covariance between θ_{conv} and θ_{cond}. (g): As in (a), but for the covariance between θ_{conv} and θ_{cond}. (h): As in (a), but for the covariance between θ_{diff} and θ_{cond}. Extra contours are in white.

layer. This is also reflected in the spatial structure in the tropical lower troposphere of the tags $\overline{\theta_{conv}}$ and $\overline{\theta_{diff}}$ compared to the total $\overline{\theta}$ (as discussed in Section 4.3; see figures 4.1b, 4.3a, and 4.3c). ci There is also large negative covariability in the tropics and subtropics between θ_{conv} and θ_{cond} (figure 4.5f, see also figures 4.4a,b), reflecting the competition between large-scale and subgrid scale condensation processes in the atmosphere. This is partially offset by the moderate positive covariability between θ_{diff} and θ_{cond} in the extratropical upper troposphere (figure 4.5h). Since θ_{cond} has a large source in the midlatitudes, we expect the covariability there to be related to midlatitude dynamics. Near the midlatitude surface $\mathrm{cov}(\theta_{conv}, \theta_{cond})$ is positive (figure 4.5f, near the surface around 45°). The correlation between Q^+_{conv} and Q^+_{cond} integrated over the bottom 15 hPa of the atmosphere between 40° and 50° is 0.92, suggesting that the positive covariability in this region is related to the dynamics controlling shallow convection. In the midlatitudes, the dynamics are dominated by the ascending and descending regions within synoptic scale eddies. In the ascending branches moisture is condensed, while the descending branches prevent the surface fluxes from destabilising the boundary layer and create regions of shallow convection (Gutowski Jr and Jiang, 1998). This contrasts with the covariance of θ_{diff} with θ_{conv} and with θ_{cond}, which are both negative in the same region (figures 4.5g-h). This indicates that the process of warming through turbulent sensible heat transfer at the surface compensates warming through condensation and latent heating on subgrid and resolved scales.

The covariance of θ_{radi} with the other tags is negative, and the greatest magnitude coincides with the region of greatest $\mathrm{var}(\theta_{radi})$ (not shown). Since θ_{radi} dominates the other tags in the stratosphere (e.g. figure 4.3g), this variability reflects the variability of the tropopause height and exchange between the stratosphere and the troposphere. When the tropopause is anomalously low (high), there are anomalously high (low) values of θ_{radi}, and anomalously low (high) values of the other tags. This is also reflected in the positive correlation between θ_{conv}, θ_{cond} and θ_{diff} in the upper troposphere (figure 4.5f-h, around 200 hPa). This suggests that the tropospheric tags all vary with the tropopause height in the same way, and so all positively correlate with each other. The large negative correlations between θ_{radi} and the other tags which cancel with the large values of $\mathrm{var}(\theta_{radi})$ to create the stratospheric maximum of $\mathrm{var}(\theta)$. Similarly, when tropospheric air is transported into the stratosphere it carries with it the signature of the tropospheric heat tags, which helps to explain the positive covariability of θ_{conv}, θ_{cond}, and θ_{diff} near 45° in the stratosphere. This region is in the center of the midlatitudes, where tropopause folding and Rossby wave breaking promotes exchange across the tropopause (Holton et al., 1995). In both cases, the positive covariance between the tags reflect the relationship between the troposphere and stratosphere.

A complimentary perspective on the variance analysis of (4.25) is provided by

$$\mathrm{var}(\theta) = \sum_{i=1}^{N_S} \mathrm{cov}(\theta_i, \theta), \tag{4.26}$$

for which each $\mathrm{cov}(\theta_i, \theta)$ (figure 4.6) indicates how tag i contributes to total θ variance. The contribution of θ_{conv} (figure 4.6a) dominates in the troposphere and is positive throughout the troposphere. This reflects how variability in tropical convective heating is communicated, via transport, into the mid-latitudes, and dominates variability there. This contribution accounts for the main tropospheric structure of $\mathrm{var}(\theta)$ equatorwards of 50° (figure 4.6a); contributions from the other tags are of mixed sign and comparatively weak in the troposphere.

Polewards of 50°, $\mathrm{cov}(\theta_{cond}, \theta)$ (figure 4.6b) and $\mathrm{cov}(\theta_{diff}, \theta)$ (figure 4.6c) make comparable contributions to $\mathrm{cov}(\theta_{conv}, \theta)$. Interestingly, polar near-surface variability in θ can be almost entirely attributed to the variability in θ_{diff}. This region of relatively stable air is isolated from the rest of the atmosphere. Thus, variability of θ in this region reflects local sources rather than long-range transport. This is consistent with the diagnosis of Orbe et al. (2015a) who find that much of the boundary layer in the Arctic remains there. The variability above the planetary boundary layer in the polar region is still dominated by $\mathrm{cov}(\theta_{conv}, \theta)$. This suggests that although local dynamics are important for the variability of the surface temperature, the variability of the mid- and upper- troposphere in polar regions is controlled by remote contributions (Fajber et al., 2018).

In the stratosphere, the dominant contribution of θ_{radi} to stratospheric θ variance (figure 4.6d) is evident. This is suggested by figure 4.4 and consistent with the results and analysis of figure 4.5 discussed above.

The coupling between the tags evident in figures 4.5e-g is of different sign in different regions, which suggests that these relationships are inherently nonlinear. To further analyse the tag inter-relationships we compute the mass-weighted joint probability distribution function (pdf) of the tag fractions. Figure 4.7 shows the joint pdf of χ_{cond} and χ_{conv} for the tropical midtroposphere (4.7a), the extratropical midtroposphere (4.7b), the tropical lower troposphere (4.7c), and the extratropical lower troposphere (4.7d). Notice that almost the entire troposphere occupies the range $0.20 < \chi_{conv} < 0.50$ and $0.2 < \chi_{cond} < 0.40$, which bracket the well-mixed estimates (table 4.1). For over 95% of the mass of the regions considered here, $\chi_{radi} < 0.05$ (not shown). In these regions, then, the diffusive tag is constrained by the two other tags via [equation ((4.12)]:

$$\chi_{diff} \approx 1 - \chi_{conv} - \chi_{cond}. \tag{4.27}$$

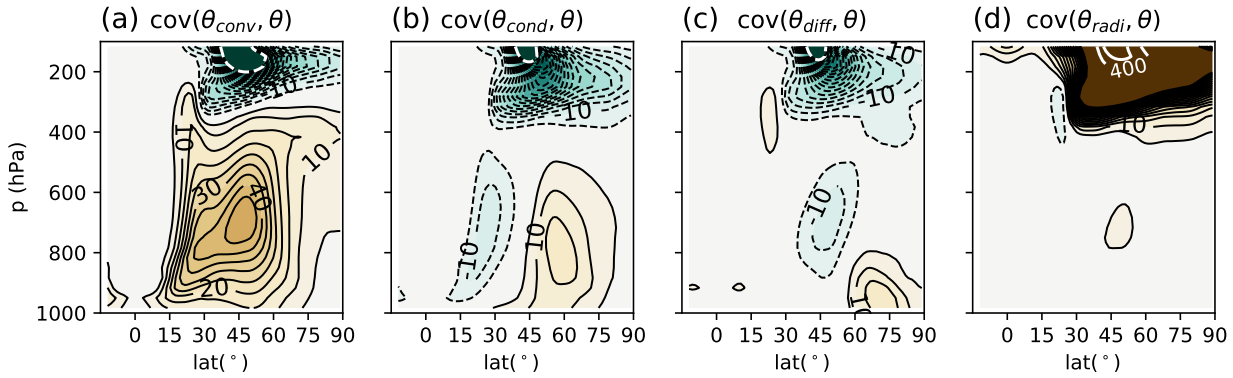

Figure 4.6: Referencing equation (4.26): (a) The zonal mean, climatological mean, covariance between θ_{conv} and θ (contour interval 10 K^2). (b)-(d) Extra contours are in white.

To aid in our analysis, we will analyse two populations, represented by the lines

$$\chi^1_{cond} = \chi^1_{conv} + 0.10 \Rightarrow \chi^1_{diff} \approx 0.90 - 2\chi^1_{conv} \tag{4.28}$$

(shown on figure 4.7a) and

$$\chi^2_{cond} = -\frac{2}{3}\chi^2_{conv} + 0.56 \Rightarrow \chi^2_{diff} \approx 0.44 - \frac{1}{3}\chi^2_{conv} \tag{4.29}$$

(shown on figure 4.7d). The relationships between χ_{conv} and the other two tropospheric heat tag fractions for these populations are sketched in figure 4.7f. We note that these relationships are for illustrative purposes and do not represent a rigorous separation of the data into distinct populations.

The first population is found mainly in the tropics. It is characterised by a long tail of high χ_{conv} values being replaced by χ_{cond} and, in a ratio of two to one, by χ_{diff}. This air features high values of χ_{conv} in the upper and mid tropical troposphere, and is then mixed with air of lower χ_{conv}. Integrating the pdfs over the region $\chi_{conv} > 0.30$, an approximate boundary for this population, we find that this population contains about 33% of the mass of the atmosphere.

The second population is mainly found near the surface. Integrating the pdfs over the region $\chi_{conv} \leq 0.26$ we find that this population makes up about 41% of the atmosphere. It is characterised by high χ_{diff} values compared to the first population. The contributions of χ_{conv} and χ_{cond} increase at the same rate, although χ_{cond} is higher. This population lies near or in the planetary boundary layer.

Between the populations, in the region $0.25 < \chi_{conv} < 0.30$ the air has $\chi_{cond} \approx 0.36$. We interpret the air in this region as resulting from the mixing of the two different populations. This mixed population is found primarily in the extratropical midtroposphere (figure 4.7b), where there are no diabatic sources in the atmosphere. In this region the fractionation between χ_{conv} and χ_{cond} is set by the mixing of air masses created in different environments. The mixed population also exists in the tropical mid and lower troposphere. This is the signature of air mixing from either the surface or polar latitudes into the tropics. Integrating the pdfs over the region $0.25 < \chi_{cond} < 0.30$ we find that this mixed population makes up about 26% of the mass of the atmosphere.

Taken together, this diagnostic suggests thinking of the troposphere as composed of an air mass with high χ_{conv} values (mid χ_{diff} and low χ_{cond} values), residing in the tropics, and an air mass with low χ_{conv} values (mid χ_{cond} and high χ_{diff} values), residing near the surface. The air mass in the lower tropical troposphere and extratropical midtroposphere come from the mixing of these two air masses.

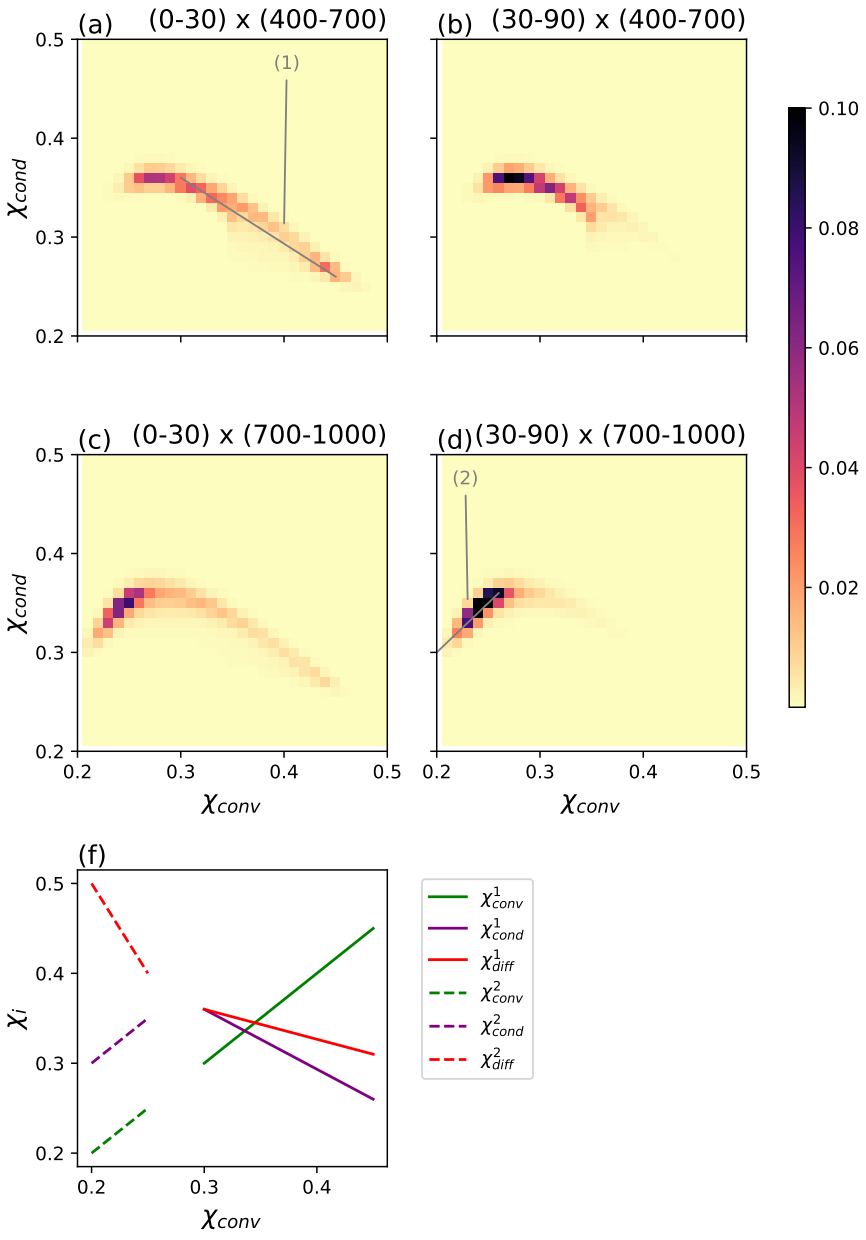

Figure 4.7: (a): Double tag pdfs for 0-30° latitude and 400-700 hPa, or the tropical mid troposphere. (b): As in (a), for the extratopical mid troposphere. (c): As in (a), for the tropical lower troposphere. (d): As in (a), for the extratropical lower troposphere. The solid grey lines in (a) and (d) describe two different populations of points, defined and discussed in the text. (f): The values of χ_{conv}, χ_{cond}, and χ_{diff} (implied by equation (4.27)) for the grey lines shown in (a) and (b).

4.5 Insights into atmospheric energy transport

The heat tags framework provides what is, to our knowledge, novel insight into the contributions of moist processes to atmospheric energy content and to poleward energy transport. The contribution of each heat tag to total atmospheric heat content (both moist and dry contributions to the moist static energy) is calculated through partitioning of equivalent potential temperature θ_e:

$$1 = \left\langle \frac{\theta_e}{\theta_e} \right\rangle \approx \sum_{i=1}^{4} \left\langle \frac{\theta_i}{\theta_e} \right\rangle + \left\langle \frac{\frac{L_v}{C_p} q}{\theta_e} \right\rangle, \tag{4.30}$$

where q is specific humidity (third column of table 4.1). The heat tags associated with latent heating ("conv" and "cond") contribute almost forty times as much heat content as the direct contribution of moisture ($L_v q/c_p$). This can be viewed as a consequence of the relatively rapid cycling of water vapor in the hydrological cycle compared to the relatively slow cycling of heat content. This assertion is supported by, first, approximating the time mean budget for $< q >$ as

$$0 \approx < E > - \frac{< q >}{\tau_q}, \tag{4.31}$$

where E is the evaporation, and precipitation has been represented by a relaxation to 0 with time scale τ_q; and second, by approximating budget for the heat content associated with latent heating by

$$0 \approx \left\langle \frac{L_v C}{c_p} \right\rangle - \frac{< \theta_C >}{\tau_C} \tag{4.32}$$

where C is the condensation (including subgrid scale and large-scale condensation, so that $\theta_C = \theta_{conv} + \theta_{cond}$), and cooling has been represented as a relaxation to 0 with time scale τ_C. Noting that $< E > \approx - < C >$,

$$\frac{< L_v q/c_p >}{< \theta_C >} \approx \frac{\tau_q}{\tau_C}. \tag{4.33}$$

The partitioning of heat content in the third column of table 4.1 can be interpreted as reflecting the long lifetime of the heat tags related to latent heating (dissipated by radiative cooling to space over several weeks) compared to the short lifetime of water vapor (which is rapidly removed by precipitation over a few days). Equation (4.15) implies that these contributions are additive across tags.

4.5.1 Vertically Integrated Tag Transport

The vertically integrated transport total, mean, and eddy, transport of a given tag are given by

$$
\begin{aligned}
H_i^T &= 2\pi a \cos\phi \int \overline{v\theta_i} \frac{dp}{-g} \\
H_i^M &= 2\pi a \cos\phi \int \overline{v}\,\overline{\theta_i} \frac{dp}{-g} \\
H_i^E &= 2\pi a \cos\phi \int \overline{v'\theta_i'} \frac{dp}{-g}
\end{aligned}
$$

respectively. The transport of θ, is the sum of the tag transports: $H_\theta^T = \sum_i H_i^T$. Similar experessions hold for H_θ^M and H_θ^E.

Total θ transport is dominated by a poleward flux of magnitude 6 PW from H_{conv}^T (green curves in figure 4.8) from the tropics into the midlatitudes (grey and green curves in figure 4.8c). In the tropics, this is dominated by the Hadley circulation term H_{conv}^M (figure 4.8a) which is then taken over by eddy term H_{conv}^E (figure 4.8b) in the extratropics. Heat tags quantify how convectively heated air is transported out of the deep tropics through the Hadley cell, which is then transported further polewards by the midlatitude eddies (Trenberth and Stepaniak, 2003b).

The remaining heat tags are responsible for relatively less θ transport. The θ_{cond} transport H_{cond}^T is dominated by H_{cond}^E, which is negative equatorwards of 45° and positive polewards of 45° (purple curves in figure 4.8). Since there is a maximum of the source of the condensation tag, ΠQ_{cond}^+ around 45°, this suggests that the eddies are transporting θ_{cond} away from the region where it is produced. H_{cond}^M is relatively weak in comparison. The relatively weak transport of the diffusive tag by the mean circulation, H_{diff}^M (red curves in figure 4.8), is opposite in sign to that of H_{conv}^M, simply because $\overline{\theta_{conv}}$ is amplified in the upper troposphere and $\overline{\theta_{diff}}$ is amplified at the surface (figure4.3a and d). Similar to H_{cond}^E, H_{diff}^E diffuses energy away from the maximum of the source of θ_{diff}, which is around 60°.

Even though the tag with a tropical source, θ_{conv}, plays the largest role globally, in the high latitudes the tags with midlatitude sources, θ_{cond} and θ_{diff}, become more important. At 50° $\left(H^T{}_{cond} + H_{diff}^T\right)/H^T{}_\theta$ is small, but by 50° $\left(H^T{}_{cond} + H^T{}_{diff}\right)/H^T{}_\theta \approx 0.4$, and polewards of 65° $\left(H^T{}_{cond} + H_{diff}^T\right)/H_\theta^T \approx$ 0.65. In comparison, at 50° $H_{conv}^T/H_\theta^T \approx 0.7$, but by 50° $H_{conv}^T/H_\theta^T \approx 0.4$, and polewards of 65 ° $H_{conv}^T/H_\theta^T \approx 0.3$, less than half that of $\left(H^T{}_{cond} + H_{diff}^T\right)/H^T{}_\theta$. Thus, heat transport from θ_{cond}+θ_{diff} is important for maintaining the heat content of the polar atmosphere, even though it is relatively small in other regions.

The total transport of the radiative tag, H_{radi}^T (orange curves in figure 4.8), is a small residual between the sum of large equatorward H_{radi}^M transport and an equal and opposite poleward H_{radi}^E (comparing the yellow curves in figure (4.8a-c)). This causes a large cancellation between H_θ^M and H_θ^E in the midlatitudes, which does not occur in H_θ^T. Indeed $H_\theta^T - H_{radi}^T$ (cyan curves in figure 4.8) does not show the same cancellation between mean and eddy components.

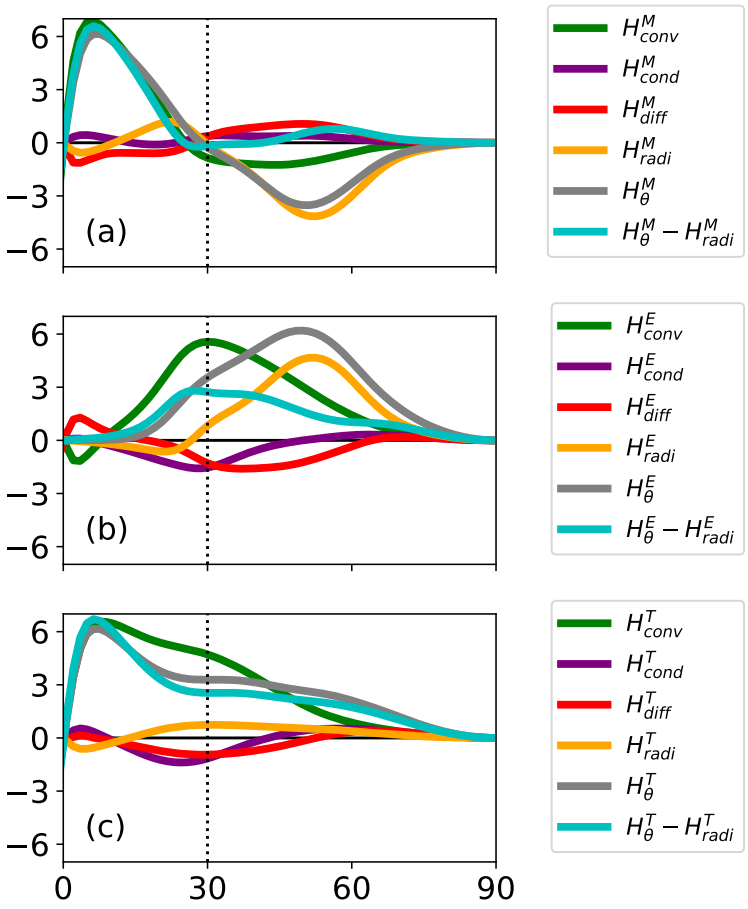

Figure 4.8: (a): Vertically integrated mean transport for the heat tags, θ, and θ minus the transport of θ_{radi} (untist are PW). The dashed line shows 30°, roughly the edge of the tropics. (b): As in (a) but for the eddy transport. (c): As in (a) but for the total transport.

We are not confident in the ability of this low-top model with a poorly represented stratosphere to capture these features. In particular, this version of the model makes use of the default sponge layer formulation based on Rayleigh drag applied to the zonal winds, which can readily lead to spurious circulations in the stratosphere (Shepherd and Shaw, 2004). Since H^T_{radi} is still required to be small by the diabatic tendencies in the stratosphere, a large compensatory H^E_{radi} is developed. Capturing heat tag processes within a model with a more realistic stratospheric representation merits further investigation. This begin said, we note that diagnosing the midlatitude compensation in H^M_θ and H^E_θ as a result of the stratospheric transport was aided by having the heat tags. This highlights the potential of the heat tags to understanding atmospheric heat transport, and diagnosing unrealistic aspects of the simulated heat transport.

4.5.2 Using the heat tags to elucidate the role of moisture in the total heat transport

Traditional analysis splits $H^T_{\theta_e}$ into a heat transport from the moisture transport,

$$H^T_q = 2\pi \cos\phi a L_v \int \overline{vq} \frac{dp}{-g} \tag{4.34}$$

and a heat transport from the dry air transport H^T_θ (e.g. Shaw and Pauluis, 2012):

$$H^T_{\theta_e} \approx H^T_q + H^T_\theta . \tag{4.35}$$

This decomposition is shown in figure 4.9a. In the tropics there is significant compensation between H^T_q and H^T_θ. As is well known, the lower branch of the Hadley cell creates a tropical moisture convergence (H^M_q, dotted blue line in figure 4.9a). Condensation occurs in deep tropics, balancing the moisture convergence, and warming the atmosphere. The warm air is exported from the tropics in the upper branch of the Hadley cell in the tropics (H^M_θ, dotted grey line in figure 4.9a) and eventually by eddy fluxes (Trenberth and Stepaniak, 2003b). The total mean transport in the tropics ($H^M_{\theta_e}$ dotted black line in figure 4.9a) is a small residual between the moist and dry transports. Outside of the tropics the large equatorward H^M_θ values are due to the stratospheric mean circulation and θ_{radi} (the values almost match figure H^M_{radi} in 4.8a). In the extratropics both H^T_θ and H^T_q play comparable roles in the $H^T_{\theta_e}$, and the transport is dominated by the eddies.

Can H^T_q be interpreted in isolation as the contribution of the hydrological cycle to the total heat transport? The answer is no, because the removal of water vapor in the atmosphere through phase

changes results in latent heating. This warms the air, which can then be transported further before being cooled, resulting in a conversion from H_q^T to H_θ^T, but without changing the total transport $H_{\theta_e}^T$.

Using the heat tags we can remove this cancellation and isolate the component of the heat transport that is directly linked to the energy put into the atmosphere through evaporation. To do this we combine the heat tag transport related to latent heating and combine it with H_q^T, e.g.

$$H_{\theta_e}^T \approx (H_q + H_{conv} + H_{cond}) + (H_{diff} + H_{radi}) = H_{moist} + H_{dry}. \tag{4.36}$$

The first term of (4.36), H_{moist}^T is the heat transport through either the transport of water vapor or through the transport of heat created by latent heat release from water vapor condensation in the model's subgrid convection or resolved condensation schemes. The second term H_{dry}^T is the heat transport unrelated to the transport or phase changes of water vapor. In appendix B we show that the source appearing in H_{moist}^T is the evaporation, while the only sources appearing in H_{dry}^T are ΠQ_{diff}^+ and ΠQ_{radi}^+. The latent heat from convection or condensation does not appear in either of the divergences; it is removed by a cancellation with removal of water vapour in the divergence of H_q^T. This mirrors the divergence of $H_{\theta_e}^T$, which also does not contain any latent heating terms (Trenberth and Stepaniak, 2003a).

Arguably H_{moist}^T better represents the heat transport associated with the hydrological cycle, since it results from the balance between energy added to the atmosphere from evaporation and the diabatic cooling required to balance this energy input. This is the same energy balance that was used at the start of Section 4.5 to compare the timescales of the tags related to latent heating and water vapor.

The decomposition of the total heat transport into H_{moist}^T and H_{dry}^T is shown in figure 4.9b. The compensation between the H_q^T and H_θ^T in the tropics has been removed. Instead H_{moist}^T is single signed, showing the overall flow of energy out of tropics. A transfer from H_{moist}^M to H_{moist}^E happens near the edge of the tropics, similar to H_{conv}^M and H_{conv}^E. The total transport is dominated by the H_{moist}^T term everywhere except for polewards of 75°, where H_{dry}^T becomes comparable to H_{moist}^T. The negative values of H_{dry}^M in the midlatitudes are attributable to H_{radi}^M, and are compensated by the H_{radi}^E in the total (figure 4.8a-c, see Section 4.5.1).

The large role that H_{moist}^T plays in $H_{\theta_e}^T$ globally could not be inferred from the results of table 4.1. Although the components of H_{moist}^T combined make up just over 60% of total atmospheric heat content, this is still less than the fraction of $H_{\theta_e}^T$ from H_{moist}^T. This means that the size of H_{moist}^T is not solely due to the large amount of moisture related tags in the atmosphere, and instead reflects the relationship between the processes that add moisture related heat to the atmosphere and atmospheric transport.

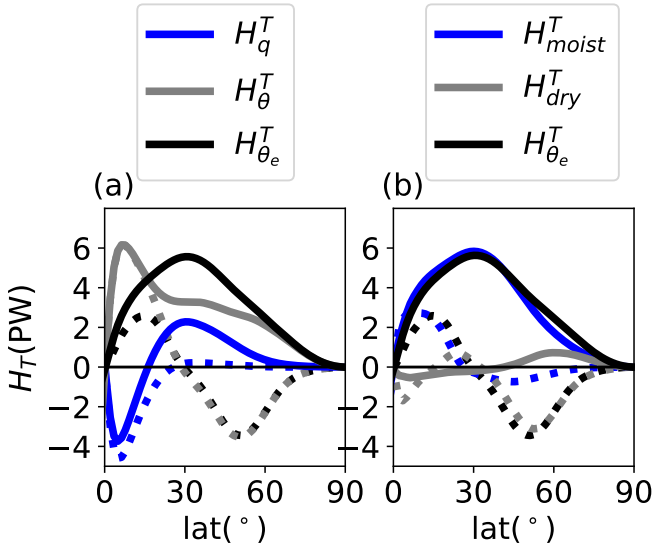

Figure 4.9: (a): Decomposition of the total transport $H_{\theta_e}^T$ into H_q and H_θ. The corresponding H_i^M are shown as dotted lines to show the Hadley circulation. (b): As in (a), but for H_{moist}^T and H_{dry}^T.

4.6 Response to Greenshouse Warming

As stated in Section 4.2, the radiative scheme used in our version of the model has a nominal CO_2 value of 360 ppm. The response of the system, including dynamic variables and heat tags, to climate change is explored by doubling the CO_2 to 720 ppm and integrating the model for 3000 days, and using the last 2500 days for averaging. This "2xCO_2" similation will be compared to the 360 ppm control simulation, "CLIM".

4.6.1 Response of the Mean Climate

The difference between 2xCO_2 and CLIM is shown in figure 4.10. The response of $\overline{\theta_e}$ (figure 4.10a) is greatest in the tropics, where it is almost vertically uniform. The $\overline{\theta}$ response (figure 4.10b) is greatest in the upper troposphere at the top of the Hadley cell, indicating an increase of moisture in the lower tropical atmosphere. There is a secondary center of warming in both $\overline{\theta_e}$ and $\overline{\theta}$ in the lower polar atmosphere; this aquaplanet model displays weak polar amplification when the poles are compared to the midlatitudes. In the subtropical lower stratosphere there is a decrease in both $\overline{\theta_e}$ and $\overline{\theta}$. Taken with the increase in $\overline{\theta}$ in the upper tropical troposphere this implies an upwards shift of the tropopause height. This raising of the tropopause is also observed in many of the other fields looked at in this Section.

Along with these thermodynamic changes there are relatively small dynamical changes: The mean streamfunction $\overline{\psi}$ increases in the tropical upper troposphere (figure 4.10c), and there is also a small reduction in the transient eddy activity (as measured by $\sqrt{\overline{v'^2}}$) in the subtropics, with an increase in the upper troposphere (figure4.10d).

The changes to the tag sources and sinks, ΠQ_i^+ and ΠQ_i^-, are shown in figure 4.11. As anticipated from the increase in the strength of the Hadley cell there is an increase in tropical convective heating (figure 4.11a). There is also a decrease in subtropical convective heating, consistent with the strengthening of the downwelling branch of the Hadley cell. Condensational heating, ΠQ_{cond}^+, shifts upwards in the tropics, consistent with the upwards shift of the tropopause (figure 4.11b). The ΠQ_{cond}^+ midlatitude maximum shifts polewards in the extratropics and increases in strength and depth. This is consistent with the baroclinic eddies condensing more moisture. Since there is not an appreciable change in $\sqrt{\overline{v'^2}}$ in the same region (figure 4.12d) the changes in condensation must be mostly coming from the change in supply of water vapor.

The increase of the latent heating terms ΠQ_{conv}^+ and ΠQ_+^{cond} contrasts with the response of the sensible heating term ΠQ_{diff}^+ (figure 4.11c), which shows a decrease throughout most of the extratropics (although there is a small increase polewards of 60° and in the tropics)). This implies that in 2xCO_2

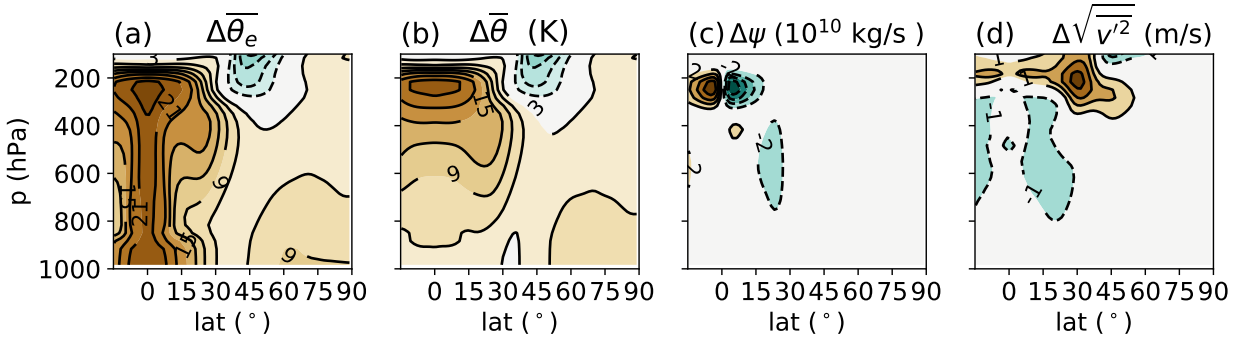

Figure 4.10: As in figure 4.1, but for the difference between $2XCO_2$ and CLIM. Contour intervals are (a) 3K, (b) 3K, (c) $2\times10^{10}\text{kgs}^{-1}$,(d) 1ms^{-1}.

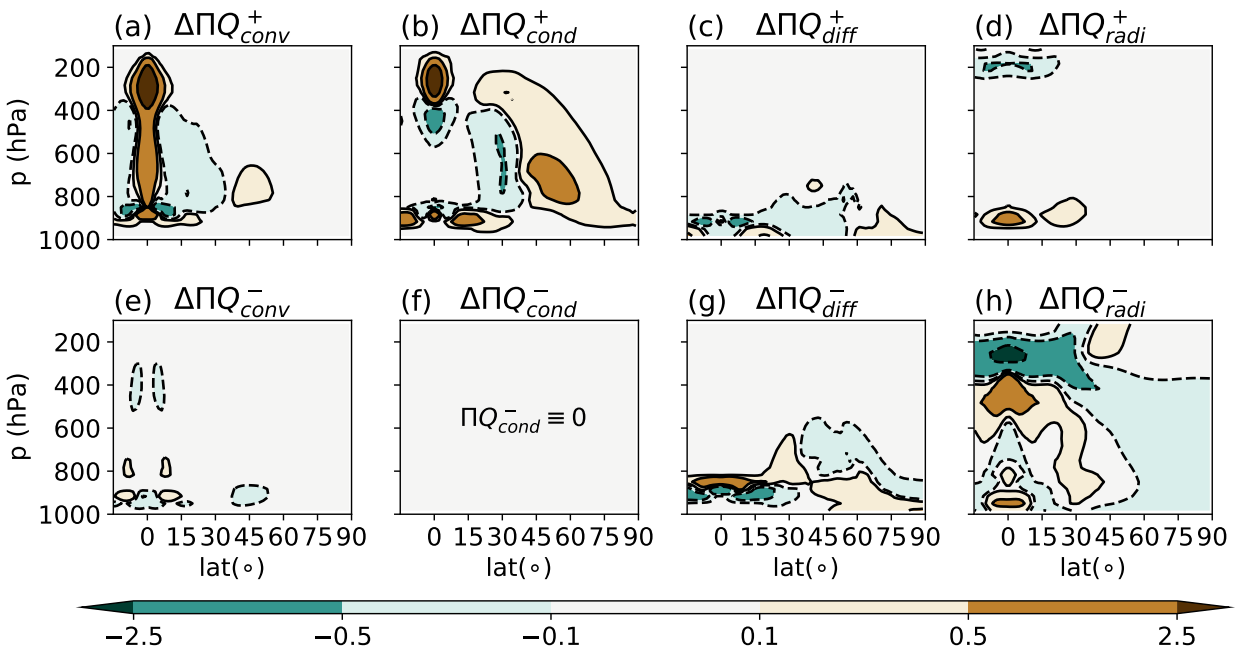

Figure 4.11: As in figure 4.2, but for the difference between $2XCO_2$ and CLIM.

more energy is transferred to the atmosphere from the surface through latent heating and less through sensible heating than in CLIM.

There is increased longwave cooling throughout most of the extratropical troposphere (figure 4.11h). In the tropics, the cooling has been raised to a higher level in the atmosphere, corresponding to a raising of the tropopause. There is still some cooling coming from the ΠQ^{-}_{diff} term which experiences only minor changes in the extratropics.

The changes in the diabatic tendencies are apparent in the well mixed estimates of the global tag fractions, χ_i^{mixed} (table 4.2, first and fourth columns). The increase in convection and condensation increase their respective well-mixed estimates, while the diffusive well-mixed estimates have decreased, showing that latent heating is responsible for relatively more of the atmospheric heat content in the new, warmer troposphere. The radiative tag source and sink both decrease in the stratosphere, so that the well-mixed estimate of the radiative tag remains relatively unchanged.

The actual increases of $\langle \chi_{conv} \rangle$ and $\langle \chi_{cond} \rangle$ closely follow the increases in the well-mixed estimates. By comparison, $\langle \chi_{diff} \rangle$ decreases less than its well-mixed estimate and $\langle \chi_{radi} \rangle$ decreases while its well-mixed estimate stays approximately the same.

The increases in moisture and moist tags are also reflected in their relative contributions to θ_e (table 4.2, third and sixth columns). Both of them increase, reflecting the increase of moisture and subsequent latent heating in the atmosphere. The increase in moisture is comparatively larger however, leading to an increase in the ratio of residence times, $< \tau_q > / < \tau_C >$, and hence the importance of water vapor transport in total energy transport, of (approximately) 30%.

The climate response of the distribution of the heat tags is shown in figure 4.12. The most striking difference is an increase in θ_{conv} (figure 4.12a) and θ_{cond} (figure 4.12 b), and a decrease in θ_{diff}(figure 4.12 c) throughout the entire troposphere. The total of these three tags is almost equal to the total change in θ in the troposphere (figure 10b). The decrease in θ_{diff} is more than compensated by the differences in θ_{conv} and θ_{cond}, and so the overall change in θ is positive. This is true not only for regions like the tropical upper troposphere or extratropical midtroposphere where there are increases in latent heating, but also in regions like the extratropical upper troposphere, the polar mid troposphere and the lower troposphere where there are not. Indeed, using the heat tags we see that even though there is an increase in ΠQ^{+}_{diff} in the polar region, there is a decrease in θ_{diff} and an increase in θ_{cond}. This means that the change in θ should be attributed to moist processes that are occurring at remote latitudes, instead of due to a local change in sensible heating at the surface. This recalls the results of Orbe et al. (2015b), who showed that an increase in atmospheric CO_2 resulted in an increase air in last in contact with the surface in the midlatitudes in the middle and lower arctic troposphere.

	tag	$< \chi_i^{mixed} >$	$< \chi_i >$	$\left\langle \frac{\theta_i}{\theta_e} \right\rangle$	$\Delta < \chi_i^{mixed} >$	$\Delta < \chi_i >$	$\Delta \left\langle \frac{\theta_i}{\theta_e} \right\rangle$
0	conv	0.354	0.342	0.335	0.017	0.017	0.014
1	cond	0.326	0.291	0.285	0.027	0.027	0.025
2	diff	0.258	0.244	0.239	-0.041	-0.029	-0.031
3	radi	0.052	0.127	0.126	0.001	-0.012	-0.012
4	$\frac{L_v}{C_p} q$	-	-	0.021	-	-	0.006

Table 4.2: As for table 4.1, but for the 2xCO_2 run and the difference between the 2xCO_2 run and the control run.

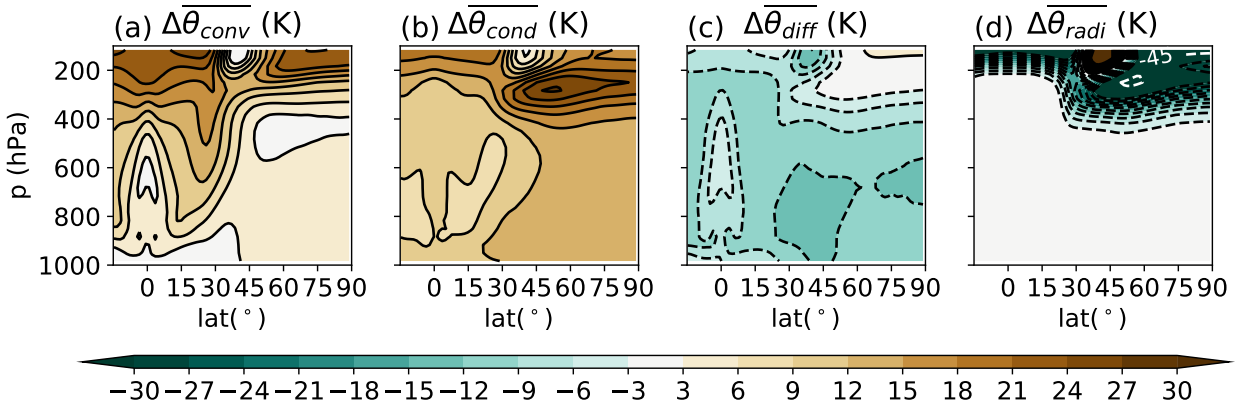

Figure 4.12: As in figure 4.3(a-d), but for the differences between 2XCO2 and CLIM.

There is a decrease in $\overline{\theta_{radi}}$ throughout most of the stratosphere, consistent with a decrease in ΠQ^{+}_{radi} in the stratosphere. The exception is in the stratosphere near 45°, where there is an increase in $\overline{\theta_{radi}}$, coincident with a decrease in $\overline{\theta}$. This indicates that this region is becoming less connected to the stratosphere, even though the stratospheric θ is decreasing slightly (since these θ are in the stratosphere the changes are very small relative to the climatological θ). The dynamical mechanisms behind this midlatitude anomaly are left to future study.

The moister atmosphere leads to an increase in $H^T_{\theta_e}$ (figure 4.13a). As expected from CLIM there is compensation between increasing H^T_q and H^T_θ in the tropics. Interestingly, the change in moisture convergence is not caused by the mean flow transport (H^M_q, the dashed blue line in figure 4.13a, is relatively small). This is consistent with the lack of intensification in the lower branch of the Hadley cell (figure 4.10c). Instead the moisture convergence that is required to balance the increase in tropical convection and condensation is accomplished by an increase in eddy moisture transport.

When we decompose $H^T_{\theta_e}$ into H^T_{moist} and H^T_{dry} the apparent competition between the dry and moist responses in the tropics is removed (figure 4.13b). The total response is dominated by H^T_{moist} everywhere. This is consistent with the general increase in the tags related to moisture. The small decrease in H^T_{dry} around 50° is related to the change in the transport of θ_{radi} (not shown). Overall, the picture of the response is an increase of moisture (the difference between figures 4.10a and 4.10b) and moist heat tags (figures 4.12a-b), which are redistributed by a net transport (figure 4.13) through a circulation which is little affected by climate change (at least as measured by the circulation statistics in figure 4.10), similar to the picture of Held and Soden (2006).

Additional features of the response are also of interest. The decrease in θ_{radi} seen in the extratropics (figure 4.12d) is related to the increase in the tropopause height, which displaces high θ_{radi} air. There is also a minor change in the tropospheric radiative tag related to a small change in the tropospheric source. The changes in longwave cooling in the stratosphere are relatively weak.

The increases in θ_{conv} also have implications for the variance decomposition of θ response (not shown). There is an increase in var(θ_{conv}) of approximately 50% in the subtropics, which is partially compensated for by a decrease in var(θ_{cond}), so that var(θ) only increases by about 10% in the subtropics. The consequence of this is that in 2xCO2, subtropical var(θ) is driven more by tropical convectively heated airmasses than in CLIM. This means that for models to accurately forecast future climate changes in the midlatitudes and polar atmosphere capturing the response of tropical convection and latent heating may be key.

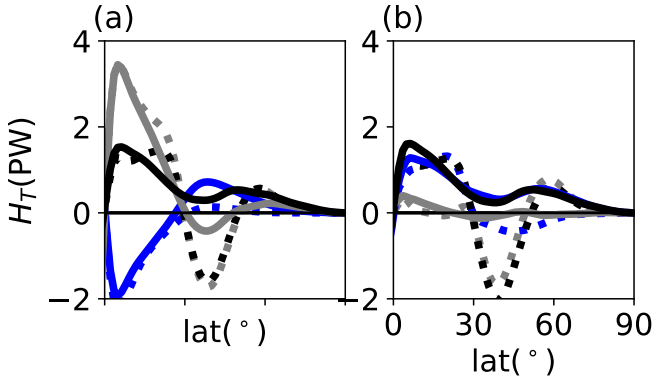

Figure 4.13: As in figure 4.9, but for the difference between $2XCO_2$ and CLIM.

4.7 Summary

In this study, a passive tracer system, called heat tags, was developed and applied to an idealized aquaplanet model to attribute the potential temperature in an air mass to the processes that heat the atmosphere. The novel aspect of the method is to treat the heat tags as material substances by separating the diabatic terms by sign at every time and location so that heating tags air masses, and cooling removes heat proportional to the amount of tags. This method ensures that the tags remain non-negative, and since they sum to the total potential temperature they remain finite. This study has served as a proof of concept for the idea of heat tagging in climate model experiments, and has given us insights into the ways that diabatic heating can influence heat content in remote regions.

The main conclusions are summarized here:

1. The tag sources tend to be localised, while the tag distributions extend throughout the atmosphere. This is because a large fraction of cooling is through longwave cooling which is spread throughout the troposphere, and so the tags must spread out in order to reach a steady state balance.

2. The tags related to latent heating (θ_{conv} and θ_{cond}) make up 60% to 80% of the θ content of the free troposphere, including in the polar troposphere where there is minimal latent heating. Even though water vapour itself makes up less than 2% of the moist static energy in the atmosphere, the energy released from condensation of water vapor makes up a large fraction of the total θ in the troposphere.

3. The variance of the potential temperature in the troposphere is largely due to the variability of convectively generated heat (θ_{conv}), with small contributions from θ_{cond} and θ_{diff} only in high latitudes.

4. The mid and lower troposphere are composed of two populations: an upper tropical population with relatively high fractions of χ_{conv} and low values of χ_{diff}, and a surface population with a comparatively low fraction of χ_{conv}. These two populations mix in the extratropical midtroposphere and in the tropical lower troposphere.

5. Much of the heat transport in the tropics and midlatitudes happens through the polewards transport of θ_{conv}, initially through the Hadley circulation and then through eddy transport. The transport of θ_{cond} and θ_{diff} transports θ both equatorwards and polewards, away from the regions where they are created.

6. Using the heat tags to decompose the dry heat transport into various components, we find that the greatest heat transport in the atmosphere occurs through convectively heated airmasses moving out of the topics and into the subtropics and midlatitudes.

7. The heat tags can be used to isolate the component of the heat transport that is due to the hydrological cycle (H^T_{moist}), which dominates the total atmospheric heat transport.

8. Under CO_2 doubling, there is an increase in the tags related to latent heating (θ_{conv} and θ_{cond}), and a decrease in the tag related to sensible heating θ_{diff}, including the high latitudes, where there is no latent heating.

4.8 Discussion

These results have highlighted the important role that the hydrological cycle plays in determining heat transport in the atmosphere. There are two ways to look at this. The first is the dry, or θ perspective: the large amounts of latent heating in the atmosphere, particularly in the tropics, creates warm airmasses that need to be redistributed to the subtropics and poles where there are large amounts of longwave cooling. The transport of these air masses away from the tropics dominates the heat transport through the low and mid latitudes, and dominates the variability of θ in the midlatitude midtroposphere. This is the perspective from analysing the atmospheric heat transport in terms of $H^T_{conv} + H^T_{cond}$. The second is the moist static energy, or θ_e perspective: evaporation adds large amounts of energy to the atmosphere that must be first condensed and then balanced by longwave cooling. Latent heating does not change the total θ_e of an air parcel, but it will transfer it from latent energy to thermal energy. The total heat transport primarily balances the heat being added by evaporation with a fraction of the total cooling in the atmosphere. This is the perspective from analysing the atmospheric heat transport in terms of $H^T_{moist} = H^T_{conv} + H^T_{cond} + H^T_q$.

We assert that this additional perspective can only be quantified using heat tags. Comparing θ and θ_e can show the presence or transport of water vapor (Pauluis et al., 2008, 2010; Fajber et al., 2018), but comparing the two cannot partition how much of the thermal energy originally came from latent heating. The advantage of using heat tags as opposed to analysing θ or θ_e on their own is that we are unable to separate the contributions from latent heating or evaporation, respectively, from sensible and radiative heating. This separation is what enables us to track the heat from the hydrological cycle far from its source.

Since convective heating is greatest in the tropics and radiative heating is greatest in stratosphere,

we have interpreted these tags as containing regional information. This is a happy accident of our model, however; there is no guarantee that diabatic heating needs to be regionally isolated as it is in our model. For instance, if the convective relaxation time was increased, then large-scale latent heating would increase in the tropics (Frierson, 2007), and θ_{conv} would no longer be a significant fraction of the tropical θ content.

In another approach, heat tags can be subdivided to be sourced from different spatial regions similar to water tagging (Singh et al., 2016; Dyer et al., 2017). This is challenging with our current model set up, since these tags can have sharp gradients which our spectral transport scheme has difficulty resolving. However there is nothing inherit in our method which prevents further regional decomposition.

In any case, for the current model configuration, we have learned that 1) only a small fraction of the standard deviation of θ is attributable to sensible heating, and this is mostly confined to the polar near surface, and 2) in the midlatitudes the majority of the variability arises from tropical latent heating. This means that characterizing the variability in this region requires an accurate representation of the tropics and the transport connecting the tropics and midlatitudes. For this idealized aquaplanet model, the variability of midlatitude θ is controlled by the mixing of tropically warmed airmasses into the midlatitudes.

While the idealized configuration of our model has been useful in demonstrating the utility of our approach, several important controls on transport remain to be studied. Surface inhomogeneity can shape the distribution of passive tracers by introducing stationary waves, which accomplish a large fraction of the transport in the subtropics (Holzer, 1999; Holzer and Boer, 2001). Since the convection parameterization of this model does not simulate a mass flux, we cannot explicitly capture the convectively triggered mass transport, which plays an important role in transport tracers from the boundary layer to the upper troposphere in the deep tropics (Erukhimova and Bowman, 2006), and seasonally can play a large role over Asia in ventilating the upper troposphere and lower stratosphere (Orbe et al., 2015c). The lack of a seasonal cycle also prevents us from studying the previously documented effect that the Hadley cell migration has on interhemispheric transport (Bowman and Erukhimova, 2004) and the transport from the midlatitudes to the Arctic (Yang et al., 2019). Applying heat tagging to models with less idealized insolation and boundary conditions will bring insights into these processes and the role that long range transport plays in climate. Our hope is that this method can be extended to more state-of-the-art circulation models and help to provide guidance into model development by linking the heat content of remote regions.

Appendix A: Initialization and numerical accuracy of the heat tag system

In order to initialize the heat tagging system we need to choose an initial distribution of tags that satisfies

$$\sum_i \theta_i(t=0) = \theta(t=0).$$

One possible way to do this is to add a tag, θ_0 with no sources, e.g. a tag that satistfies

$$\frac{\partial \theta_0}{\partial t} = -\nabla \cdot (\underline{v}\theta_0) + D_H(\theta_0) + \Pi \frac{\theta_0}{\theta} Q^-,$$

as the model spins up θ_0 will decay towards 0. However since there are only weak diabatic sources and sinks in the stratosphere this model configuration the radiative tag has a considerably longer lifetime in the atmosphere than the other tags, similar to the long residence times of airmasses in the stratosphere (Hall and Plumb, 1994). Choosing $\theta_{radi}(t=0) = \theta(t=0)$ with the other tags set to 0 reduces the time for the stratosphere to equilibriate, so that we do not have to wait for the stratosphere to equilibrate. An example of the transient adjustment is shown in figure 4.14. Initially $\chi_{radi} = 1$, but as the other tags are added and θ_{radi} is removed the tags equilibrate within approximately 2500 days.

To ensure that the equilibrium state conserves the total tag mass, we calculate the root mean square difference between θ and $\sum_i \theta_i$:

$$R = \left(\frac{1}{T} \int_0^T \left(\theta - \Sigma_i \theta_i\right)^2 dt \right)^{\frac{1}{2}}. \tag{4.37}$$

The distribution of numerical errors averaged over 2000 days after spinup is shown in figure 4.15. The error is less than 1% throughout most of the troposphere, and less than 2% everywhere below 200 hPa. The regions with higher R are regions with relatively higher amounts of radiative tracer tag. Improving upon these errors, is left to future research.

Appendix B: Divergences of H^T_{moist} and H^T_{dry}

Ignoring horizontal diffusion, the vertically integrated, time mean forms of equations (18a-d) are

$$div\left(H^T_{conv}\right) = \int \Pi\left(\overline{Q^+_{conv}} + \overline{\chi_{conv}Q^-}\right)\frac{dp}{-g} \tag{4.38a}$$

$$div\left(H^T_{cond}\right) = \int \Pi\left(\overline{Q^+_{cond}} + \overline{\chi_{cond}Q^-}\right)\frac{dp}{-g} \tag{4.38b}$$

$$div\left(H^T_{diff}\right) = \int \Pi\left(\overline{Q^+_{diff}} + \overline{\chi_{diff}Q^-}\right)\frac{dp}{-g} \tag{4.38c}$$

$$div\left(H^T_{radi}\right) = \int \Pi\left(\overline{Q^+_{radi}} + \overline{\chi_{radi}Q^-}\right)\frac{dp}{-g}, \tag{4.38d}$$

where $div\left(\cdot\right) = \left(a\cos\phi\right)^{-1}\partial_\phi\left(\cdot\cos\phi\right)$. These equations can be summed to give

$$div\left(H^T_\theta\right) = \int \Pi\left(\overline{Q_{conv}} + \overline{Q_{cond}} + \overline{Q_{diff}} + \overline{Q_{radi}}\right)\frac{dp}{-g}$$

.

Similarly for water vapor

$$div\left(H^T_q\right) = L_v(\overline{E} - \overline{P}), \tag{4.39}$$

where $\overline{E}$ is the mean evaporation and $\overline{P}$ is the mean precipitation.

The precipitation comes from condensation which also results in latent heating, so that

$$L_v\overline{P} = \int \left(Q_{conv} + Q_{cond}\right)\frac{dp}{-g}. \tag{4.40}$$

Note that the large scale condensation scheme conserves energy at every vertical level (Frierson et al., 2006), while the subgrid scale convection scheme only conserves energy integrated over the entire column (Frierson, 2007).

If we approximate $\theta_e \approx \theta + \frac{L_v}{C_p}q$ (Shaw and Pauluis, 2012), then

$$\begin{aligned} div\left(H^T_{\theta_e}\right) &\approx div\left(H^T_q\right) + div\left(H^T_\theta\right) \\ &= L_v(\overline{E} - \overline{P}) + \textstyle\int \Pi\left(\overline{Q_{conv}} + \overline{Q_{cond}} + \overline{Q_{diff}} + \overline{Q_{radi}}\right)\frac{dp}{-g} \\ &\approx L_v\overline{E} + \textstyle\int \Pi\left(\overline{Q_{diff}} + \overline{Q_{radi}}\right)\frac{dp}{-g}. \end{aligned}$$

The last line of the approximation is consistent with $\theta_e \approx \theta + \frac{L_v}{C_p}q$, i.e. $\dot{\theta_e} \approx \dot{\theta} + \frac{L_v}{C_p}\dot{q}$.

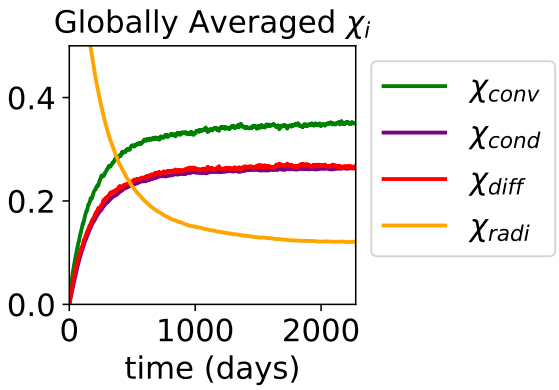

Figure 4.14: Time evolution of the globally averaged tracer tag fractions χ_i during the tag spinup.

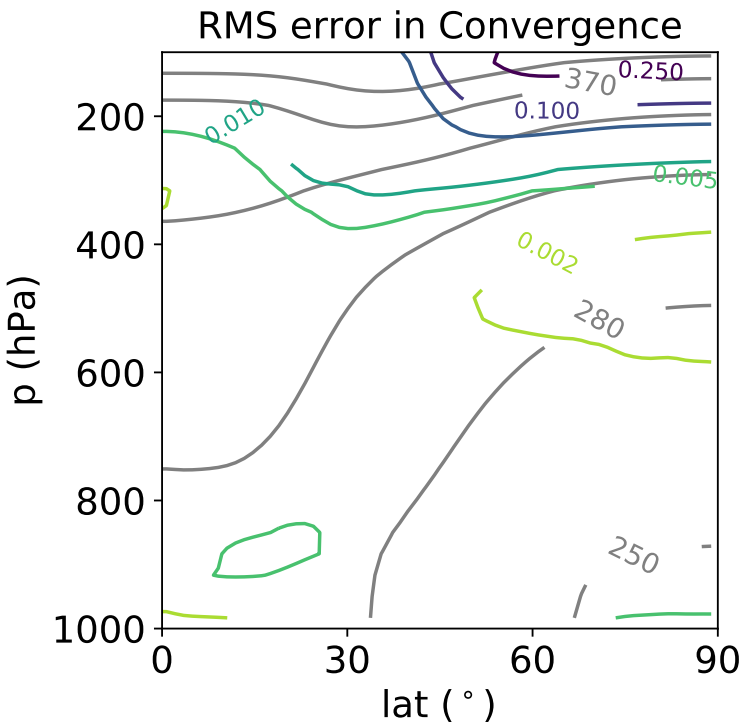

Figure 4.15: The root mean squared residual between θ and the sum of the tagged tracers, given by equation (A1). The grey lines show zonal mean, climatological mean, θ (contour interval 30 K).

We can also calcuate the divergence of H_{moist} by summing over equations (4.38a), (4.38b), and (4.39), and using (4.40), to get

$$\begin{aligned} div\left(H^T_{moist}\right) &= div\left(H^T_{cond}\right) + div\left(H^T_{cond}\right) + div\left(H^T_q\right) \\ &\approx L_v\overline{E} + \int \Pi\left(\overline{\chi_{conv}Q^-} + \overline{\chi_{cond}Q^-}\right)\frac{dp}{g} \end{aligned}$$

and similary we sum over (4.38c) and (4.38d) to get

$$\begin{aligned} div\left(H^T_{dry}\right) &= div\left(H^T_{diff}\right) + div\left(H^T_{radi}\right) \\ &= \int \Pi\left(\overline{Q^+_{diff}} + \overline{Q^+_{radi}}\right) + \Pi\left(\overline{\chi_{diff}Q^-} + \overline{\chi_{radi}Q^-}\right)\frac{dp}{-g}. \end{aligned}$$

As argued in Section 4.5.2, this shows that no terms realted to condensation occur in either $div\left(H^T_{moist}\right)$ or $div\left(H^T_{moist}\right)$.

Chapter 5

Conclusions and Future Research Directions

The single largest net transport of energy from the surface to the atmosphere is the evaporation of water vapor. For this energy to be removed from the atmosphere (which is necessary for the atmosphere to come to steady state), the water vapor has to change phases and release latent energy to the atmosphere. The energy from latent heating fundamentally changes the atmospheric transport of heat and mass, since, unlike sensible heating from turbulent fluxes at the surface, water vapor can travel long horizontal distances before condensing and heating the atmosphere.

The main objective of this thesis was to develop techniques for relating the diabatic heating in the atmosphere, particularly from latent heating, to the atmospheric transport of heat and mass. In Chapter 2 I focused on short time scale surface perturbations and how they were transported along zonal mean θ_e surfaces. In Chapter 3 the response of the circulation averaged on θ_e surfaces to global warming like perturbations was investigated using the STEM. In Chapter 4 a new passive tracer technique was introduced in order to keep track of the sources of θ in the atmosphere. All of these methods highlight the role of latent heating in creating atmospheric transport, either by implicitly including it in the calculation of θ_e, or by explicitly accounting for the fraction of warm air from latent heating in θ.

The fundamental challenge of heat and mass transport in moist atmospheres is that latent heating changes the buoyancy of an air parcel, which can cause the air parcel to become unstable and travel vertically in the atmosphere. One way to account for this is to use θ_e as an analysis variable, implicitly accounting for the eventual latent heating of an air parcel. When θ_e is used as an averaging coordinate, the circulation defined is in balance with the net atmospheric diabatic heating, which makes it an

excellent choice to study the net overturning circulation in the atmosphere responsible for heat transport. Since on average the high θ_e air has to be moving polewards and the low θ_e air has to be moving equatorwards to create a poleward heat flux, using θ as an averaging coordinates separates out these two air streams, even in a turbulent atmosphere. One disadvantage of using θ_e is that it cannot be directly related to the buoyancy without knowing the total water content of an airmass. Implicit in the stability estimates done in Chapter 2 is that there is sufficient mechanical forcing to raise air parcels to the level of lifted condensation so that air can be treated as saturated. The other disadvantage of using θ_e as a variable is that it does not quantify the amount of potential temperature in an air parcel from latent heating.

A second approach considered in this thesis is to use the heat tags introduced in Chapter 4 to track the amount of θ attributable to latent heating. Using the heat tags allows us to retain information about how much of the potential temperature field is attributable to latent heating, even at latitudes remote from regions of latent heating, as air parcels mix and are transported through the atmosphere. If the heat tags are combined with the specific humidity to estimate θ_e the total amount of heat transport associated with the atmospheric hydrological cycle can be found. The main disadvantage of the heat tags is that they require additional calculations and data storage to calculate and store the heat tags.

Studying atmospheric dynamics from climate model output is sometimes limited by the outputs saved from the model. As an example, the LENS experiment used in Chapter 3 only saved six hourly outputs for a small subset of the total years of simulation to reduce the amount of data storage needed (Kay et al., 2015). As models become increasingly complex and move to finer resolution the amount of output from them also increases, the majority of which is not archived for future use. The diagnostics presented in this thesis provide one way to deal with this challenge; by choosing diagnostics which can be saved in the zonal mean at monthly timescales, but which still describe the statistics of transport at much higher frequencies, the data storage requirement to study the transport of the global circulation can be massively reduced. The diagnostics presented in Chapters 3 and 4 are compatible with this purpose, because they utilize standard tools available in most GCMs (keeping running sums and calculating passive tracer advection), making them easy to add to existing GCMs and used in other experiments.

The STEM sensitivity variables could be calculated at monthly intervals and saved with only a small increase in the computation burden. For example, the CESM analysis package already stores zonal mean $\overline{v}$, $\overline{MSE}$, and $\overline{vMSE}$; if $\overline{MSE^2}$ were also stored then circulation on MSE surfaces and its sensitivity kernels could be calculated using the STEM. The requirement to store the zonal mean monthly variables is much smaller than the 6 hourly outputs used to calculate them in this thesis, and (for our purposes) the data storage needed to hold all the outputs could have been reduced substantially if these variables

had been computed first.

Computing heat tags is a greater computational burden, since it involves solving additional passive tracer equations. However, it is small compared to the calculations already done by modern GCMs. As an example, in the new Energy Exascale Earth System Model (E3SM); the default version of the model advects 40 tracers already (Rasch et al., 2019), so adding the four heat tags from Chapter 4 would be a relatively small computational cost. Keeping zonally or temporally averaged heat tags or second order statistics would provide useful information about the effect of remote diabatic processes without necessarily having to save high frequency output.

Besides these technical consideration there are still many open science questions about the general circulation that arise from this work. I briefly outline a few promising research directions here.

In Chapter 2; evidence supporting a linkage between the midlatitude surface and the Arctic mid-troposphere was established. However, the use of a fixed SST model configuration, along with the lack of radiatively active water vapor, prevented us from investigating the impact of the Arctic midtropospheric temperature and moisture anomalies on the Arctic surface. Several studies have highlighted the possible radiative connections between the Arctic mid-troposphere and Arctic surface, driven by intraseasonal variability in the midtroposphere (Woods and Caballero, 2016; Gong et al., 2017). A version of this experiment that used interactive sea surface temperatures or sea ice could help to investigate the linkage between the Arctic midtroposphere and surface. Additionally, Laliberté and Kushner (2014) found that there is a strong seasonal dependence on the midlatitude Arctic midtroposphere connection in reanalysis, and that there is a particular wave 3 pattern in the correlation. Introducing land or other zonal asymmetries with a seasonal cycle into the experiments could potentially help to understand these features by introducing stationary waves into the model and increasing the seasonal contrast.

The results of Chapter 3 show that the climate change response of the moist isentropic circulation is strongly dependent on the variability of θ_e in the atmosphere. Based on the differences in the variability of θ_e between different reanalysis products, more research is needed to understand the present day variability of θ_e. This would have a direct effect on constraining future climate projections of the moist isentropic circulation. Another interesting direction for future research is understanding the physical mechanisms which determine the variability of θ_e in the atmosphere, and especially the relationship between different physical parametrizations and the variability of θ_e. If a simple link between the physical parametrizations and the variability of θ_e could be found, then the variability of θ_e could be constrained to match an observation estimate, which would constrain future responses of the moist isentropic circulation.

The tracer tagging method in Chapter 4 was presented in a general way in order to make it applicable

to a plethora of different scientific problems, such as the study of trace gases which have large sources and sinks in the interior of the atmosphere. Applying the method detailed in Chapter 4 to Carbon Monoxide would yield a system of tracers similar to Fisher et al. (2017), except that it removes the requirement to linearize the source and sink terms. Doing so would enable diagnostics to establish causal linkages between concentrations and specific mechanisms, even when the transport is non-conservative. Studies which focus on conservative transport from a boundary condition can calculate the transit time distribution from the boundary can be determined by taking moments of the Green's function (Holzer and Hall, 2000). This approach is similar for age tracers, which track the transit time from a particular boundary. For heat tags the transport is non-conservative, and so this interpretation cannot be used, without creating a rule to update the age of the heat tags inside of an air parcel. This can be systematically done by directly simulating the moments of the age distribution using the method of Deleersnijder et al. (2001), and would enable us to characterize the transit time distribution for different diabatic sources.

In general, the theme of this thesis and proposed future investigations is to link diabatic processes, which can be sub-grid scale and parameterized, with the transport of heat and mass, which is usually resolved at the grid scale. Understanding these connections has the ability to improve our knowledge of the climate system and make model development easier by linking the diabatic air mass transformation with the dynamical transport. Developing and applying diagnostic which quantify the interactions between physics and dynamics will likely be a fruitful area of future research.

Bibliography

Andrews, D., and M. E. Mcintyre, 1976: Planetary waves in horizontal and vertical shear: The generalized eliassen-palm relation and the mean zonal acceleration. *Journal of the Atmospheric Sciences*, **33 (11)**, 2031–2048.

Audette, A., Fajber R., Kushner P., Wu Y., Peings Y., Magnusdotti G., Eade, R., Sigmond M., and L. Sun, in prep.: Opposite responses of the dry and moist eddy heat transport into the arctic in the pamip experiments.

Betts, A. K., 1974: Further comments on "a comparison of the equivalent potential temperature and the static energy". *Journal of the Atmospheric Sciences*, **31 (6)**, 1713–1715.

Betts, A. K., 1986: A new convective adjustment scheme. part i: Observational and theoretical basis. *Quarterly Journal of the Royal Meteorological Society*, **112 (473)**, 677–691.

Blackport, R., and P. J. Kushner, 2017: Isolating the atmospheric circulation response to arctic sea ice loss in the coupled climate system. *Journal of Climate*, **30 (6)**, 2163–2185.

Bolton, D., 1980: The computation of equivalent potential temperature. *Monthly weather review*, **108 (7)**, 1046–1053.

Bowman, K. P., and T. Erukhimova, 2004: Comparison of global-scale lagrangian transport properties of the ncep reanalysis and ccm3. *Journal of Climate*, **17 (5)**, 1135–1146.

Brayshaw, D. J., B. Hoskins, and M. Blackburn, 2008: The storm-track response to idealized sst perturbations in an aquaplanet gcm. *Journal of the Atmospheric Sciences*, **65 (9)**, 2842–2860.

Bryan, G. H., and J. M. Fritsch, 2004: A reevaluation of ice–liquid water potential temperature. *Monthly weather review*, **132 (10)**, 2421–2431.

Caballero, R., 2005: The dynamic range of poleward energy transport in an atmospheric general circulation model. *Geophysical Research Letters*, **32 (2)**, L02 705.

Chen, G., R. A. Plumb, and J. Lu, 2010: Sensitivities of zonal mean atmospheric circulation to sst warming in an aqua-planet model. *Geophysical Research Letters*, **37 (12)**.

Cohen, N. Y., and W. R. Boos, 2016: Perspectives on moist baroclinic instability: Implications for the growth of monsoon depressions. *Journal of the Atmospheric Sciences*, **73 (4)**, 1767–1788.

Copernicus Climate Change Service Climate Data Store, 2017: Era5: Fifth generation of ecmwf atmospheric reanalyses of the global climate. Available at https://cds.climate.copernicus.eu/cdsapp#!/home.

Dee D., Uppala S.M., Simmons A.J., Berrisford Paul, Poli P., Kobayashi S., Andrae U., Balmaseda M.A., Balsamo G., and P. Bauer, 2011: The era-interim reanalysis: Configuration and performance of the data assimilation system. *Quarterly Journal of the royal meteorological society*, **137 (656)**, 553–597.

Deleersnijder, E., J.-M. Campin, and E. J. Delhez, 2001: The concept of age in marine modelling: I. theory and preliminary model results. *Journal of Marine Systems*, **28 (3-4)**, 229–267.

Döös, K., and J. Nilsson, 2011: Analysis of the meridional energy transport by atmospheric overturning circulations. *Journal of the Atmospheric Sciences*, **68 (8)**, 1806–1820.

Dyer, E. L., D. B. Jones, J. Nusbaumer, H. Li, O. Collins, G. Vettoretti, and D. Noone, 2017: Congo basin precipitation: Assessing seasonality, regional interactions, and sources of moisture. *Journal of Geophysical Research: Atmospheres*, **122 (13)**, 6882–6898.

Emanuel, K. A., 1994: *Atmospheric convection*. Oxford University Press, Oxford, United Kingdom.

Erukhimova, T., and K. P. Bowman, 2006: Role of convection in global-scale transport in the troposphere. *Journal of Geophysical Research: Atmospheres*, **111 (D3)**.

Fajber, R., P. J. Kushner, and F. Laliberté, 2018: Influence of midlatitude surface thermal anomalies on the polar midtroposphere in an idealized moist model. *Journal of the Atmospheric Sciences*, **75 (4)**, 1089–1104.

Fisher, J. A., L. Murray, D. Jones, and N. M. Deutscher, 2017: Improved method for linear carbon monoxide simulation and source attribution in atmospheric chemistry models illustrated using geoschem v9. *Geoscientific Model Development*, **10**, 4129–4144.

Frierson, D., and N. Davis, 2011: The seasonal cycle of midlatitude static stability over land and ocean in global reanalyses. *Geophysical Research Letters*, **38 (13)**.

Frierson, D. M., 2007: The dynamics of idealized convection schemes and their effect on the zonally averaged tropical circulation. *Journal of the Atmospheric Sciences*, **64 (6)**, 1959–1976.

Frierson, D. M., 2008: Midlatitude static stability in simple and comprehensive general circulation models. *Journal of the Atmospheric Sciences*, **65 (3)**, 1049–1062.

Frierson, D. M., I. M. Held, and P. Zurita-Gotor, 2006: A gray-radiation aquaplanet moist gcm. part i: Static stability and eddy scale. *Journal of the Atmospheric Sciences*, **63 (10)**, 2548–2566.

Galewsky, J., A. Sobel, and I. Held, 2005: Diagnosis of subtropical humidity dynamics using tracers of last saturation. *Journal of the Atmospheric Sciences*, **62 (9)**, 3353–3367.

Gelaro R., McCarty, W., Suárez, M.J., Todling, R., Molod, A., Takacs, L., Randles, C.A., Darmenov, A., Bosilovich, M.G., and R. Riechle, 2017: The modern-era retrospective analysis for research and applications, version 2 (merra-2). *Journal of Climate*, **30 (14)**, 5419–5454.

Gong, T., S. Feldstein, and S. Lee, 2017: The role of downward infrared radiation in the recent arctic winter warming trend. *Journal of Climate*, **30 (13)**, 4937–4949.

Gutowski Jr, W. J., and W. Jiang, 1998: Surface-flux regulation of the coupling between cumulus convection and baroclinic waves. *Journal of the Atmospheric Sciences*, **55 (6)**, 940–953.

Hall, T. M., and R. A. Plumb, 1994: Age as a diagnostic of stratospheric transport. *Journal of Geophysical Research: Atmospheres*, **99 (D1)**, 1059–1070.

Hauf, T., and H. Höller, 1987: Entropy and potential temperature. *Journal of the Atmospheric Sciences*, **44 (20)**, 2887–2901.

Held, I. M., and T. Schneider, 1999: The surface branch of the zonally averaged mass transport circulation in the troposphere. *Journal of the Atmospheric Sciences*, **56 (11)**, 1688–1697.

Held, I. M., and B. J. Soden, 2006: Robust responses of the hydrological cycle to global warming. *Journal of Climate*, **19 (21)**, 5686–5699.

Holton, J. R., 2004: *An introduction to dynamic meteorology*. 4th ed., Elsevier, Burlington (MA) United States of America.

Holton, J. R., P. H. Haynes, M. E. McIntyre, A. R. Douglass, R. B. Rood, and L. Pfister, 1995: Stratosphere-troposphere exchange. *Reviews of geophysics*, **33 (4)**, 403–439.

Holzer, M., 1999: Analysis of passive tracer transport as modeled by an atmospheric general circulation model. *Journal of Climate*, **12 (6)**, 1659–1684.

Holzer, M., and G. J. Boer, 2001: Simulated changes in atmospheric transport climate. *Journal of Climate*, **14 (23)**, 4398–4420.

Holzer, M., and T. M. Hall, 2000: Transit-time and tracer-age distributions in geophysical flows. *Journal of the Atmospheric Sciences*, **57 (21)**, 3539–3558.

Holzer, M., and T. M. Hall, 2008: Tropospheric transport climate partitioned by surface origin and transit time. *Journal of Geophysical Research: Atmospheres*, **113 (D8)**.

Iribarne, J. V., and W. L. Godson, 1981: *Atmospheric thermodynamics*. 2nd ed., Springer Science & Business Media.

Jucker, M., and E. Gerber, 2017: Untangling the annual cycle of the tropical tropopause layer with an idealized moist model. *Journal of Climate*, **30 (18)**, 7339–7358.

Juckes, M., 2000: The static stability of the midlatitude troposphere: The relevance of moisture. *Journal of the Atmospheric Sciences*, **57 (18)**, 3050–3057.

Juckes, M., 2001: A generalization of the transformed eulerian-mean meridional circulation. *Quarterly Journal of the Royal Meteorological Society*, **127 (571)**, 147–160.

Kaspi, Y., and T. Schneider, 2013: The role of stationary eddies in shaping midlatitude storm tracks. *Journal of the Atmospheric Sciences*, **70 (8)**, 2596–2613.

Kay, J.E., Deser, C., Phillips, A., Mai, A., Hannay, C., Strand, G., Arblaster, J.M., Bates, SC. Danabasoglu, G., and J. Edwards, 2015: The community earth system model (cesm) large ensemble project: A community resource for studying climate change in the presence of internal climate variability. *Bulletin of the American Meteorological Society*, **96 (8)**, 1333–1349.

Kushner, P. J., and L. M. Polvani, 2004: Stratosphere–troposphere coupling in a relatively simple agcm: The role of eddies. *Journal of Climate*, **17 (3)**, 629–639.

Laliberté, F., and P. Kushner, 2013: Isentropic constraints by midlatitude surface warming on the arctic midtroposphere. *Geophysical Research Letters*, **40 (3)**, 606–611.

Laliberté, F., and P. J. Kushner, 2014: Midlatitude moisture contribution to recent arctic tropospheric summertime variability. *Journal of Climate*, **27 (15)**, 5693–5707.

Laliberté, F., and O. Pauluis, 2010: Winter intensification of the moist branch of the circulation in simulations of 21st century climate. *Geophysical Research Letters*, **37 (20)**.

Laliberté, F., T. Shaw, and O. Pauluis, 2012: Moist recirculation and water vapor transport on dry isentropes. *Journal of the Atmospheric Sciences*, **69 (3)**, 875–890.

Lee, M.-I., M. J. Suarez, I.-S. Kang, I. M. Held, and D. Kim, 2008: A moist benchmark calculation for atmospheric general circulation models. *Journal of Climate*, **21 (19)**, 4934–4954.

Ling, J., and C. Zhang, 2013: Diabatic heating profiles in recent global reanalyses. *Journal of Climate*, **26 (10)**, 3307–3325.

Mantsis, D. F., B. R. Lintner, A. J. Broccoli, M. P. Erb, A. C. Clement, and H.-S. Park, 2014: The response of large-scale circulation to obliquity-induced changes in meridional heating gradients. *Journal of Climate*, **27 (14)**, 5504–5516.

Martínez-Alvarado, O., and R. S. Plant, 2014: Parametrized diabatic processes in numerical simulations of an extratropical cyclone. *Quarterly Journal of the Royal Meteorological Society*, **140 (682)**, 1742–1755.

McCusker, K. E., P. J. Kushner, J. C. Fyfe, M. Sigmond, V. V. Kharin, and C. M. Bitz, 2017: Remarkable separability of circulation response to arctic sea ice loss and greenhouse gas forcing. *Geophysical Research Letters*, **44 (15)**, 7955–7964.

Medeiros, B., D. L. Williamson, and J. G. Olson, 2016: Reference aquaplanet climate in the c ommunity a tmosphere m odel, v ersion 5. *Journal of Advances in Modeling Earth Systems*, **8 (1)**, 406–424.

Michel, C., and G. Rivière, 2014: Sensitivity of the position and variability of the eddy-driven jet to different sst profiles in an aquaplanet general circulation model. *Journal of the Atmospheric Sciences*, **71 (1)**, 349–371.

Neale, R. B., and B. J. Hoskins, 2000: A standard test for agcms including their physical parametrizations: I: The proposal. *Atmospheric Science Letters*, **1 (2)**, 101–107.

Neelin, J. D., and I. M. Held, 1987: Modeling tropical convergence based on the moist static energy budget. *Monthly Weather Review*, **115 (1)**, 3–12.

O'Gorman, P. A., and T. Schneider, 2008: The hydrological cycle over a wide range of climates simulated with an idealized gcm. *Journal of Climate*, **21 (15)**, 3815–3832.

Orbe, C., M. Holzer, L. M. Polvani, and D. Waugh, 2013: Air-mass origin as a diagnostic of tropospheric transport. *Journal of Geophysical Research: Atmospheres*, **118 (3)**, 1459–1470.

Orbe, C., P. A. Newman, D. W. Waugh, M. Holzer, L. D. Oman, F. Li, and L. M. Polvani, 2015a: Air-mass origin in the arctic. part i: Seasonality. *Journal of Climate*, **28 (2015)**.

Orbe, C., P. A. Newman, D. W. Waugh, M. Holzer, L. D. Oman, F. Li, and L. M. Polvani, 2015b: Air-mass origin in the arctic. part ii: Response to increases in greenhouse gases. *Journal of Climate*, **28 (23)**, 9105–9120.

Orbe, C., D. W. Waugh, and P. A. Newman, 2015c: Air-mass origin in the tropical lower stratosphere: The influence of asian boundary layer air. *Geophysical Research Letters*, **42 (10)**, 4240–4248.

Orbe, C., D. W. Waugh, P. A. Newman, and S. Steenrod, 2016: The transit-time distribution from the northern hemisphere midlatitude surface. *Journal of the Atmospheric Sciences*, **73 (10)**, 3785–3802.

Oudar, T., E. Sanchez-Gomez, F. Chauvin, J. Cattiaux, L. Terray, and C. Cassou, 2017: Respective roles of direct ghg radiative forcing and induced arctic sea ice loss on the northern hemisphere atmospheric circulation. *Climate Dynamics*, **49 (11-12)**, 3693–3713.

Pauluis, O., A. Czaja, and R. Korty, 2008: The global atmospheric circulation on moist isentropes. *Science*, **321 (5892)**, 1075–1078.

Pauluis, O., A. Czaja, and R. Korty, 2010: The global atmospheric circulation in moist isentropic coordinates. *Journal of Climate*, **23 (11)**, 3077–3093.

Pauluis, O., T. Shaw, and F. Laliberté, 2011: A statistical generalization of the transformed eulerian-mean circulation for an arbitrary vertical coordinate system. *Journal of the Atmospheric Sciences*, **68 (8)**, 1766–1783.

Peixoto, J. P., and A. H. Oort, 1992: *Physics of climate*. American Institute of Physics, New York, NY (United States).

Perlwitz, J., M. Hoerling, and R. Dole, 2015: Arctic tropospheric warming: Causes and linkages to lower latitudes. *Journal of Climate*, **28 (6)**, 2154–2167.

Pfahl, S., C. Schwierz, M. Croci-Maspoli, C. M. Grams, and H. Wernli, 2015: Importance of latent heat release in ascending air streams for atmospheric blocking. *Nature Geoscience*, **8 (8)**, 610–614.

Pierrehumbert, R. T., 2002: The hydrologic cycle in deep-time climate problems. *Nature*, **419 (6903)**, 191–198.

Pithan, F., and T. Mauritsen, 2014: Arctic amplification dominated by temperature feedbacks in contemporary climate models. *Nature Geoscience*, **7 (3)**, 181–184.

Rasch, P.J., Xie, S., Ma, P-L., Lin, W., Wang, H., Tang, Q., Burrows, S.M., and Caldwell, P., Zhang, K., and Easter, R.C., 2019: An overview of the atmospheric component of the energy exascale earth system model. *Journal of Advances in Modeling Earth Systems*, **11 (8)**, 2377–2411.

Rasch, P. J., and D. L. Williamson, 1990: Computational aspects of moisture transport in global models of the atmosphere. *Quarterly Journal of the Royal Meteorological Society*, **116 (495)**, 1071–1090.

Reynolds, R. W., N. A. Rayner, T. M. Smith, D. C. Stokes, and W. Wang, 2002: An improved in situ and satellite sst analysis for climate. *Journal of Climate*, **15 (13)**, 1609–1625.

Schemm, S., H. Wernli, and L. Papritz, 2013: Warm conveyor belts in idealized moist baroclinic wave simulations. *Journal of the Atmospheric Sciences*, **70 (2)**, 627–652.

Schubert, W. H., S. A. Hausman, M. Garcia, K. V. Ooyama, and H.-C. Kuo, 2001: Potential vorticity in a moist atmosphere. *Journal of the Atmospheric Sciences*, **58 (21)**, 3148–3157.

Scinocca, J., and P. Haynes, 1998: Dynamical forcing of stratospheric planetary waves by tropospheric baroclinic eddies. *Journal of the Atmospheric Sciences*, **55 (14)**, 2361–2392.

Screen, J. A., C. Deser, and I. Simmonds, 2012: Local and remote controls on observed arctic warming. *Geophysical Research Letters*, **39 (10)**.

Screen, J. A., and I. Simmonds, 2010: The central role of diminishing sea ice in recent arctic temperature amplification. *Nature*, **464 (7293)**, 1334–1337.

Shaw, T. A., and O. Pauluis, 2012: Tropical and subtropical meridional latent heat transports by disturbances to the zonal mean and their role in the general circulation. *Journal of the Atmospheric Sciences*, **69 (6)**, 1872–1889.

Shepherd, T. G., and T. A. Shaw, 2004: The angular momentum constraint on climate sensitivity and downward influence in the middle atmosphere. *Journal of the Atmospheric Sciences*, **61 (23)**, 2899–2908.

Singh, H., C. Bitz, J. Nusbaumer, and D. Noone, 2016: A mathematical framework for analysis of water tracers: Part 1: Development of theory and application to the preindustrial mean state. *Journal of Advances in Modeling Earth Systems*, **8 (2)**, 991–1013.

Smith, D.M., Screen, J.A., Deser, C., Cohen, J., Fyfe, J.C., García-Serrano, J., Jung, T., Kattsov, V., Matei, D., R. Msadek, 2019: The polar amplification model intercomparison project (pamip) contribution to cmip6: investigating the causes and consequences of polar amplification. *Geoscientific Model Development*, **12**, 1139–1164.

Sodemann, H., H. Wernli, and C. Schwierz, 2009: Sources of water vapour contributing to the elbe flood in august 2002 – a tagging study in a mesoscale model. *Quaterly Journal of the Royal Meteorlogical Society*, **223**, 205–223.

Soden, B. J., I. M. Held, R. Colman, K. M. Shell, J. T. Kiehl, and C. A. Shields, 2008: Quantifying climate feedbacks using radiative kernels. *Journal of Climate*, **21 (14)**, 3504–3520.

Steinbrecht, W., H. Claude, U. Köhler, and K. Hoinka, 1998: Correlations between tropopause height and total ozone: Implications for long-term changes. *Journal of Geophysical Research: Atmospheres*, **103 (D15)**, 19 183–19 192.

Trenberth, K. E., J. T. Fasullo, and J. Kiehl, 2009: Earth's global energy budget. *Bulletin of the American Meteorological Society*, **90 (3)**, 311–324.

Trenberth, K. E., and D. P. Stepaniak, 2003a: Covariability of components of poleward atmospheric energy transports on seasonal and interannual timescales. *Journal of Climate*, **16 (22)**, 3691–3705.

Trenberth, K. E., and D. P. Stepaniak, 2003b: Seamless poleward atmospheric energy transports and implications for the hadley circulation. *Journal of Climate*, **16 (22)**, 3706–3722.

Vallis, G. K., P. Zurita-Gotor, C. Cairns, and J. Kidston, 2015: Response of the large-scale structure of the atmosphere to global warming. *Quarterly Journal of the Royal Meteorological Society*, **141 (690)**, 1479–1501.

Vallis, G.,K., Colyer, G., Geen, R., Gerber, E., Jucker, M., Maher, P., Paterson, A., Pietschnig, M., Penn, J., and S.I. Thomson, 2018: Isca, v1.0: A framework for the global modelling of the atmospheres of Earth and other planets at varying levels of complexity. *Geoscientific Model Development*, **11 (3)**, 843–859.

Wang, Y., Y. Zhang, J. Hao, and M. Luo, 2011: Seasonal and spatial variability of surface ozone over china: contributions from background and domestic pollution. *Atmospheric Chemistry and Physics*, **11 (7)**, 3511.

Waugh, D., and T. Hall, 2002: Age of stratospheric air: Theory, observations, and models. *Reviews of Geophysics*, **40 (4)**, 1–1.

Wolfe, C. L., 2014: Approximations to the ocean's residual circulation in arbitrary tracer coordinates. *Ocean Modelling*, **75**, 20–35.

Woods, C., and R. Caballero, 2016: The role of moist intrusions in winter arctic warming and sea ice decline. *Journal of Climate*, **29 (12)**, 4473–4485.

Wu, Y., and O. Pauluis, 2013: Examination of Isentropic Circulation Response to a Doubling of Carbon Dioxide Using Statistical Transformed Eulerian Mean*. *Journal of the Atmospheric Sciences*, **70 (6)**, 1649–1667.

Wu, Y., and O. Pauluis, 2014: Midlatitude tropopause and low-level moisture. *Journal of the Atmospheric Sciences*, **71 (3)**, 1187–1200.

Yamada, R., and O. Pauluis, 2016: Momentum balance and eliassen–palm flux on moist isentropic surfaces. *Journal of the Atmospheric Sciences*, **73 (3)**, 1293–1314.

Yang, H., Waugh, D.W., Orbe, C., Zeng, G., Morgenstern, O., Kinnison, D.E., Lamarque, J-F., Tilmes, S., Plummer, D.A., and P. Jöckel, , 2019: Large-scale transport into the arctic: the roles of the midlatitude jet and the hadley cell. *Atmospheric Chemistry and Physics*, **19**, 5511–5528.

Zhang, K., W. J. Randel, and R. Fu, 2017: Relationships between outgoing longwave radiation and diabatic heating in reanalyses. *Climate Dynamics*, **49 (7-8)**, 2911–2929.